UNIVERSITÉ DE VERSAILLES ST-QUENTIN-EN-YVELINES

université PARIS-SACLAY

Improvement of the upper body of HYDROïD robot for bi-manual tasks and manipulation

Thèse de doctorat de l'Université Paris-Saclay
préparée à l'Université de Versailles

École doctorale n°580, Sciences et technologies de l'information et de la communication (STIC)
Spécialité de doctorat : Robotique

Thèse présentée et soutenue à Vélizy - Villacoublay, le 05 Décembre 2017, par

Ahmad TAYBA

Composition du Jury :

M. Vincent HUGEL Professeur des Universités, Université de Toulon	Président, Rapporteur
M. Adrian OLARU Professeur des Universités, Université Polytechnique du Bucarest	Rapporteur
M. Didier PRADON Ingénieur Hospitalier, HDR, Université de Versailles	Examinateur
M. Nathanaël JARRASSE Chargé de Recherche CNRS, Université Pierre et Marie Curie	Examinateur
M. Fethi BEN OUEZDOU Professeur des Universités, Université de Versailles	Directeur de thèse
M. Samer ALFAYAD Maître de conférences, HDR, Université de Versailles	Co-Directeur de thèse

université PARIS-SACLAY
ÉCOLE DOCTORALE
Sciences et technologies de l'information et de la communication (STIC)

Titre : Amélioration de la partie supérieure du robot HYDROïD pour des tâches bimanuelles et la manipulation

Mots clés : HYDROïD, Torse, Epaule-Complexe, Espace de Travail, Actionnement Hydraulique, Modélisation cinématique.

Résumé : Ma thèse vise à contribuer au développement et l'amélioration de la cinématique de la partie supérieure du robot HYDROïD pour des tâches bimanuelles, tout en basant sur une étude biomécanique de cette partie chez l'être humain.
Pour atteindre notre objectif majeur, ce travail adopte dans un premier temps une nouvelle structure hybride de 4 degrés de liberté (ddl) pour le torse du robot distribués en 3 ddl au niveau lombaire et un ddl au niveau thoracique. Cette structure était identifiée après une analyse de l'espace de travail d'un modèle multi-corps simulant la colonne vertébrale d'un être humain, et une étude d'optimisation de ce moldèle permettant la synthèse de la structure envisagée.
Dans un second temps, une amélioration de la cinématique du bras du robot a été mise en place, en introduisant la notion de l'épaule complexe à la présente structure. Le choix de ce nouveau degré de liberté était le fruit d'une approche systématique pour augmenter l'anthropomorphisme géométrie du bras souhaité vers un bras humain de la même taille. Les 2 structures proposées ont passé par la suite par la phase de conception mécanique tout en respectant les contraintes géométriques et en se basant sur l'énergie hydraulique comme étant l'énergie d'actionnement de ces systèmes. Enfin, le modèle IGM pour la solution générique du torse a été établi et son adaptation à notre cas particulier a été identifiée. Une solution optimisée pour ce mécanisme basée sur 2 différents critères a été donnée.

Title : Improvement of the upper body of HYDROïD robot for bi-manual tasks and manipulation

Keywords : HYDROïD, Torso, Shoulder Complex, Workspace, Hydraulic actuation, Kinematic modelling.

Abstract: My thesis aims at contributing to the development and the improvement of the kinematics of the upper body of the HYDROïD robot for bi-manual tasks, while basing on a bio-mechanical study of this part at the human being. To reach our major goal, this work adopts at first a novel hybrid structure of 4 degrees of freedom (DOF) for the trunk of the robot distributed in three DOF at the level lumbar vertebra and one DOF at the thoracic level. This structure was identified after analysis of the work-space of a multi-body model feigning the vertebral column of a human being, and an optimization study of this model allowing the synthesis of the envisaged structure.
Secondly, an improvement of the kinematics of the arm of the robot was organized, by introducing the notion of the shoulder complex in the present structure. The choice of this new degree of freedom was the fruit of a systematic approach to increase the anthropomorphism geometry of the wished arm towards a human arm of the same size. The two proposed structures crossed afterward by the mechanical design phase while respecting the geometrical constraints and by using the hydro-electric power as being the energy of actuation of these systems. Finally, the model IGM for the generic solution of the trunk was established and its adaptation to our particular case was identified. A solution optimized for this mechanism based on 2 various criteria was given.

Université Paris-Saclay
Espace Technologique / Immeuble Discovery
Route de l'Orme aux Merisiers RD 128 / 91190 Saint-Aubin, France

Contents

List of Figures

List of Tables

Acknowledgments

Certainly, a few words are never enough to thank the leaders of this work as well as the transparent soldiers who endured the suffering so that I will be the laureate of that moment. Whoever gives you a favour is entitled to thanks, and whoever gives you good is entitled to praise, and whoever continues to give is worthy of gratitude.

In the first place, I would like to thank Prof. Fethi Ben Ouezdou, director of the thesis, for the trust he has placed in me in accepting this doctoral work. In particular, I would like to express my sincere appreciation to Prof. Alfayad Samer, co-director of this Thesis, for his many advice and for all the hours he has devoted to directing this research. I would also like to tell him how much I appreciated his availability during these years, and his constant concern for the success of this work. Finally, I was extremely sensitive to their human qualities of listening and understanding throughout this PhD work.

My thanks also go to all the members of the jury to know Mr. Vincent Hugel, Mr. Adrian Olaru, Mr. Didier Pradon and Mr. Nathanael Jarasse for having me does the honor of participating in the thesis defense and judging my work.

I would like to thank my dearest family, mom and dad, my two brothers Rabih and Rami, for the support and encouragement that they provided me over the years. Thank you for giving me strength to reach my goals and chase my dreams.

I would express my great gratitude to my beloved wife Fatima, who's standing with me from the beginning. Thank you for your patience and your serious commitment to fulfill this position. You still the greatest gift anyone has ever given to me.

I would like to thank sincerely the director of LISV Prof. Luc Chassagne and all the

administrative staff.

Finally, I would like to thank my best colleagues and my second family, Khaled, Ahmed, Moustafa, Tahoun, Anas, Asswad and Kardofaki. Thank you for your encouragement, we have been the most wonderful team and we make together a wonderful experience.

For my wonderful wife,
and my future sons.

Introduction

Brothers Čapek, the creators of the word "**ROBOT**" do not know that this fiction will one day become a reality. Surrounded by many challenges, several decades have been invested in the development of an extraordinary human like machine dedicated to serving a human being. And, what a challenge to face when aspiring as much and as widely as possible one of the most complex biological systems we know: "**Human Being**".

In this context, many projects have been launched to develop a new humanoid aimed to interact with human environment, and provide services such as handicapped carrying, housework assistance, and moreover it exceeds that, to execute a complex tasks such as ultimate helpers in man-made or natural disasters. For that purpose, it was a trend to find a structure of the upper part of the robot(Trunk and arms) capable of generating a large workspace as well as a high degree of redundancy for its end effector, presenting afterward a rather important and equivalent problem for the locomotion of bipeds topic.

Hence, different constraints have been faced during the design process. The most important, was to produce an anthropomorphic design able to imitate the kinematic of human limbs; So, the researchers begin to study in depth the anatomy of human being, believing that this latter is the best in terms of performance and capabilities. The main role behind this planned kinematics is to increase the degree of flexibility, which may lead to an increase in the degree of redundancy for the envisaged system. In the other hand, they went to get a friendly design character in order to be acceptable from the geometric functional and psychological points of view, especially for human robot interaction purposes [10],[11].

Indeed, the geometrical, kinematic and dynamic behavior of the end-effector (hands) is affected solely and directly by the structure of the trunk and the arms. For this reason,

the search for an optimal structure for the trunk of HYDROïD robot as well as the investment to improve the structure of its arms while respecting all the constraints already presented are the core of this thesis.

Who is HYDROïD? HYDROïD (Hydraulic + Android) is a underdevelopment humanoid robot project initiated by Alfayad et al in 2005 at University of Versailles to develop a robot with more than 40 degrees of freedom totally actuated by the hydraulic energy except its head [12][13][14][15][16]. This robot should have $1.85m$ of height and $120Kg$ of weight and it should be designed to walk with a nominal speed of $1.2m/s$. The biomechanical study that preceded this project leaded to develop an anthropomorphic structure for the legs and the arms able to cohabit with human environment. In addition and as it is actuated using hydraulic energy, this new generation of humanoid robot is characterized by a high power to mass ratio. These characteristics make this structure not only to be a research platform for humanitarian behaviors, but also to be the first intervene for a human or natural made disasters, completing by this a dexterity of easy and hard manipulation and locomotion tasks. these characteristics do not exist in a lot of humanoid robot.

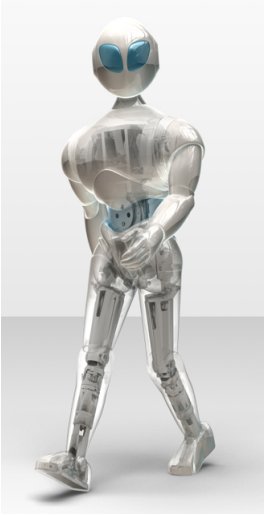

Figure 1: HYDROïD (futur version)

Our objectives in this thesis is to complete the development of this robot by using a novel concept of thinking about the trunk of the existing humanoid robot. This concept should verify a high degree of flexibility inspired from the anatomy of human spine and by introducing a new degree of freedom at the thoracic level of the robot. Furthermore, the robot's trunk or torso joints are generally exposed to a high level of torque being given the weight of the upper part (arms, head) and its influence such as lifting heavy objects. For this purpose, a mechanical system capable of generating this range of torque at each joint must be set up while satisfying the constraint of the total mass of the system. This work is completed by an improvement in the kinematics chain of the existing arm by analyzing the anatomy of the shoulder-complex to acquire an increasing in the workspace of the end effector. This analysis leads to the development of a new

degree of freedom at the shoulder girdle leading to an increase in the manipulability of the robot arm. After analyzing, the mechanisms of the torso joints and the shoulder girdle are presented as well as their mechanical design and the technological choices for both systems. The last part of this thesis present an optimized solution for the hybrid mechanism of the torso based on the inverse geometrical model calculation. Finally, a general conclusion and the perspectives of this work are presented.

Chapter 1

Humanoïd Trunk - State of the art

Contents

In this chapter, we will present a macroscopic anatomy for the human spine as well as a state of art on the existed humanoid robot with their trunk design.

1.1 Trunk of human body

In human anatomy, the trunk is the middle part of the body. It is divided into three parts: the thorax, the abdomen and the small pelvis, and supported by the two lower limbs that are connected to the pelvis below. It also carries the two upper limbs at the thorax, on each side, and connected at the top to the head via the neck. The trunk has a complex structure with an articulated skeleton and a dense muscular network which gives it sufficient versatility to accomplish a large number of different spots while maintaining the body in balance. It is armed to fulfill the role of central part of the body[17]. In addition, trunk of human body, where the center of mass (COM) is located, plays a key role to maintain a stable posture and providing an efficient gait cycle.
Indeed, the trunk of a human being has essential mechanisms that work in coherence with the required muscles and the nervous system to participate in one way or another to the human manipulation tasks as well as to its dynamic locomotion.
The following section will present a macroscopic anatomy of the main parts of the trunk.

1.1.1 Human Spine

In human body, the most complex and remarkable system is their spine. It is located in the torso part and transmits the weight of the upper body (Arms & Head) to the pelvis; and given his flexibility, it offers a wide range of movements to the whole body and contribute to bear external loads to achieve several kinds of motion.

The human body spine is composed of 33 vertebrae localized at the bottom of the upper body and it distributed into five parts: (i)- Cervical Spine, contains seven vertebrae $(C1\ to\ C7)$ characterized by small, light and most mobile vertebrae in the vertebral column. (ii)- Thoracic spine, the biggest part that contains 12 vertebrae $(T1\ to\ T12)$ starting from the bottom of the cervical vertebrae to top of the lumbar. The thoracic vertebrae increase in size going towards the lumbar vertebrae. (iii)- Lumbar spine, consisting of five vertebrae $(L1\ to\ L5)$ characterized by being the largest vertebrae given that they are the most responsible for bearing the weight of the body. (iv & v)- Sacrum and Coccyx consisting of five and four fused vertebrae respectively.

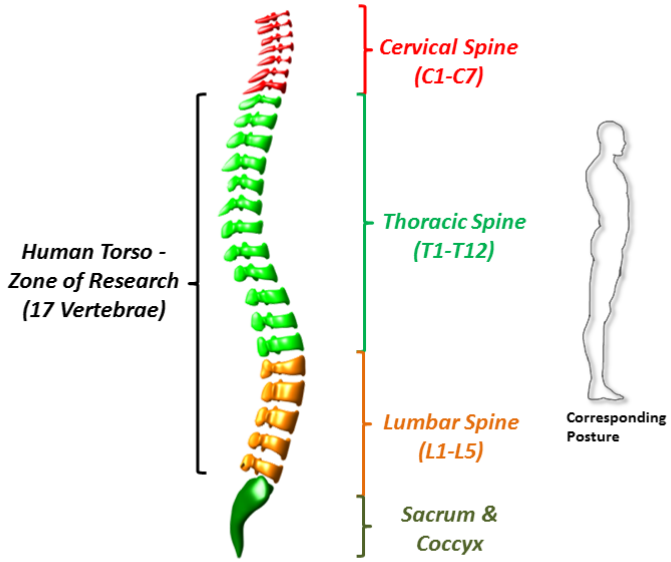

Figure 1.1: Spine of Human body

As shown in the figure 1.1, the vertebral column display different curves, a natural slight lordotic curve exists in the cervical spine, a slight kyphotic curve exist in the thoracic spine, as well as a natural light lordotic curve in the lumbar spine. These curvatures allow a straight biped posture, looking forward, with a low energy cost by providing a more even distribution of body weight.
The main parts of the human spine are listed below:

Vertebrae

The vertebrae (fig1.2a) are irregularly shaped bones that stack on top of each other to form the vertebral column. The shape and structure of vertebrae is not consistent along the vertebral column, but a general common architecture exists between all vertebrae. The elements that form this architecture are: the body or the centrum, the vertebral arch and the vertebral foramina.

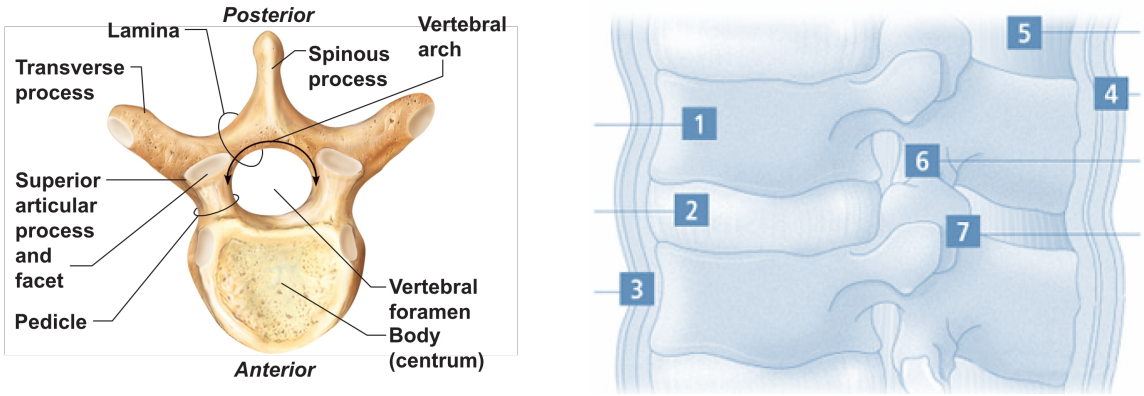

(a) Vertebrae[18] (b) Section of human spine

Figure 1.2: Essentail Parts of human spine

Intervertebral disc

The upper and lower surfaces of each vertebra (fig 2.4b- 1) are separated by intervertebral discs (fig 2.4b-2) composed of cartilage, the function of which is to absorb or dampen the shocks and pressures associated with movements or forces. The thickness of the disc varies according to the region of the back; It takes a maximal value between the lumbar vertebrae.

Ligaments

The vertebrae are connected to each other by two fibrous bands, the ligaments (anterior, posterior and intervertebral), which extend over the whole height of the vertebral column. One of these ligaments is located forward while the other is behind the vertebral bodies.

Spinal Cord

This is one of the main elements of the central nervous system and consists of a white cord with 1 centimeter in diameter and 50 centimeters in length. The spinal cord passes through the vertebrae giving it an essential safety field (fig 2.4b- 5).

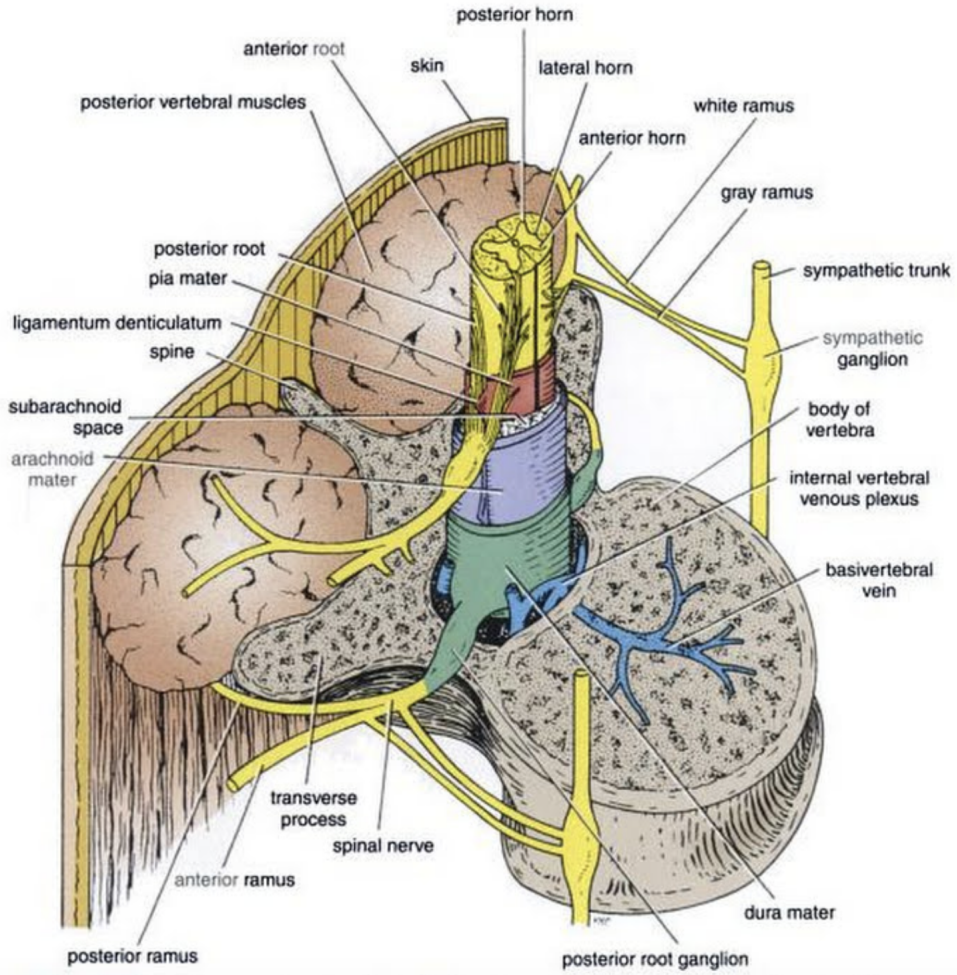

Figure 1.3: Oblique section through the first lumbar spine showing the spinal cord and its covering membranes [1]

The articular processes

The two lower (fig 2.4b- 6) and upper (fig 2.4b- 7) processes of each vertebra are articulated with the two neighboring vertebrae. More details about the constitution of the vertebral column is given by the figure 1.3 extracted from [1]

Human Spinal column plays a remarkable role not just to protect spinal cord and support the majority of body weight, but also it contributes to the manipulability efficiency of the human upper limbs. In humanoid robotics, this part is largely forgotten or in other words it is used as a storage space without taking into account its important

effects. In the next part, we will present a bibliography on a part of humanoid robots by classifying them according to the degree of freedom used for their trunk. This part is preceded by a definition of a two essentials terms : Anthropomorphism Morphology and Anatomical planes of the body.

1.1.2 Anthropomorphism Morphology

One of our objectives is to create a robot shape which has the same outer form of human being. Thus, we have searched for a technique to estimate the human body segment parameters (BSP) including segment dimensions, and segment initial parameters such as mass, center of mass location, and moment of inertia. Many models were developed to achieve this target [19]. From these, modified Hanavan model which is a multi-segment model consisting of 16 rigid segments as shown in figure 1. It was originally developed by E. P. Hanavan in 1964 [20], then updated by Clauser et al. in 1969 [21] , and finally updated by Miller & Morrison in 1975 [2]. Although Hanavan is not the most up to date model to estimate the segment mass, it respects the human morphology. Since HYDROïD follows the Hanavan Model [14], certainly all its missing mechanisms must obey the same body dimension ratio.

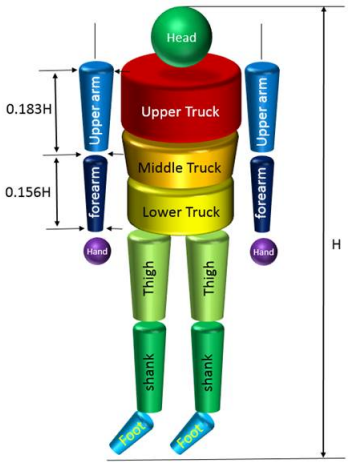

Figure 1.4: Hanavan model [2]

1.1.3 Anatomical planes of the body

There are three primary planes used to characterize the motion of the human body (fig 1.5). These planes can be categorized as the transverse or horizontal plane, frontal or coronal plane and sagittal or median plane. The transverse plane divides the body into upper and lower or superior and inferior parts, while, the sagittal plane divides it into left and right portions, and finally the coronal or frontal plane divides the body into front and rear portions, where anterior is towards the front or face and posterior is toward the

rear or back. The body limb can undergo Flexion/extension motion in the sagittal plane, lateral flexion in the frontal plane and axial rotation in the transverse plane.

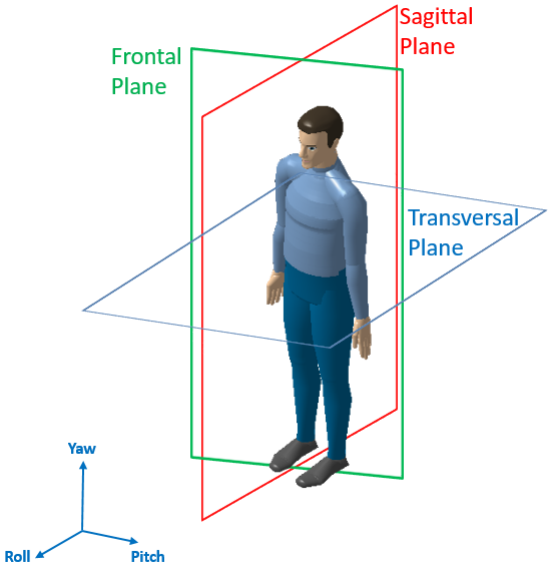

Figure 1.5: Anatomical planes of the body

1.2 Biped robots

Notably the development of humanoid robots is a highly interesting yet challenging task. It requires the effort and collaboration of a high number of researchers from various domains, in order to design a humanoid robot able to integrate in human's everyday life. However, despite the increased sophistication in nowadays humanoids structure, the spine remains a part of the robots body were major improvement is required. In this part, we will review the current state of the art of the existing humanoids vertebral columns focusing on the advantages and disadvantages of each structure.

1.2.1 Humanoid with rigid trunk

ASIMO [22] is the 11th in a line of walking robots developed by Honda, called the P-Series[23][24]. The name of the robot stands for 'Advanced Step in Innovative Mobility'. The goal behind the creation of this robot was the creation of a human helper.

Therefore, its height is four feet (120 centimeters) perfectly suited for the help of a person in a wheelchair or confined to bed. Honda's development of humanoid robots began in 1986, where the company started with the E0 model a two legged robot made to walk by putting one leg before the other however the walking cycle took plenty of time. Honda continued the humanoid robots project and introduced between the years 1987 and 1991 the models E1-E2-E3. Fast walking was achieved after studies on both human and animal walking. The next step for Honda was to complete the walking cycle by stabilizing walking even on slopes and uneven surfaces. This was achieved between the years 1991 and 1993 with the introduction of E4-E5-E6. Researches on completely humanoid robots developed between 1993 and 1997 where P1-P2-P3 where introduced. And in the year 2000, ASIMO was introduced before having major updates in 2005. the remarkable thing in Honda's robot was the design of the torso robot. It is design to be a storage area for electronic components and batteries without any additional degree of freedom. Figure 3.12 present some version of Honda's robot.

1.2.2 Humanoid with one DOF trunk

The humanoid robot of KAIST university KHR-2 was developed to have 41 DOF in total and one yaw DOF at the trunk[25]. It has 120 cm of height and 56 Kg of weight. All its DOF are actuated using DC motors because of their easy controllability and compactness. It is equipped with four 3-axis force/torque sensor, one inertia sensor and two CCD cameras. It can perform powerful kicks and kung-fu, and responds immediately to commands.

The new version of KHR-2, named HUBO or KHR-3, is a head mounted on a life-size walking bipedal frame[26]. it was released in 2005 with a voice recognition as well as sophisticated vision in which, two eyes moves independently of one another. This version was followed by Albert HUBO (2005), HUBO 2 (2008), HUBO 2 Plus (2011. HUBO was the winner of DARPA Robotics Challenge on June 2015. All these robots were recognized with one yaw DOF at its trunk level.

JOHNNIE robot is a biped robot developed at TUM university with 17 actively driven joints[27]. It has 49 Kg of weight and 1.8 m of height. its upper body is equipped

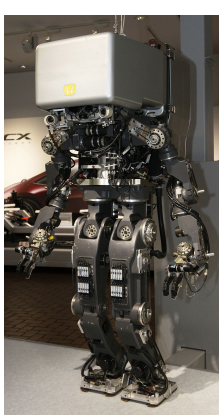

(a) P1

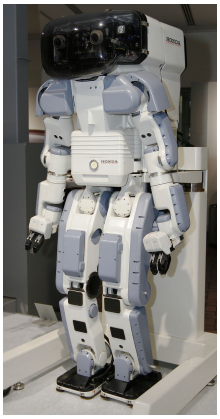

(b) P2

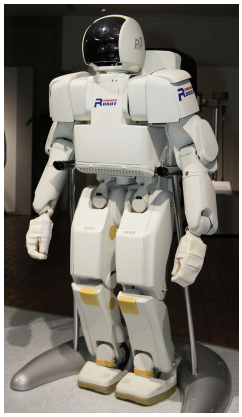

(c) P3

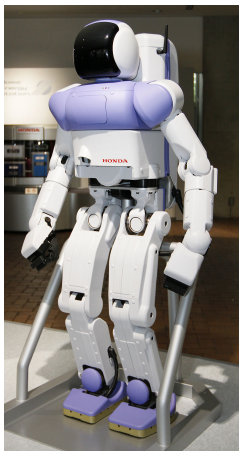

(d) P4

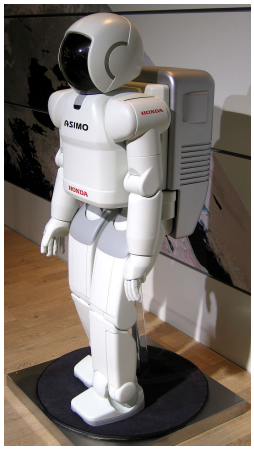

(e) ASIMO

Figure 1.6: HONDA's Humanoid robots

with a rotational joint about the vertical axis. JOHNNIE can be walk with a maximum speed up to 2.2 Km/h and it use a vision system to detect, step on and avoid obstacles.

The Torque-Controlled Humanoid Robot TORO developed at DLR biped. The idea behind this robot is to serve as an experimental platform for evaluating torque based control approaches[28]. It is a human-size humanoid robot with a total height of 174 cm and a weight of 76.4 kg. It has 25 torque-controlled and 2 position-controlled revolute joints without the hands. It recognized with one yaw joint for its waist.

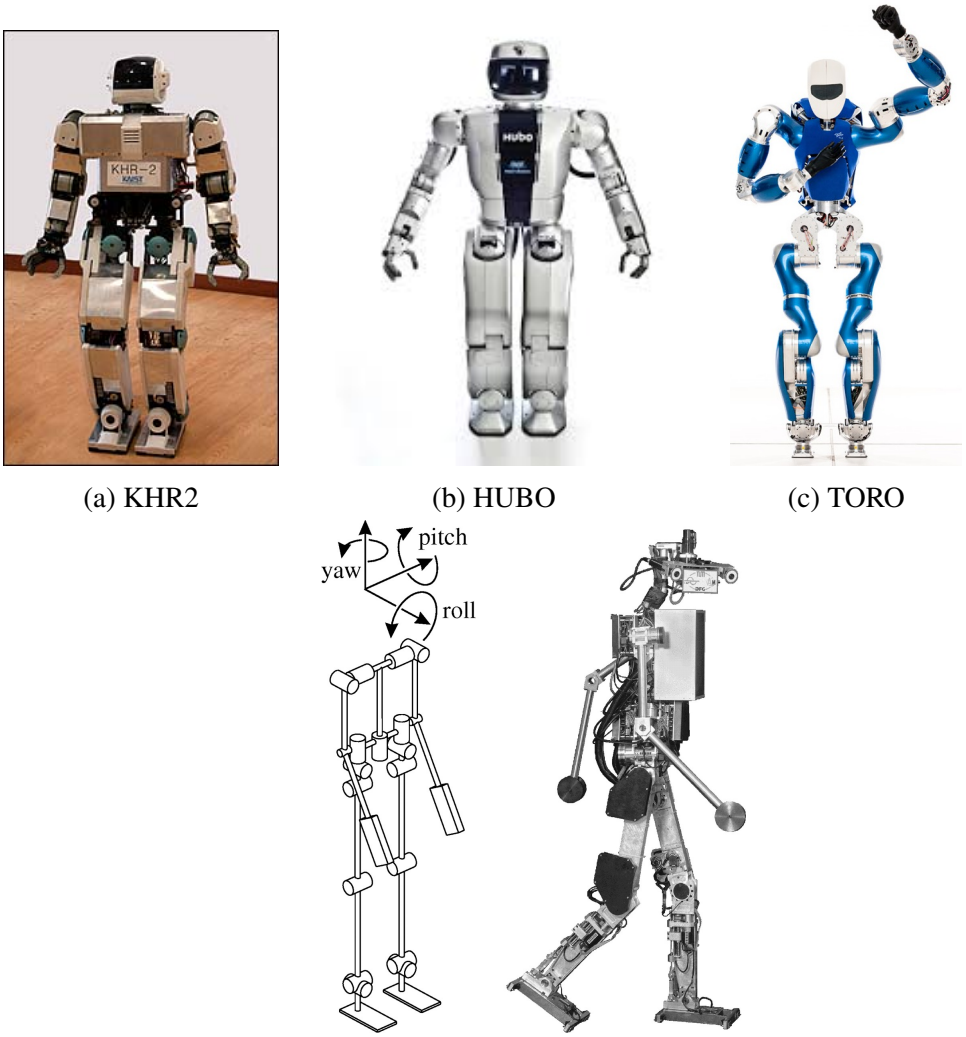

(a) KHR2 (b) HUBO (c) TORO

(d) Johnnie

Figure 1.7: Biped robot with one DOF trunk

1.2.3 Humanoid with two DOF trunk

The cybernetic humanoid developed by AIST called HRP4 has a quasi-rigid upper body with just two DOF at the waist [29]. This robots is a human friendly humanoid, and its main features are the lightweight and slim body, the improved object manipulation and expandability, as well as the reduce price and actuation power compared with the previous version HRP series. HRP4 has two degrees of freedom in the waist area but its spine still remains a remarkable storage area. HRP versions are presented in figure

1.8(a,b,c,d and e).

LOLA robot[30], successor of the German robot Johnnie, is recognized by another revolute joint arround the roll axis at the trunk. This articulation could make it possible to walk by unfolding the knee at certain moments of the cycle, as does the human being. However, this robot has not yet demonstrated any operational capabilities(figure1.8f).

REEM-C is a full-size biped humanoid robotics research platform[31]. ItâĂŹs flexible, reliable, open, standard and upgradable. An advanced robot to boost research areas like navigation, HRI, vision or AI. It has 68 degrees of freedom with pitch and roll joint at trunk level(figure1.8g).

Another humanoid has two DOF freedom at the waist is the Sarcos robot (figure1.8h). It's a humanoid robot, developped by the robotics company Sarcos, for doing the world's most dangerous jobs. It's designed to use a hydraulic power for its actuators. Despite the fact that this robot is characterized by a great force, it lacks a flexibility at the level of its torso as well as at it arms [32].

1.2.4 Humanoid with three DOF trunk

The three degrees of freedom structure of a humanoid robot spine is a relatively simple one that can, to a certain extent, provide the main motion of the torso in the planes of motion. This vertebral column architecture was used in the robots ATLAS and Romeo.

Atlas(figure 1.9a) is a full-scale, hydraulically-actuated humanoid robot manufactured by Boston Dynamics, with the US Defense Advanced Research Projects Agency for its robotics challenge. Atlas is designed to negotiate rough, outdoor terrain in a bipedal manner, while being able to climb using hands and feet as a human would. The robot stands approximately 188cm tall with a total mass of 155kg without its hands attached. It has two arms and two legs with six degrees of freedom each, a torso with three degrees of freedom and a head with one degree of freedom generated by the neck joint; which makes a total of twenty-eight actuated degrees of freedom for the ATLAS humanoid[33][34]. However Boston Dynamics released a new version of ATLAS that is much lighter and shorter than the previous model. The video released by Boston Dy-

(a) HRP1

(b) HRP2

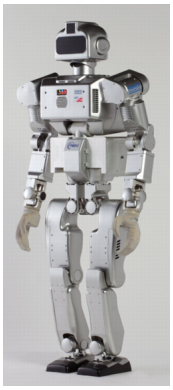

(c) HRP3

(d) HRP4C

(e) HRP4

(f) LOLA

(g) REEM-C

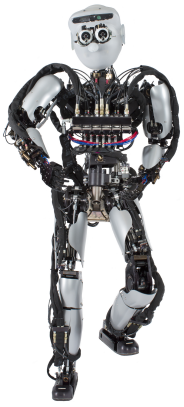

(h) Sarcos

Figure 1.8: HRP series and Sarcos robot

namics showed the ability of ATLAS to walk in a dynamically balanced way, lift 10lb boxes, pick itself autonomously after a fall and resist to external perturbation.

ROMEO (figure 1.9b) is a humanoid robot having the size of an 8 years old kid, with a height of 140cm and a weight slightly above 40Kg. Designed to explore and further research into assisting elderly people and those who are losing their anatomy. ROMEO is the fruit of collaboration between numerous French laboratories and institutions. To be as light as possible, its body is made of carbon fiber and rubber, and was designed to avoid the risk of injury to the person that will attend[35][36]. Romeo has a total of 37 degrees of freedom, two for the head, two for each eye, two for the neck, two for each shoulder and elbow, three for each wrist, one for each hand, three for the vertebral column, one for each knee and foot and two for each ankle As for the torso of Romeo, the neck is mounted to it, the arms the column and the batteries are all fixed to it, which makes it a huge rigid piece difficult to assemble. The solution for this problem came by using a lattice structure. The general principle behind the vertebral column of this robot is the use of three vertebrae to insure the pitch and roll degrees of freedom along with a yaw joint localized on the upper vertebrae. This system is actuated by electrical motors.

(a) (b)

Figure 1.9: (a): ATLAS, (b): ROMEO

1.2.5 Humanoid with four DOF trunk

A four degree of freedom spine architecture was used in different robots notably the wheeled robots JUSTIN and Twendy one, ROBIAN and the biped robot WABIAN-2.

JUSTIN(figure 1.10a) is a wheeled robot developed by the German Aerospace Center (DLR) at the Institute of Robotics and Mechatronic. JUSTIN has a torso with three actuated joints and a kinematically coupled fourth joint. The goal behind the upper body design of this robot is to increase its workspace[37].

TWENDY-ONE (figure 1.10b) is a sophisticated human-symbiotic-robot which equips the functions of human friendly communication, human safety assistance and dexterous manipulation. The special feature of TWENDY-ONE is the combination function of the dexterity with passivity and the high-power output [38]. The trunk of TWENDY-ONE has four degrees of freedom in total for the torso. The high-power actuators are installed into the joints to pick up a heavy object on the floor and to support the human body[39].

Karlsruhe Institute of Technology presented a robot prototype capable of assisting a human being in the kitchen. It has been named ARMAR and comes in a humanoid form (figure 1.10d). It consists of an autonomous mobile wheel-driven platform, a body with 4 DOF, two anthropomorphic redundant arms each having 7 DOFs, two simple gripper and a head with 3 DOF. The total weight of the upper-body of ARMAR was about 45kg. Since 2006, many advanced version of ARMAR have been see light. It was equipped with position, velocity and force-torque sensors to maintain the contrability[40][41][42].

ROBIAN developped at LISV - UVSQ, is a humanoid designed to efficiently contribute to the development of a real test bed of active/passive prosthesis for the disabled. It has 16 DOFs, a weight of 25kg and a height of 1.1m. To achieve a human like gait cycle, based on the dynamic approach for walking gaits, the human like aspect of the upper part of the robot was ignored. Following an analysis based on modeling the human body using Hanavan model and simulating the model during a positioning stage, a launching stage and two established walking cycles, a minimal mechanism is deduced to replace the upper part. Using the Dynamic Equivalence principle, a four DOFs RPPP

model was chosen to replace the upper part of the realistic simulated model in a way to make equivalence in terms of effort between the two models [43][44].

Another humanoid having a four degree of freedom upper body is WABIAN-2(figure 1.10e). Developed in Japan, WABIAN-2 has been designed with 1.5 m in height, and 64kg in weight. In order to mimic human movements, the robot has 41 DOFs and the movable range of the joints designed in reference to human's one. WABIAN-2 has two 7-DOF legs, a 2-DOF waist, a 2-DOF trunk, two 7-DOF arms, a 3-DOF neck, and two 3-DOF hands. The waist system of WABIAN is developped to minimize the displacement of the trunk and simplify the kinematics calculation[45].

1.2.6 Humanoid with flexible spine

The department of Mechano-Informatics at the University of Tokyo in Japan developed fully tendon-driven musculoskeletal humanoids. The idea behind these humanoids is to replicate the human motion as much as possible. Therefore, the vertebral column of these humanoids is a relatively sophisticated architecture.

In 2000, the first prototype Kenta was introduced (figure 1.11a). The spine of this robot is formed by eleven articulated spherical joints, then a thirty three degrees of freedom. The joints forming the spine are not simple ball and socket joints; they were equipped with a lock mechanism that prevents the vertebra excessive movement. Intervertebral discs where made of elastic silicone rubber, and the ligaments where made of tension springs[46].

In 2005, Kotaro (figure 1.11b) was developed following Kenta. The spine was reduced to five articulated spherical joints and it was compensated by an improved shoulder structure consisting of a collarbone and scapula. Compared to Kenta, Kotaro was improved in the joint DOFs arrangement and structures of its whole body [47].

In the year 2008, Kojiro (figure 1.11c) was developed having a high-power actuating system to solve the lack of joint power faced in Kenta and Kotaro. This robot has a height of 105cm and a weight of 25kg. During the design of this robot, the few movable range of the human thoracic vertebra was taken into consideration. In total Kojiro has twelve degrees of freedom in its vertebral column [48].

(a) JUSTIN

(b) TwendyOne

(c) ARMAR2

(d) ARMAR3

(e) WABIAN-2

Figure 1.10: Robots with Four DOF trunk

In order to imitate the body movement with great accuracy, the robot Kenshiro (figure 1.11d) was then developed in 2013 following Kojiro. The height of Kenshiro is about 158cm and it weight approximately 50 kg. Kenshiro has 64 DOFs, its spine is designed in a manner that takes into consideration the fact that the lumbar spine rarely contributes to the rotation in the transverse plane [49].

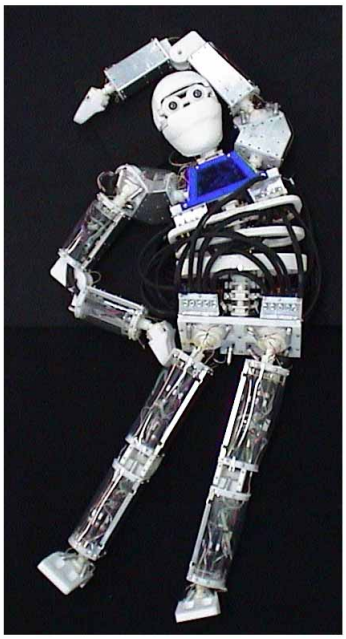

(a) Kenta - 2000

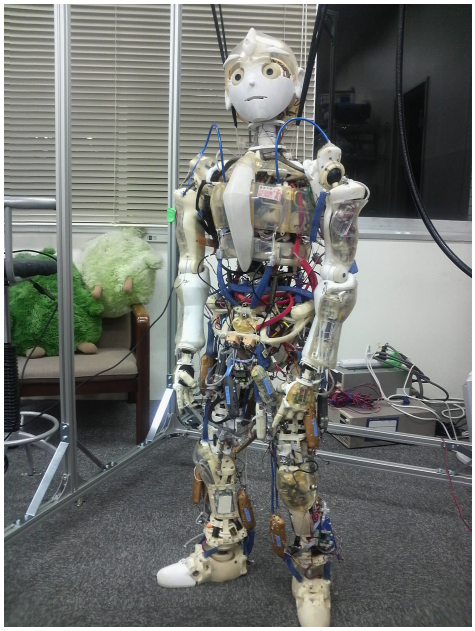

(b) Kotaro - 2005

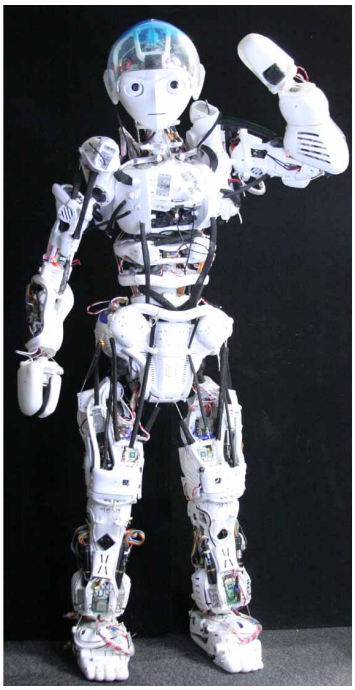

(c) Kojiro - 2008

(d) Kenshiro - 2013

Figure 1.11: Robots with flexible Spine

1.2.7 Kid size Humanoid

Kid sized humanoids with sophisticated spinal structures were developed notably POPPY, ACROBAN and the underdevelopment HOPALALA.

POPPY (figure 1.12a) is designed for scientific experiments on biped locomotion and human-robot interaction. One of the main characteristics of this humanoid robot is that its anatomical proportions are bio-inspired. It is designed using the 3D printing technology with Polyamide material. POPPY uses a bio-inspired trunk system using five servomotors which allows the reproduction of the main DOFs of the human spine. This feature permits more natural fluid motion as well as allowing the spine to participate in the humanoid balance during bipedal walking and other activities[50].

ACROBAN the father of POPPY (figure 1.12b) has thirty degrees of freedom. Its height is about 70 cm. Acroban has the classical joints of humanoid robots, but in addition it includes a multi-articulated compliant vertebral column with five degrees of freedom [51].

HOPALALA (Humanoid Open Platform Aiming for Laboratories And Learning Affairs) is a kid size humanoid robot project started in 2016 by our team at LISV laboratory - Paris Saclay University (figure 1.12c). This robot is characterized by an anthropomorphic kinematic structure and intended to be an open platform for different kind of student. All the link of the robot are designed based on the plastic molding technology. In addition, Its spine is designed with 3DOF in order to be used as an experimental platform for trunk contribution research.

1.3 Conclusion

The projects we have presented show the growing interest of research and industry in the field of biped robots. The new humanoids increasingly resemble the human being and their ability to interact with it make these robots of choice as robots for companionship or entertainment.

In this chapter, we present the trunk's design of different robot. We have concluded that there are different ways of thinking about this part in humanoid robot. Some have

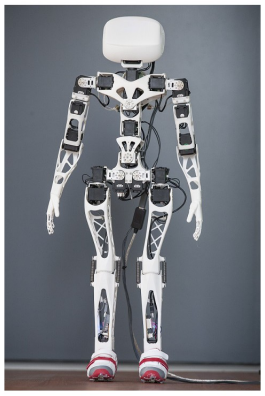

(a) POPPY

(b) ACROBAN

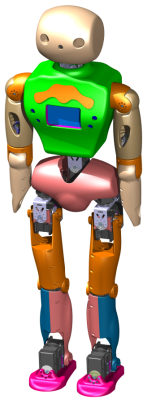

(c) HOPALALA

Figure 1.12: Kid size Humanoid

chosen to keep this part for storage of actuators or electronic equipment. Others, they thought to implement some degree of freedom in the lumbar part of the spine. The goal behind this is to give some flexibility for the upper part of the robot so that increase it workspace and affect on its dynamic manipulation. Others, they went to develop a very flexible spine so that they have a structure similar to the human spine.

The next chapter will concern in the effect of the spine to the robot mobility in order to obtain an optimized structure for the thoracic part of the humanoid robot HYDROïD.

Chapter 2

HYDROïD Vertebral Column Mechanism

Contents

In this Chapter, we will examine the effect of the vertebral column mobility on HYDROïD's workspace. To achieve this aim, a full human spine model was designed in MSC.ADAMS. This model was then simulated in the sagittal, transverse and frontal plane. The idea behind simulating a detailed human spine model is to examine the effect of each vertebra on the workspace and then, identify the performances of a simplified vertebral column for HYDROïD robot.

2.1 Workspace definition

The workspace of a robot is defined as being all the points reached by its end effector[52]. It is an essential term which gives an idea onto the working volume of a manipulator, and which must be taken into account at the beginning of the design phase. Although an exact calculation of the workspace boundaries stays a difficult problem, several methods try to determine them: analytical methods [53], and iterative and numerical ones [54].

2.2 Computational models of human spine

Biomechanical modelling of the human spine date back to the 17th century [55]. Different techniques have been used to model the vertebral column. The aim behind these models was in prior to estimate the spinal loading due to an external load and even to the body weight during dynamic activity. Equally important, was to study how the spine

behaves to the physical stability and estimate of risk of injury through biomechanical modeling.
Computational human spine model can be categorized into four groups based on the used technique: (i): Analytical , Geometric, Pivot, and Continuum Models such as[56, 57, 58, 59], (ii): Multibody model such as [60, 61, 62], (iii): Finite element model such as [63, 64] and finally (iv): Hybrid multi-body FE models such as [65].

In order to establish a kinematic model for the spine, it was essential to create a detailed model of the spinal column allowing us to analyze its effect on the work space. For this, a multi-body model will be presented in the next section.
By definition, A multi-body system is a group of rigid bodies connected through kinematic joints. More the mechanical properties of the bodies and the joints are well implemented, more the system is realistic.

2.3 Multi-Body model development

In order to obtain a reliable model that can replicate the complex motion and nature of the human spine, each part of the spine must be modeled taking into consideration it geometrical, inertial and mechanical properties.

2.3.1 Vertebrae Geometry

The vertebra geometry is typically obtained from CT scans by using cadavers and recording the coordinates of each vertebra. The method relies on accurate sample preparation and many input points to obtain a solid.
The most complete data collection was done by Panjabi et al. [3, 66] who wrote series of articles about the geometrical data of the spinal vertebra in the different regions of the vertebral column.

2.3.2 Vertebra Position

As it was stated in chapter one, the initial posture of the human spine is characterized by a kyphotic curve in the thoracic spine and a lordotic curve in the lumbar spine.

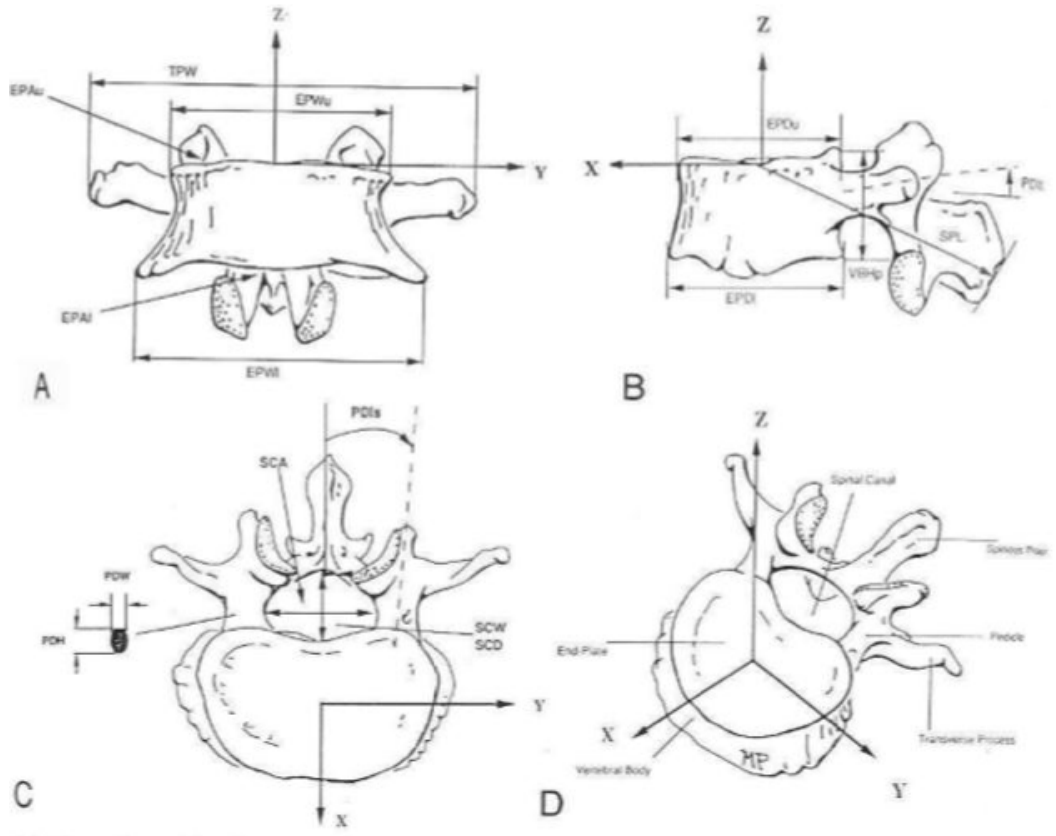

Figure 2.1: Orthogonal views for lumbar vertebrae [3]

Therefore the initial positions of the vertebrae must be taken into consideration to create the appropriate initial shape of the human vertebral column. The vertebrae positions were derived from [7] and listed in the table 2.1.

2.3.3 Inertial properties of vertebra

In order to improve the reliability of the spine model, hence improving the simulation precision, the masses and moments of inertia of each Vertebra were defined.
The inertial properties were derived from [8] after measurement for a 35 fresh adult cervical spine motion and introduced in the spine model (table 2.2). These value are considered as the nominal value corresponding for HYDROIïD dimensions.

Table 2.1: Vertebrae body and Intervertebral disc centroid coordinate defined relative to the posterior-inferior corner of the S1 vertebrae for an adult [7]

	VB Centroid		IVD Centroid	
Vertebrae	X(mm)	Y(mm)	X(mm)	Y(mm)
T1	-6.81	472.76	-11.03	482.65
T2	1.49	452.90	-2.78	463.16
T3	9.16	432.31	5.71	443.06
T4	15.36	410.84	12.94	422.11
T5	20.00	388.11	18.60	399.86
T6	22.70	364.75	22.18	376.63
T7	23.29	340.54	23.88	352.79
T8	21.13	315.73	22.81	328.24
T9	16.9	290.37	19.14	303.29
T10	11.10	263.92	13.95	277.57
T11	3.48	235.71	7.26	250.24
T12	-6.77	205.81	-2.11	221.32
L1	-18.83	174.14	-14.09	190.80
L2	-31.86	139.94	-27.09	157.90
L3	-42.37	103.01	-39.59	122.06
L4	-46.73	64.66	-47.58	83.76
L5	-41.20	27.12	-47.89	44.96
S1	-20.14	-2.13	-35.53	8.31

2.3.4 Ligament Properties

For each vertebra in the spine model six ligaments were modeled as springs, with the damping and stiffness coefficients defined according to [9] (table 2.3).

A 3-D CAD model of the segments of the lumbar and thoracic spine were established. The vertebrae were designed into CATIA V5 software and the model of the spine was build into Adams/views (Figure 2.2).

2.3.5 Range of motion

Between two adjacent vertebrae, a spherical joint was created to generate rotational motion around the x, y and z axis. However during the simulation, range of motions must be respected in all the planes of motions and for all the vertebrae, according to

Table 2.2: Inertial properties of vertebrae [8]

		Momoent of Inertia		
Vertebrae	Mass (g)	Ix (g.mm$\hat{2}$)	Iy ($g.mm^2$)	Iz ($g.mm^2$)
T1	40.3	9093.9	9937.95	14545.2
T2	40	7128.15	9721.95	12623.55
T3	48.5	9570.75	13664.55	17698.5
T4	55.9	11912.25	17352	22233
T5	56.3	11804.1	17302.5	22215
T6	60.8	12942	22192.5	27441
T7	62.4	13263	22480.5	27634.5
T8	68.4	15633	22884	29808
T9	73.3	16186.5	24618	31246.5
T10	88	20677.5	32013	37747.5
T11	89.3	20241	34623	40461
T12	89.3	20220	34683	40452
L1	89.7	21642	33895.5	40257
L2	86.4	20587.5	33579	39921
L3	95.9	24291	39938.5	46333.5
L4	96.8	24697.5	39570	46929
L5	84.1	21019.5	28614	37368
Sacrum	250.1	299895	170518	207240

Table 2.3: Stifness and damping properties for lumbar ligaments [9]

Ligament	Spinal Region	Stiffness (N/m)	Damping (N.s/m)
CL	Lumbar	33900	0.4
LF	Lumbar	27200	0.4
ISL	Lumbar	11500	0.4
SLL	Lumbar	23700	0.4
ALL	Lumbar	33000	0.4
PLL	Lumbar	20400	0.4

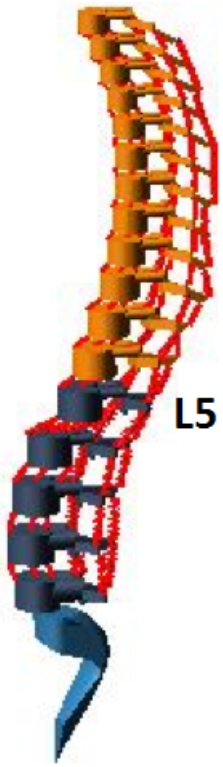

Figure 2.2: Human spine model - Adams/view

figure 2.3.

2.4 Workspace simulation and analysis

Using this human spine model, simulations were conducted to examine the workspace in each plane of motion and investigate the effect of each vertebrae and each spinal region on the workspace.

As we are interested in the manipulation and co-working tasks, the end effector for each plane was chosen to be the point representing the hand of the HYDROïD robot. This point is localized using the lengths of the robot arms.

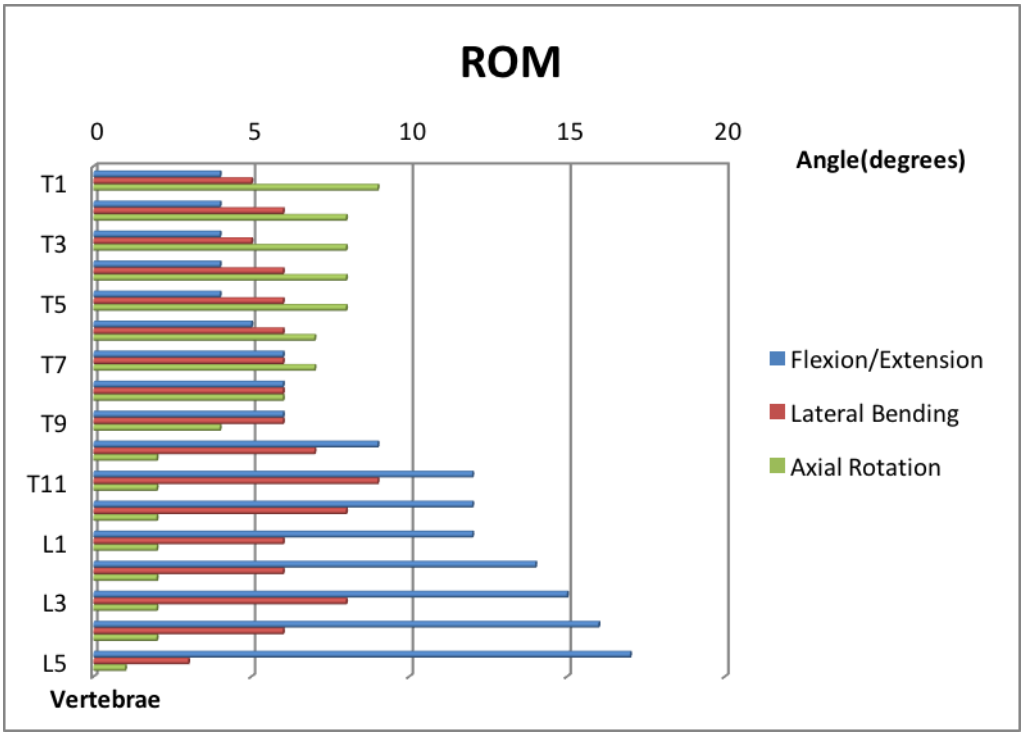

Figure 2.3: Range of motion of some Vertebrae

2.4.1 Sagittal plane

First a marker representing the end effector was introduced in the sagittal plane. This marker trajectory was traced during each simulation to examine the workspace of the HYDROïD robot. The maximum angle of flexion/extension was introduced to every vertebra in the model using the STEP function to create maximum bending of the spinal model. This simulation was repeated after blocking the motion in each joint to investigate the effect of each vertebra on the workspace in the sagittal plane. Furthermore, a simulation was made with the whole thoracic region fixed and another one with the whole lumbar spine fixed to investigate the effect of spinal regions on the workspace.

Figure 2.4 shows the curves representing the marker trajectories in all simulations. These curves data were exported and analyzed, where comparisons were made between data sets in order to derive valuable conclusions.

Figure 2.5 represents the maximal workspace in the sagittal plane in the cases where

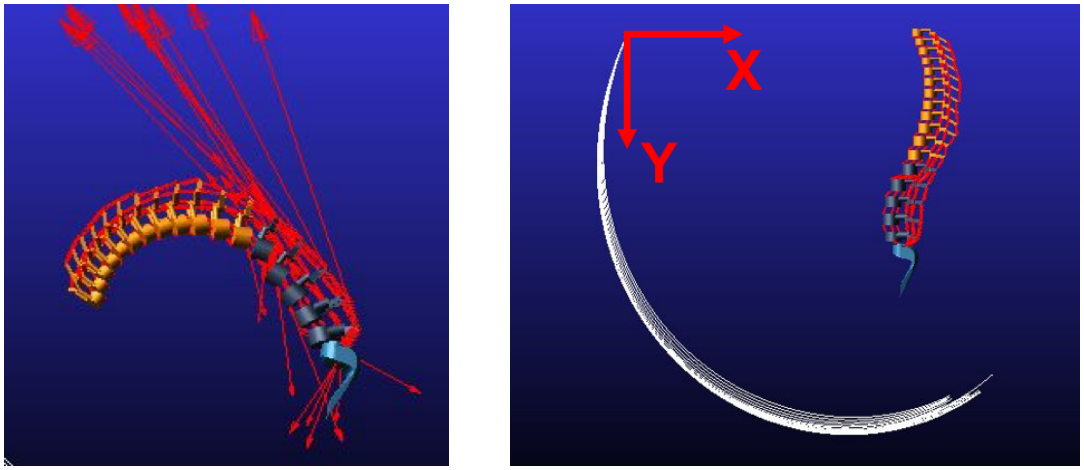

(a) Maximum Bending for the spine

(b) Diffrent simulations and workspaces

Figure 2.4: Simulation of human spine

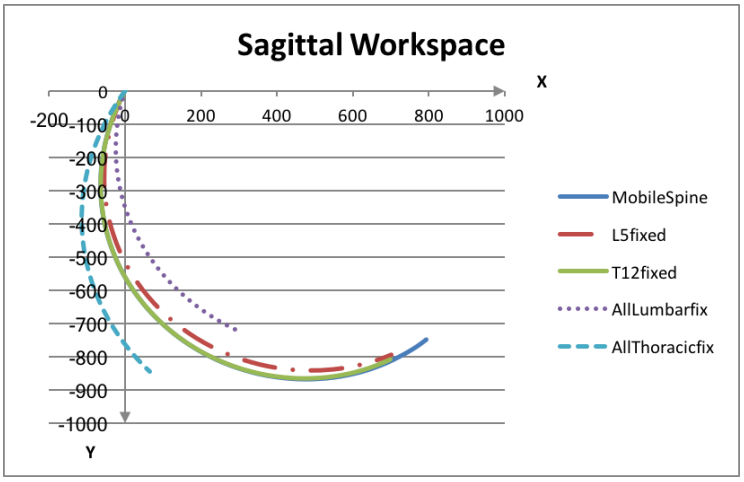

Figure 2.5: Curves analysis - Sagittal Plane

all the spine vertebrae are mobile, where the vertebra L5 is fixed, where the twelfth thoracic vertebra is fixed, where the entire lumbar spine is fixed and when the whole thoracic spine is fixed. The point (0 , 0) represents the initial coordinates of the end effector. For robotic bi-manual application, we are interested in expanding the workspace along the negative X direction (figure 2.6) shown in figure 2.5 by using the vertebral column flexibility. Little importance is given to the expansion of the workspace along the Y direction because this work area can be cover by using HYDRïOD's arm and knee

structures rather than the spine. Analyzing the curves in Figure 2.5, we noticed that when L5 is fixed, the boundary of the workspace in the sagittal plane decreased compared to the case when all vertebrae are mobile. Furthermore, this workspace largely decreases when the entire lumbar region is motionless. These observations outline the importance of the motion of the lumbar region regarding the expansion of the workspace in the sagittal plane. On the other hand, we can notice that when T12 is fixed a slight increase in the workspace is observed. However, this workspace is highly expanded when the entire thoracic spine is fixed. To quantify the effect of the lumbar and thoracic spine mobility on the robot workspace in the sagittal plane, we have constructed a chart that represents the gain of the boundary of the workspace in the case of each vertebrae being fixed. The chart is shown in Figure 2.7. The value of this gain designates the ratio between the maximum value in negative X direction of each simulation to its value when all the spine is mobile.

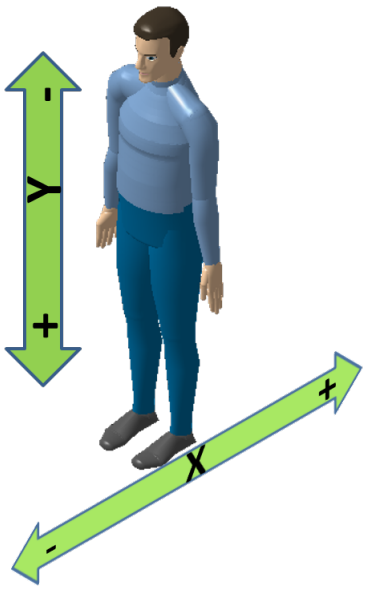

Figure 2.6: axis direction

A gain value of 100 corresponds to the workspace when none of the vertebral column elements are fixed. The value of the gain decreases below 100 and it reaches its minimum when the entire lumbar spine is fixed. The gain value increases above 100 during the cancellation of the thoracic vertebrae motion until it reaches its maximum

when the whole thoracic spine motion is canceled. We can conclude that, to maximize the boundary of the workspace in the sagittal plane, the motion of the lumbar spine is inevitable. Moreover, the most critical vertebra of the lumbar spine is L5. Furthermore, the previous results showed that a relative rigidity in the thoracic area of the vertebral column is very useful in the context of workspace expansion in the sagittal plane (Figure 2.7).

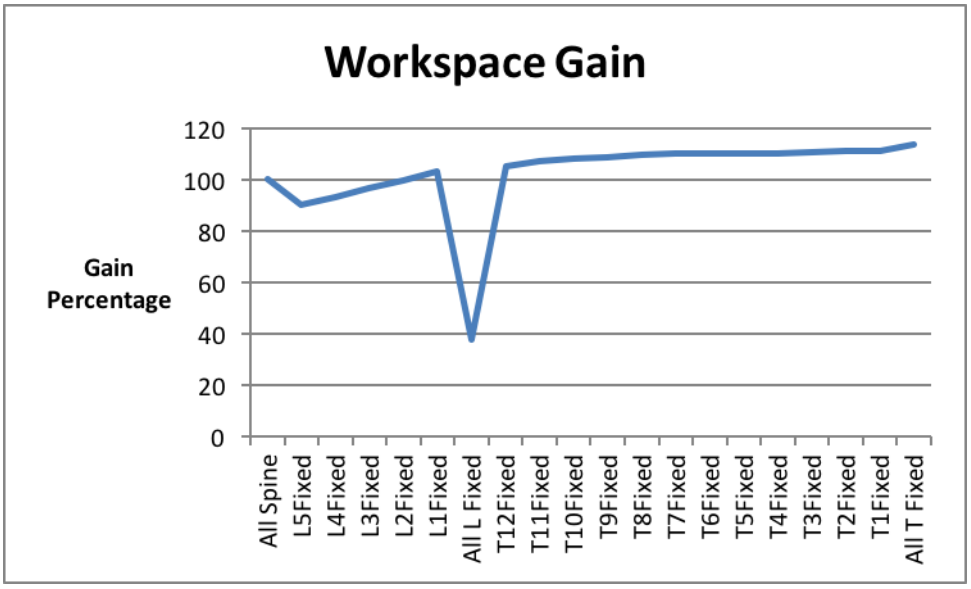

Figure 2.7: workspace gain - Sagittal plane

Conclusion

We can conclude from the previous section that the lumbar part of the spine has an effective and dominant role on the working space especially at the level of L5 vertebra, where the gain reach its minimal value (Figure 2.7). Hence, a degree of freedom in the sagittal plane and at the level of L5 will be a major asset. On the other hand, the complete fixation of the thoracic part increase the possibility of holding upstream of the robot. Nevertheless, this rigidity will move the workspace towards the front and so on. It leaves the arms to cover the manipulability in the area closest to the robot. Thus, an optimal solution is to leave a slight mobility in the thoracic region which will simplify the kinematics of the arms without leaving a major difference in the gain of the

workspace Figure 2.5. Hence, a second degree of freedom in the sagittal plane should take place between the T8 and T12, depending on the mechanical constraints.

2.4.2 Transverse plane

The same steps in the analysis of the workspace in the sagittal plane were made to derive valuable conclusions regarding maximization of the workspace in the transverse plane. A marker representing the end effector was introduced in the transverse plane; this marker trajectory was traced during each simulation to examine the workspace of the robot arm. The maximum yaw angle was introduced to every joint in the model using the STEP function to create maximum axial rotation of the spinal model. Similarly to the sagittal plane, the vertebrae motion was blocked one by one to highlight the effect of every vertebra on the workspace in the transverse plane. Furthermore, the motion of the entire lumbar and thoracic part of the vertebral column was eliminated. The curves derived from simulations were exported and comparisons were made.

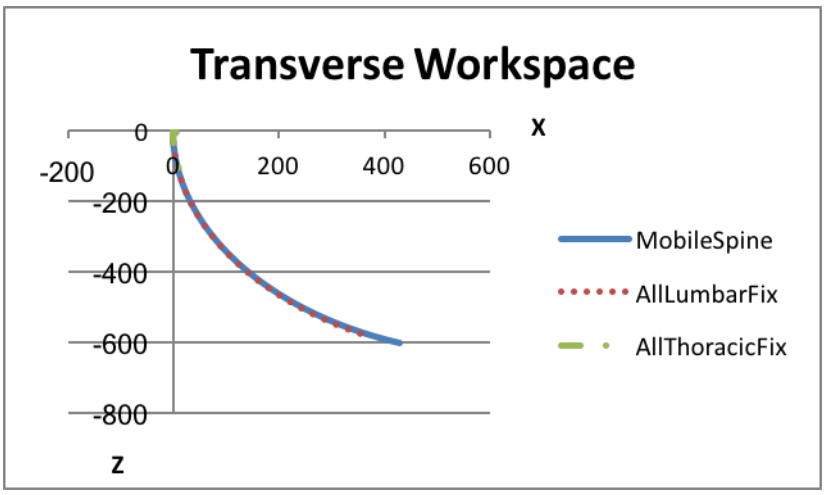

Figure 2.8: Curves analysis - Transverse Plane

Figure 2.8 represents the workspace in the transverse plane in the case where all the vertebrae are mobile, the case where the lumbar spine is fixed and the case where the thoracic spine is motionless. From Figure 2.8, it is highly remarkable that the rigidity of the lumbar spine doesn't affect the workspace in the transverse plane, as the curve

corresponding to the case where the lumbar spine is fixed nearly coincides with the one corresponding to the fully articulated spine. Using the same method to calculate the boundary gain, we obtain that the workspace in the transverse plane loses around 82% of its value when the thoracic spine is maintained fixed. However we noticed from the range of motions in figure 2.3 that the lumbar spine rarely contribute to the rotation around the vertical axis; most of the rotation in the transverse plane is derived from the thoracic region of the spine. This statement is in perfect agreement with the conclusions derived above regarding the workspace in the transverse plane.

2.4.3 Frontal Plane

The same analysis was conducted to optimize the workspace in the frontal plane. A marker representing the end effector was introduced and its trajectory was traced during all the simulations that were done in the same methodology applied in the sagittal and transverse plane in order to highlight the contribution of each vertebra to the workspace maximization. Here, the maximum roll angle has been used in the step function to create the maximum lateral flexion.

Figure 2.9 represents the workspace in the frontal plane in the cases were all vertebrae all mobile, L5 is fixed, the entire thoracic spine is fixed as well as the case were the whole lumbar spine is fixed. In order to quantify the effect of various spinal segments on the frontal workspace, we have constructed the chart in figure 2.10 representing the workspace gains in the different cases were vertebrae motions are eliminated.

We can notice from figure 2.10 that when the lumbar spine is motionless, the workspace decreases in both the Y and Z directions. On the other hand when the thoracic spine is fixed, an increase in the workspace in the Z direction is noticed but a 50% decline in the workspace in the Y direction is also remarkable in this case. Having simulated the maximum motion of the spine in the three motion planes, and eliminated each vertebra during the process, we conclude that the inclusion of the spinal motion in the lumbar area is inevitable in HYDROïD's spinal column configuration. Furthermore we conclude that a relative rigidity in the thoracic spine is useful for the expansion of HYDROïD's workspace.

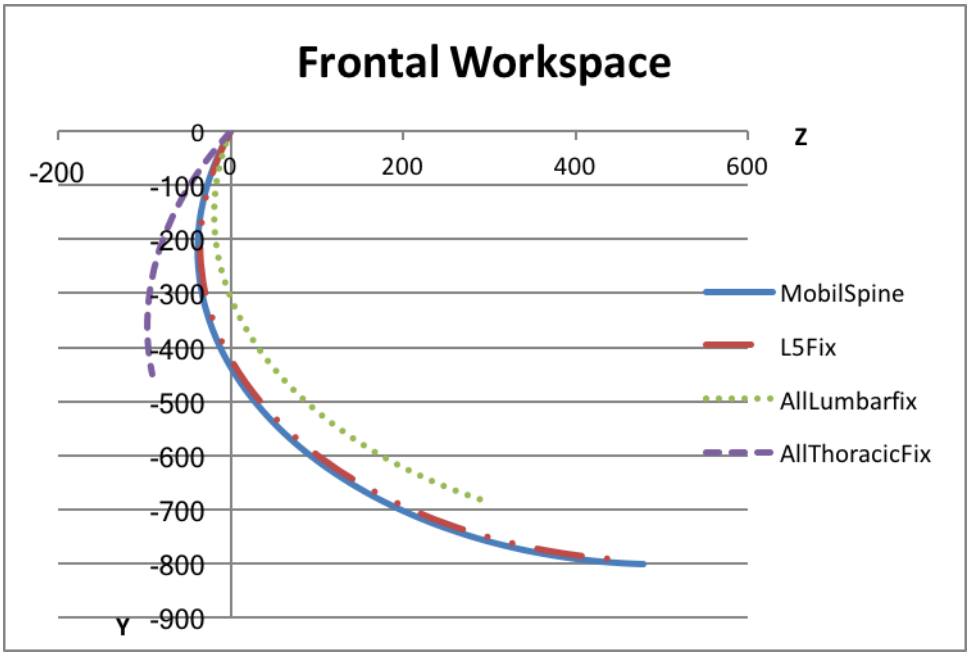

Figure 2.9: Curves analysis - Frontal Plane

These conclusions validate the architecture of HYDROïD's vertebral column having four degrees of freedom distributed as follow: 3 DOF (Roll, Pitch, Yaw joints) localized in the base of the lumbar part directly above the pelvis and 1 DOF (Pitch joint) in the base of the thoracic part. In the next section, we look to validate even more this architecture, by investigating one of the principle activities of humanoid robots; that is walking.

2.5 Vertebral Column and Gait Cycle

In order to outline the role of the spine in the walking cycle, we have in first place investigated researches that studied the gait cycle of patients suffering from Ankylosing Spondylitis [67].

Ankylosing Spondylitis is a form of arthritis that affects the joints in the spine. Its name comes from the Greek words ankylos, meaning stiffening of a joint, and spondylo, meaning vertebra. Spondylitis causes inflammation (redness, heat, swelling, and pain)

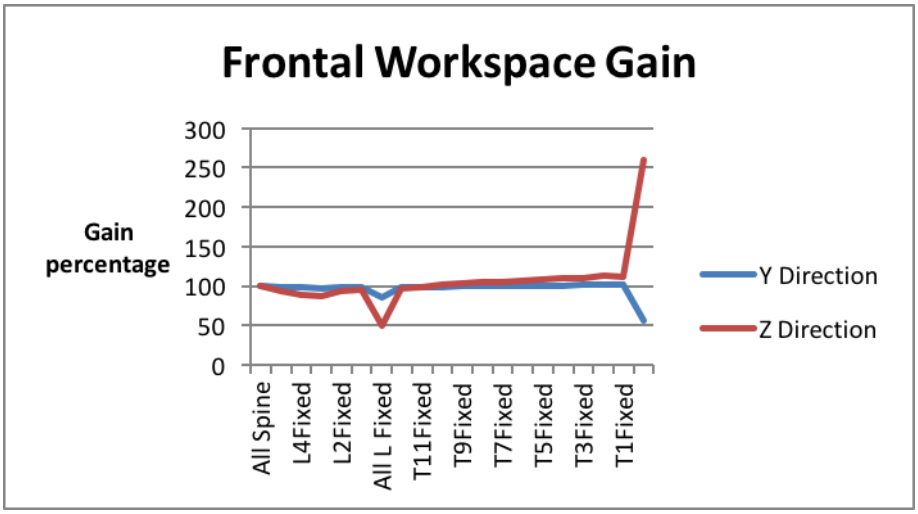

Figure 2.10: workspace gain - Frontal plane

in the spine or vertebrae. This disease causes vertebrae to fuse together imposing rigidity on the spine [68].
A group of Ankylosing Spondylitis patients participated walking trials during which kinematic and dynamic measurements were done to determine the angular displacement and moments at different lower parts joints[67]. These measurements were compared with identical ones done for a group of non-affected people and the results were compared.

The results showed that the angles for the movement of the hip and knee were less in patients with Ankylosing Spondylitis and the stride length was shorter for these patients together with many abnormalities in different parameters. Furthermore, the mean value of the trunk, knee and ankle torque were higher in the case of Ankylosing Spondolytis. These observations highlight the importance of the spinal motion during gait cycle. Furthermore, by making a primal analogy with robotics field, we assume that having a relative flexibility in the humanoid vertebral column leads to the reduction of energy consumption during walking cycle.

In a second approach, we investigated a study that treats the walking cycle of subjects wearing a fiberglass body jacket like a Thoracolumbosacral Orthosis(TLSO) hence studying the effect restricted spinal motion on gait [4]. A Thoracolumbosacral Orthosis

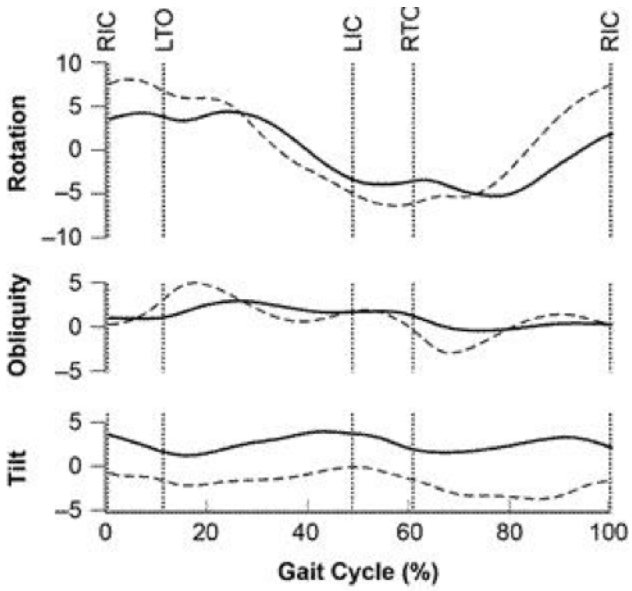

Figure 2.11: Pelvic motion pattern for one walking trial, unrestricted (dashed line, 1.34 m/s) and restricted (solid line, 1.45 m/s). RIC = right initial contact, LTO = left toe off, LIC = left initial contact, RTO = right toe off [4]

(TLSO) is one of the two main types of braces used to correct the lateral (sideways) curve of the spine in scoliosis.

Subjects wore the body jacket and walked in five different speeds, while kinematic joint measurements were taken. The same experiment was repeated without the body jacket and the set of results were compared. The first significant observation was that subjects wearing the jacket walked slower and increased their base of support. This highlights the contribution of spinal motion in maintaining balance during walking. The results of this study, as shown in Figure 2.11, demonstrated that when spinal motion was restricted pelvic obliquity and rotation were reduced along with the hip abduction-adduction motion. These findings validate the conclusion derived previously regarding humanoids and help to further outline the importance of upper body design improvement in the robot development.

2.5.1 Robotic studies

Recently there has been a growing interest in the energy efficiency of bipedal walking robots. However, the spinal effect on walking has been rarely widely investigated in these studies. One of the studies was done on the biped Robot WABIAN-2 [69] which architecture was discussed in chapter one of this report. This study investigated the effect of spinal motion on the energy efficiency of the bipedal during gait cycle. A systematic technique is presented to compare the energy efficiency of the wabian robot walking with different styles of spinal movement. To investigate the effect of an articulated spine on energy efficiency during walking, at the beginning of each simulation, they varied the spine curvature gain factor, which affect the amount of bending of the joints in the torso. After walking eight steps with 100 mm of length, they recorded the torque and the angular velocity of all the body joints. Finally, they computed the total energy consumption required by the robot during walking at different spine curvature gains and they compared it to that required by its rigid-torso counterpart. Simulation results show that with the additional lateral degrees of freedom in the torso, the humanoid requires 26.5% less energy than its conventional rigid-torso counterpart to complete the same walking task[69]. Interestingly, this happens when the robot is walking with swaying hips.

By investigating the effect of restricted spinal motion in human locomotion and looking at the effect of Ankylosis Spondylitis we can deduce that the human spine is not a passive mechanism during walking cycle. This point was further validated by the encouraging results obtained from the simulation done on the humanoid WABIAN-2. However, the ideal scenario will be to replicate all the human vertebral column degrees of freedom in the robot torso. But this approach will not be adopted taking into consideration the redundancy of the human spine and the complexity of algorithms required to control a very sophisticated spinal architecture. Furthermore, this point of view is supported by the fact that the humanoids of the University of Tokyo, having very flexible spines, couldn't stand up or walk without external support. Therefore, in the following sections, we will investigate the importance of the spinal mobility on the energy efficiency and balance during walking cycle, in order to derive valuable conclusions

regarding HYDROïD's vertebral column architecture.

2.6 Dynamic Analysis of Gait Cycle

2.6.1 Introduction and methods

The goal of this section is to study the effect of spinal motion on HYDROïD's energy efficiency. Therefore, a mathematical model of human gait would be presented. On the other hand, there are 20 or more degrees of freedom involved in human walking motion. The inclusion of these degrees of freedom into the model will be problematic. Thus, the human model for the gait analysis must be as simple as possible. Initially a seven-link gait model constrained in the sagittal plane was developed, and then another degree of freedom was added to this model, in the upper part, resulting in an eight-link model. The Lagrange formulation was applied to both models to derive torques in each joint. The set of results were compared to derive conclusions. The analysis of both models will be discussed in detail in this section.

2.6.2 Seven - link model

The humanoid biped is modeled as the seven-serial links mechanism in the sagittal plane as shown in figure 2.12

The seven links consists torso (link 4) and three links in each leg which are thigh (links 3 and 5), shank (links 2 and 6) and feet (links 1 and 7). These links are connected via rotating joints which are two hip joints, two knee joints and two ankle joints. The joints are assumed to be friction-less and each one of them is driven by an independent actuator.

From figure 2.12, the parameters of the biped model are shown as follows:

- m_i: mass of the link.
- L_i: Length of the link.

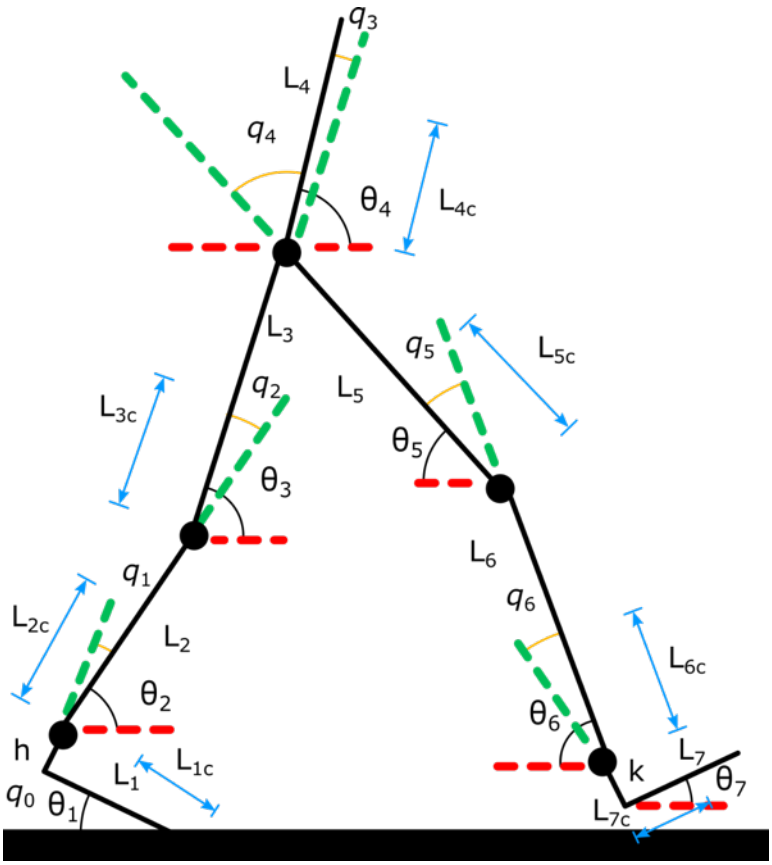

Figure 2.12: seven link model

- L_{ic}: Distance between the center of mass and the lower joint of the link.
- θ_i: angle of the link with respect to the horizontal axis (absolute angle).
- q_i: Relative angle deflections of the corresponding joints.

The masses of the links were defined in an adequate matter respecting the average human being body weight distribution. Similarly, human morphology was taken into consideration during the links length definition.

These Data are presented in table 2.4.

The coordinates of center of mass of each link were then computed. The corresponding equations are presented at Appendix A.

Table 2.4: Mass and Length of each link

Link	Mass (Kg)	Length (m)
1	1.11	0.25
2	3.6	0.425
3	7.45	0.435
4	48	0.52
5	7.45	0.435
6	3.6	0.425
7	1.11	0.25

Dynamic model

The dynamic equations of a robot can be acquired by using Lagrange's equations. In this study, the biped dynamic model is further simplified by considering only the single-leg support phase. As shown in Figure 2.12, in this phase only the supporting leg of the biped is in contact with the ground while the other leg is swinging in the midair in the forward walking direction.

The Lagrange equation of motion can be written in the following form:

$$\frac{d}{dt}\left(\frac{dL}{d\dot{\theta}_i}\right) - \frac{dL}{d\theta_i} = \tau_i \tag{2.1}$$

Where $L = K - P$, K: Kinetic Energy and P: Potential energy.

The Kinetic energy of each link was calculated using the center of mass coordinates of the links and the moments of inertia and masses of the links using the following equation:

$$K_i = 0.5 m_i (\dot{x}_{ci}^2 + \dot{y}_{ci}^2) + 0.5 I_i \dot{\theta}_i^2 \tag{2.2}$$

The Potential energy of each link was calculated by the following relation:

$$P_i = m_i g y_i \tag{2.3}$$

The Lagrange equation was applied to derive the torque expressions with the help of Maple15.

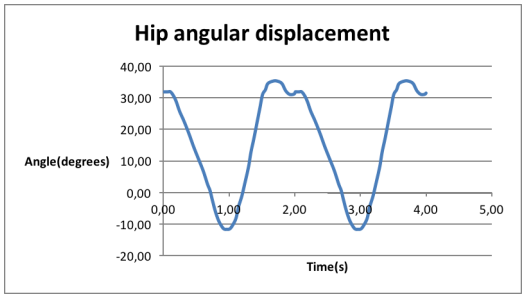

(a) Hip displacement

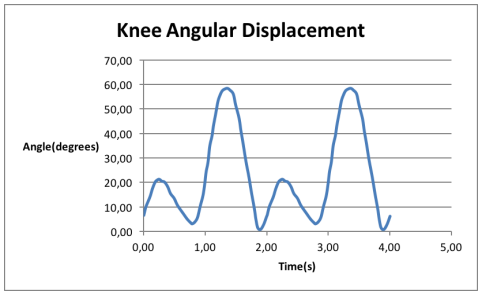

(b) Knee displacement

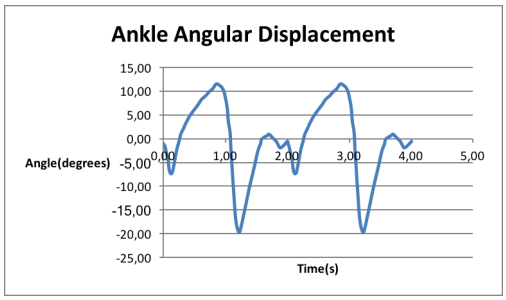

(c) Ankle displacement

Figure 2.13: Angular displacement for Hip, Knee and Ankle

Angles Calculation and Measurement

The relative motion angles are measured in various studies using motion captures technologies such as VICON tracker software. These Data were retrieved from a campaign of specific measures, conducted by members of the team at R. Poincaré Hospital in Garches. The motion analysis system which is equipped with the gait analysis platform of this hospital has allowed several tests to be analyzed with speed ranges close to those desired for the HYDROïD robot. The measurements derived were for the ankle, knee and hip of the supporting leg (Figure 2.13). To obtain the data for the swinging leg, these set of data were shifted 50% of the gait cycle time. Having the relative angles, we can compute the absolute motion angles using the relations presented at Appendix A.

The relative angles were extended to two gait cycles which results in a total time of four seconds. The angular displacements of the right limbs are given in the following charts.

Torques calculation

The goal is to estimate the torques at each joint during the gait cycle, more precisely during the single support phase of this cycle. Having determined the absolute angular displacement at each joint after the measurement of the relative angles, the next step was to derive the angular velocities and accelerations.
The torque expressions obtained in Maple15 were exported in MATLAB using the Maple Code Generation library. Having computed the torque expressions at each joint, the angular displacement, velocities and accelerations, as well as the geometrical and inertial parameters of each link; the torques can be computed in Matlab and their variations during gait cycle can be plotted.
The set of obtained data will be compared with the one obtained by applying the same analysis to an eight degree of freedom model. This biped model will have an additional degree of freedom in the vertebral column. This model will be further detailed in the next section.

2.6.3 Eight - link model

An eight link was added to the seven-link biped model discussed above to form the eight degree of freedom model. The additional degree of freedom was added in the sagittal plane at the thoracic level of the model.

The humanoid biped is modeled as the eight serial links mechanism in the sagittal plane as shown in figure 2.14. The links are identical to the seven-link model with the exception of the additional link 8 representing the second link of the torso. Similarly to the seven link model, the links are connected via rotating joints which are two hip joints, two knee joints and two ankle joints. The joints are assumed to be friction-less and each one of them is driven by an independent actuator.

The masses and lengths of the links remained unchanged, except for links 4 and 8. The geometrical and inertial parameters of these links were defined in an adequate way with the placement of the additional torso degree of freedom, which is at the thoracic level (around T3).

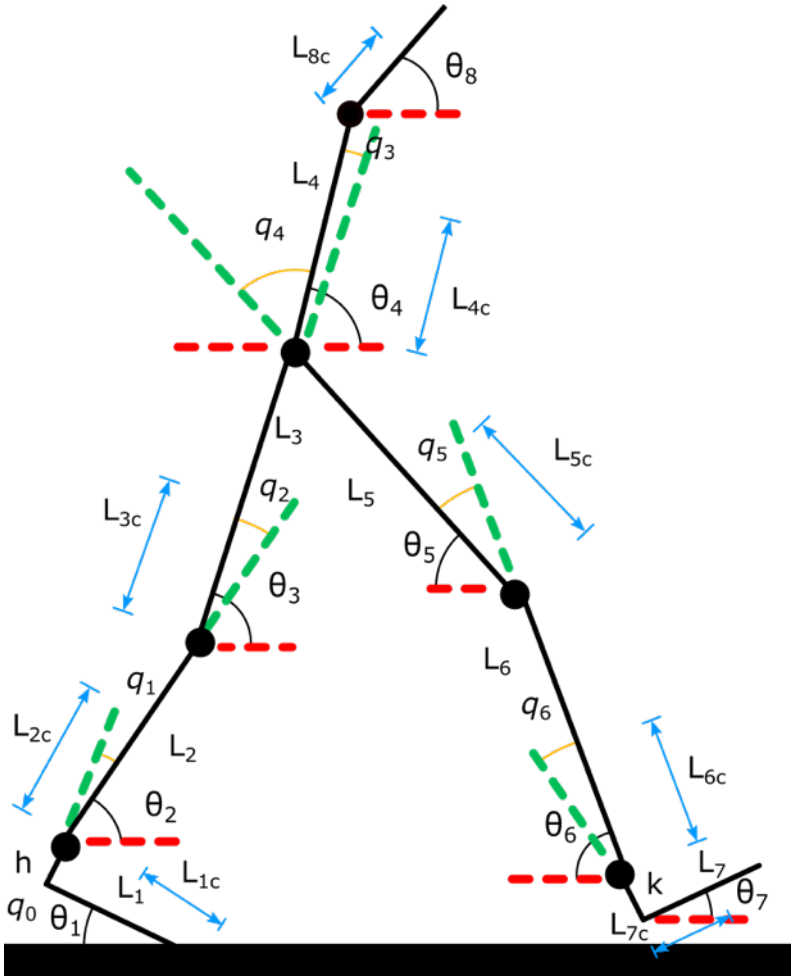

Figure 2.14: Eight - link model

The coordinates of center of mass of each link are identical to the ones computed for the seven link model, with the addition of the eight link center of mass coordinates. The 8-link model has the same mass (same mass for the trunk also), and the same center of mass, for valuable comparison. These coordinates are defined as follows:

$$x_{8c} = -l_1.cos(\theta_1(t)) + h.sin(\theta_1(t)) + l_2.cos(\theta_2(t)) + l_3.cos(\theta_3(t)) + l_4.cos(\theta_4(t)) + l_{8c}.cos(\theta_8(t))$$

$$y_{8c} = l_1.sin(\theta_1(t)) + h.cos(\theta_1(t)) + l_2.sin(\theta_2(t)) + l_3.sin(\theta_3(t)) + l_4.sin(\theta_4(t)) + l_{8c}.sin(\theta_8(t))$$

Table 2.5: Mass and Length of link 4 and 8

Link	Mass (Kg)	Length (m)
4	36	0.42
8	12	0.1

Dynamic model

The same calculation method used in the seven-link model was used in the eight-link model. The same Lagrange equation is used, with the addition of the parameters and equation of the added torso DOF.

Angles Calculation and measurement

As presented in the previous section the relative angles measured for the motion of the limbs are converted into absolute angles and used for the first seven links of the eight degree of freedom biped model. However, the absolute angle which represents the absolute motion angle for link 8 is directly obtained from [70]. The data representing the variation of this angle during gait cycle was extended to two gait cycles.

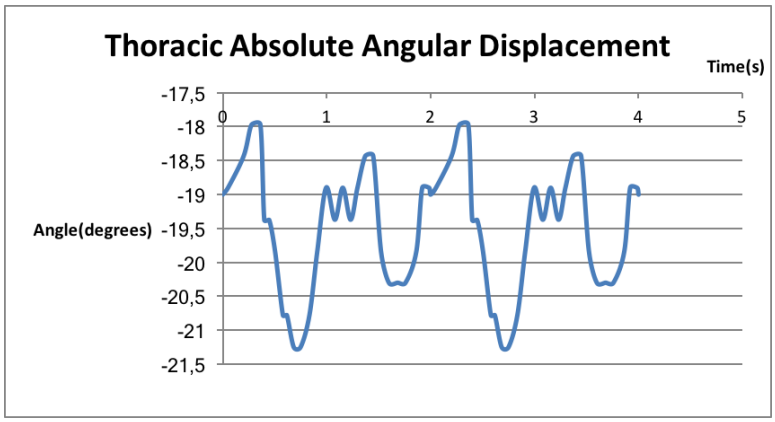

Figure 2.15: Thoracic angular displacement

2.6.4 Data Analysis

In the previous sections we detailed the calculation process of the generalized torques at the joints of a seven link biped walking model and an eight link biped walking model. However, the goal behind this dynamic walking analysis is to examine the effect of the additional degree of freedom in HYDROïD's vertebral column on the robots energy consumption during gait. Therefore, we calculated the percentage of gain in the torques of each joint resulting from the inclusion of the additional torso degree of freedom. The mathematical formula used to achieve this purpose is the following:

$$G_i = \frac{|\tau_{qia}| - |\tau_{qi}|}{|\tau_{qia}|}.100 \tag{2.4}$$

with τ_{qia} : Torque at joint i for the seven-link biped model and τ_{qi} : Torque at joint i for the eight-link biped model.

The gain was calculated at each moment of the gait cycle, then the average gain of each joint was calculated. The results are presented in the following table.

Table 2.6: Torque Gain

Joint	Gain (%)
Support Toe	4.5
Support Ankle	1.4
Support Knee	1.6
Support Hip	5.5
Swinging Hip	3.4
Swinging Knee	3.29
Swinging Ankle	18.1

From table 2.6, we can conclude that a non significant gain was observed in the support ankle and knee. however, this gain increases to around 5% for the support toe. As for the swinging leg the most significant gain is observed in the ankle, were it reaches 18%. However, the absolute value of the torques at this joint is lower than the other joints specially those of the supporting leg. Therefore we should not be deceived by the relatively high value of this gain.

2.7 Torso additional DOF motion variation

In the previous section we have proved the advantage of having an additional sagittal degree of freedom in HYDROïD's vertebral column on the torque gain in the different lower limb joints. In this section, we look to maximize the utility of this degree of freedom by modifying its motion. The function that was used to replace the previous function corresponding to the human thoracic spine motion is a periodic sin function. The function has the amplitude -19deg corresponding to the mean value of the previously used motion input. The frequency of the sinusoidal functions was varied and for each frequency the torque gains in the supporting lower limbs were collected.

The used functions can be written in the following form: $f_i = -19.\frac{Pi}{180}.sin(i.t)$

The results of the torque gains are presented in the table 2.7 and in figure 2.16(H.O represents human oscillation).

Table 2.7: Support Limbs gain variation

	Human motion	f_1	f_2	f_3	f_4	f_5	f_6	f_7	f_{10}
Support Toe	4.5	4.298	4.25	4.2	4.3	4.22	4.34	4.23	3.93
Support Ankle	1.4	1.2709	1.2	1.16	1.46	1.85	3.21	0.0328	0.2071
Support Knee	1.6	1.62	1.56	1.73	1.9	2.33	4.86	-0.82	-0.36
Support Hip	5.5	5.06	5.04	4.99	6.37	5.86	8.47	3.92	2.83

However, in the robots architecture, the ankle, knee and toe joints are more critical than the hip joint; knowing that, in the later, bigger actuators can be implemented. Therefore, improving the ankle, knee and toe joints gains should be of primary importance. Furthermore, the data of table 2.7 indicates that the gains in the ankle and knee joints should be improved as their values are small compared to the hips and toe joints gains. We can conclude that by increasing the frequency of the sinusoidal function, the ankle and knee gain increase reaching their maximum for the function f_6(frequency=$\frac{6}{Pi}$). By increasing the frequency even more, the gains in the lower limb joints decrease.

Therefore we choose the function $f_6 = -19.\frac{Pi}{180}.sin(6.t)$ as an input for the additional sagittal degree of freedom. Having chosen this function, the gain in the ankle joint is increased from an initial value of 1.4% to 3.21%. Similarly the gain in the knee

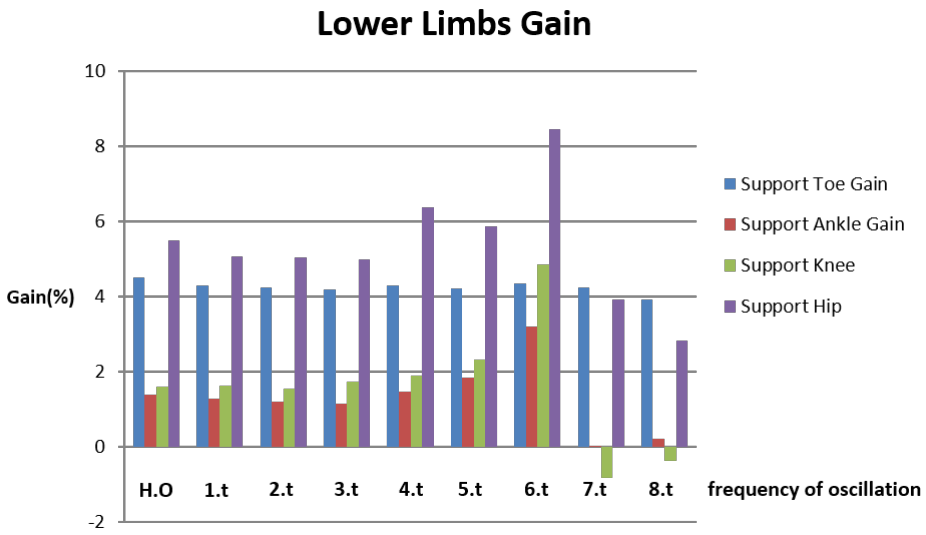

Figure 2.16: Lower Limb gain

joint is increased from 1.6% to 4.86% and the gain in the hip joint is increased from 5.5% to 8.47%. On the other hand, the gain in the toe joint is slightly decreased, but this decrease is insignificant (0.16%).

2.8 Conclusion

In this chapter, we have highlighted the advantages of HYDROïD's vertebral column architecture having four degrees of freedom. We have first proven that this structure insures a wide workspace for the robot. Second we showed the importance of the additional sagittal degree of freedom by investigating its effect on reducing torques on the lower limbs during gait cycle. However this work opens several perspectives. From the mechanical point of view, it is important to study the feasibility of the vertebral column of the humanoid robot. On the other hand, it is also important to maximize the advantages of this structure by implementing the right control algorithm.

Chapter 3

Kinematic Structure for the trunk of HYDROïD

Contents

3.1 Kinematic synthesis

To tackle the drawback related to the smallness of the workspace of a parallel mechanism while taking advantage of the rigidity of such structure, the new concept of "hybrid" mechanism introduced in [13] can be used. It consists of splitting the 3-DoF

mechanism in two subparts, one of which is serial and the other fully parallel. The association in the same mechanism of serial and parallel parts was not intensively used in humanoid robotics field. Indeed, hybrid mechanisms are able, through their serial and fully parallel parts, to achieve optimal performances under the constraints involved in humanoid robotics field mainly the compactness and the notable difference in ranges of motion of a body in the three directions (pitch, yaw and roll). As mentioned in [13], the external shape of a humanoid robot is important when the aim is to achieve helpful interactive tasks with humans. To increase the acceptance criterion, we pursue our target of designing "slim and smart" mechanisms for the several joints of the HYDROïD humanoid robot. Thanks to the modified Hanavan model, we could get the dimensions, masses, and center of mass positions of the limbs of Torso mechanism. The parameters used to define the placement of the torso, concern the chest and the pelvis for the torso. As a first approximation, the chest and the lower part of the pelvis have to be included in parallelepipeds whose main dimensions are given in Table 1. Thus, the first 3DOF of the Torso have to be included in the narrow space that is defined. This geometrical constraint, far from being consistent with the structure of a fully parallel mechanism, leads to the consideration of the new kind of solution called hybrid mechanism.

Table 3.1: HYDROïD chest and pelvis limbs approximated with simple primitives and their dimensions and masses

Limb	Primitive	mass	dimensions (*mm*)
Chest	Parallelepiped	$8,49$	$149 \times 165 \times 298$
Pelvis	Parallelepiped	$8,24$	$160 \times 189 \times 290$

On basis of the above short analysis, the following statement can be made: the motion of the first 3-DoF torso mechanism can be considered as a particular solution of a generic hybrid mechanism. It can be used for the 3 DOF shoulder and hip mechanism. Given the definition of the hybrid mechanism, the kinematic synthesis has to solve two questions: first, will the serial or fully parallel subpart be attached to the base of the mechanism (i.e. the chest or the pelvis)? And, second, which motion will the serial (i.e. rotary joint) part achieve? The answer to the first question will determine the moving part of the whole mechanism. At first glance, the answer will tend to favor the fully parallel mechanism to be fixed to the base since two actuators are required. However,

it may be interesting to compare the size of the two actuators to that of the serial rotary joint. The answer to the second equation is of great importance since, depending on the choice, it will determine the size of the fully parallel mechanism branches. Indeed, choosing, for example, a movement other than the pitch, which is the largest one for the torso mechanism, will inherently increase the size of the parallel subpart. This will challenge the constraints induced by the Hanavan model in terms of mechanism compactness. Additionally, given the definition of the hybrid mechanism, although the term "hybrid" has not been explicitly introduced, the solutions developed by Ouezdou et al. [71] and by Byung et al. [72] can be considered as hybrid mechanisms. Table 3.2 compares the several known hybrid solutions. The comparison tackles the answers to the above two questions. The range of motion remains the most important issue since it may limit the use of this kind of solution in humanoid robotics field. It is worthy to note that the three compared solutions suffer from this limitation to the fulfillment of the each mechanism requirements.

Table 3.2: Comparison between three existing hybrid solutions dedicated to hip mechanism

Solution	First Chain	Serial Motion	Range of motion (°) of the parallel part
Ouezdou et al.	Parallel	Pitch	Yaw : $-20, +20$ Roll : $-20, +20$
Byuon et al.	Serial	Yaw	Pitch : $-50, +50$ Roll : $-25, +25$
Alfayad et al.	Serial	Pitch	Yaw : $-10, +10$ Roll : $-12, +12$

Moreover, the arrangement of the links and the 15 joints of the two first compared solutions makes both of them hard to fit with the compactness requirements while trying to reach the range of motion needed for manipulation and interaction tasks. As a result, choosing the serial part for the pitch movement is most appropriate. Indeed, the second compared solution (i.e. yaw produced serially) will require a very large stroke for the linear actuators to reach the almost range of motion. The last consideration concerns the position of the actuators. It is worthy to note that the first solution takes advantage of the possibility of setting the three actuators on the pelvis. However, this advantage has

to be compared to the benefit reached by using a moving linear actuator with spherical joints as stated by Alfayad et al. [73]. Furthermore, the workspace of the proposed solution has to be free from any singular position, which is not clearly established for the first compared solution. Finally, whereas the last solution in the comparison is the most compact and the most promising, it has to be improved to significantly increase the range of all motions.

3.2 Proposed Hybrid Structure

3.2.1 Kinematic Description

The hybrid solution proposed for the first 3 DOF of the torso mechanism of the HYDROïD humanoid robot is depicted in Figure 3.4. This generic solution is a generalization of the hip mechanism proposed by Alfayad et al. [73], as will be shown later. It consists of a 3-DoF mechanism that has 17 joints arranged in three kinematic chains leading to two independent closed loops.

Classically a rod-crank system has been used to transform linear piston motion to rotary motion. This system suffers from a negative point related to singularity aspect. A rod-crank system (R-C1) is presented in Figure 3.1(a), when the three points I, J, O are aligned; the system is locked in singularity position and it is impossible to make it moving by its own force as shown Figure 3.1(b). To overcome this problem, one can imagine two rod-crank systems sharing the same output point O. If the coordinates of the two points I' and J' defining the second rod-crank system (R-C2) are well chosen (see Figure 3.1(c)), then, when the first (R-C1) system is in singularity position, the (R-C2) will not be in singularity position (see Figure 3.1(d)). In this case, each time a rod-rank system is locked the second one will produce the needed rotation around the O point. As a result, a large motion range is produced at the output using two linear actuators in the input.

As we need to produce two perpendicular rotations at the output. At first glance, one can suggest that four rod-crank systems can be used to produce two perpendicular rotations at the output. As shown in Figure 3.2, by arranging two rod-crank systems

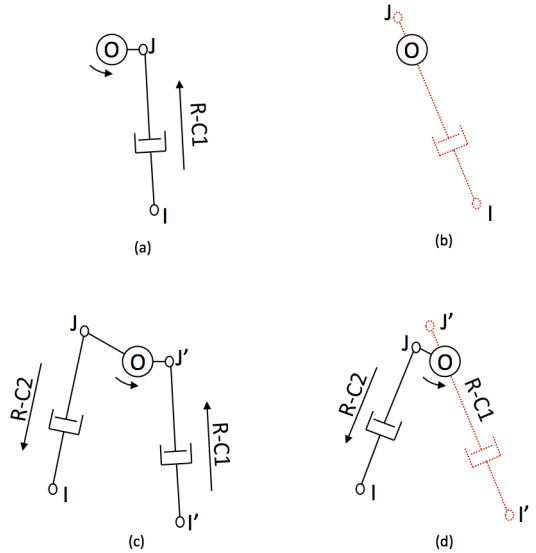

Figure 3.1: Rod-Crank systems

$[I_1J_]$) & $[I_1^{'}J_1^{'}]$ in the XZ plane, rotation around Y axis is guaranteed, while the two other rod-crank systems $[I_2J_2]$ & $[I_2^{'}J_2^{'}]$ situated in the XY plane will ensure the rotation around the Z axis.

However, using over-actuation philosophy to build humanoid robot is unfeasible in our project since available space and cost are the main constraints.

Therefore, to avoid the over-actuation disadvantage, two linear actuators $[DF]$ & $[EG]$ situated in 3D space have been used in the input to produce the two rotary motions at the output. As shown in Figure 3.3, the projections of these two linear actuators in the XY & XZ planes are equivalent to the four rod-rank systems. The next sections will determine the optimal points in the space to attach the two linear actuators. The objective is to maximize the produced torque and to minimize the extending and retracting lengths of the actuators.

As shown in Figure 3.4, two actuated linear actuators have to cooperate in order to generate the yaw and roll movements. In case of the torso and hip mechanism, the fully parallel subpart of the 3-DoF mechanism is located below the serial part. The combination of the movements of the linear actuators allows generation of roll and yaw

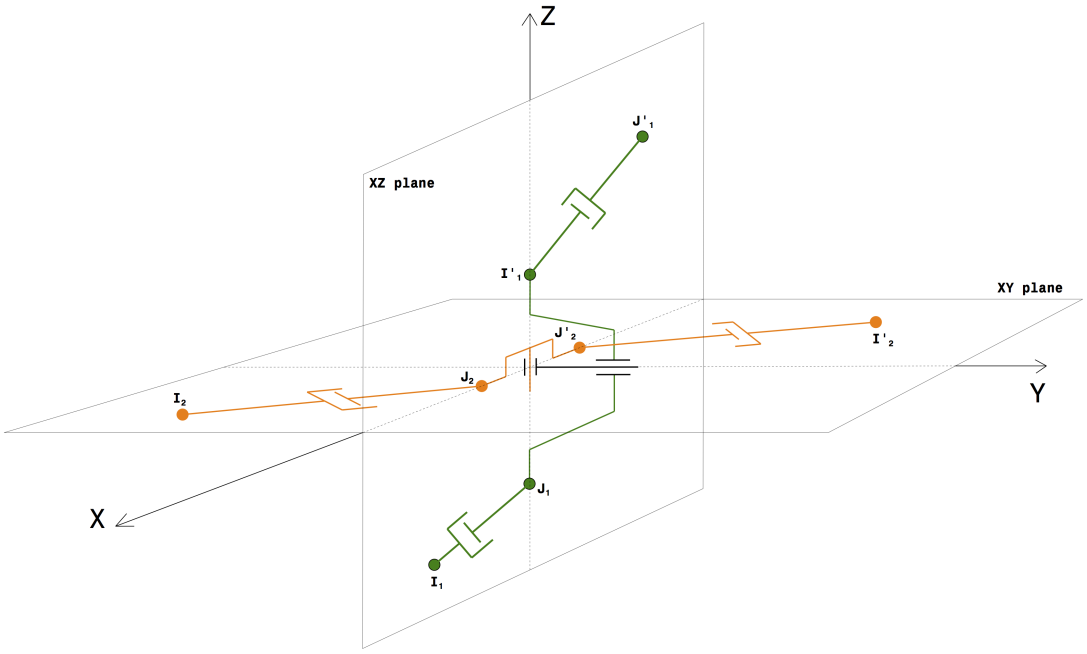

Figure 3.2: Rod-Crank system with 2 outputs

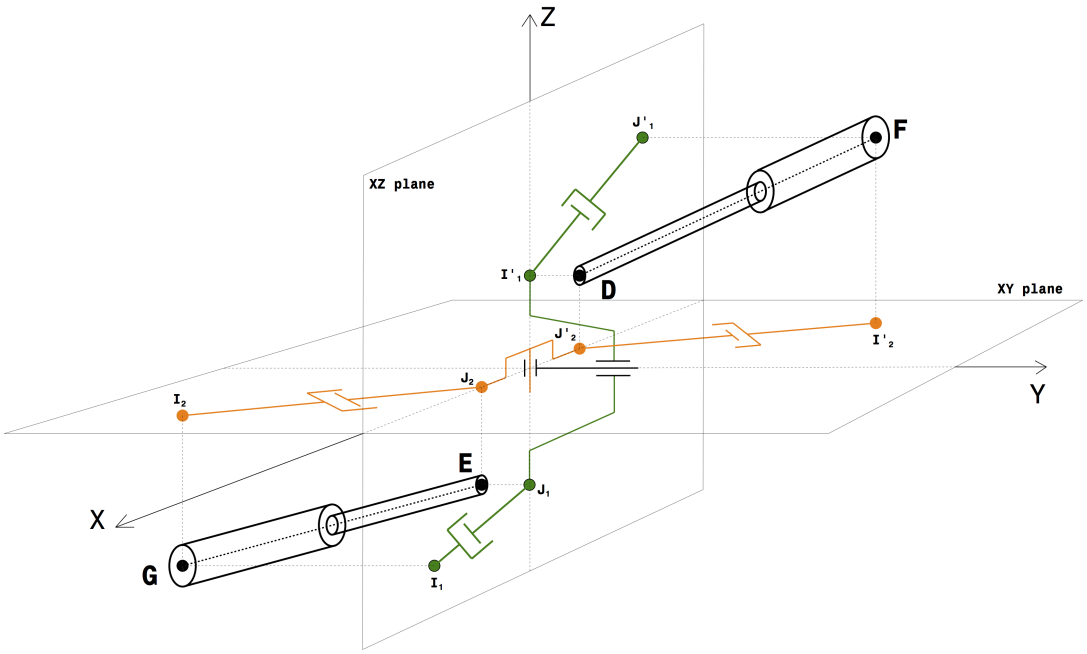

Figure 3.3: Proposed solution. Two linear actuators were used to produce the rotations at the output. Pistons in the XY and XZ planes are the projections of the linear actuators

motions of the generic hybrid mechanism. As depicted in Figure 3.4, six particular points (A, B, D, E, F and G) corresponding to the spherical and universal joints fix the relative position of the two linear actuators. It is easy to see that the arrangement

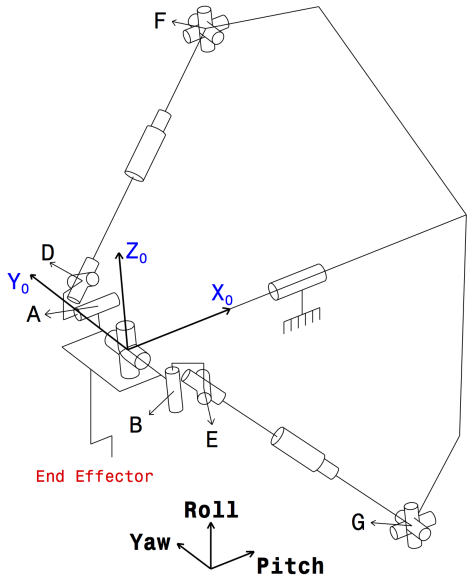

Figure 3.4: New generic hybrid mechanism

of the linear actuators, namely the relative position of the abovementioned six points, influences the movement amplitudes. In the case of the 3 DOF lumbar part of the torso and hip mechanism, these two linear actuators are structurally built to be in two parallel planes, one side and the other front plane containing the axis of the pitch rotation. This can be reached by positioning points F and G at equal distance from the pitch rotation axis while satisfying the following conditions for points A, B, D and E (see Figure 3.5):

$$A \equiv D \;\&\; B \equiv E$$

The chosen arrangement of the two linear actuators was dictated by the amplitude of motion needed for the roll and yaw. The roll motion has a larger amplitude than the yaw one, which leads to the following choice: the linear actuators have to move in the same direction for the yaw motion and in the opposite one for the roll movement; otherwise, their stroke has to be significantly increased. To tackle this issue for the shoulder mechanism, a new arrangement of the two linear actuators has been identified

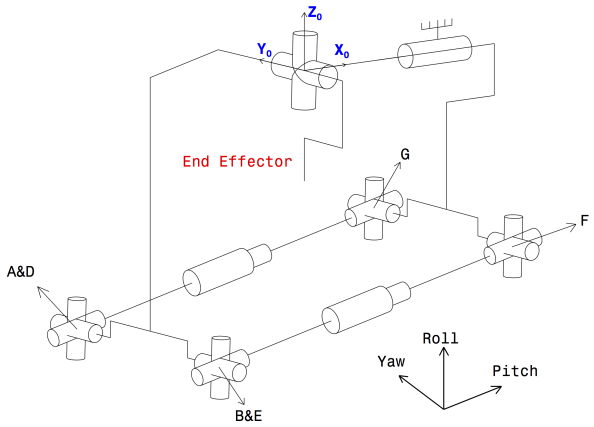

Figure 3.5: Hip hybrid mechanism

where the attachment points of each linear actuator left the previous planes and are now positioned in 3D space as depicted in Figure 3.4. In the proposed solution, the two chains of the fully-parallel subpart are now positioned on either side of the central chain with two spherical joints at each tip of the linear actuators. This arrangement allows the linear actuators to assist each other when one of them reaches its stroke limit, and thus, significantly enlarges the range of motion for both yaw and roll, as will be demonstrated later.

Figure 3.6 presents the proposed hybrid solution for the Four DOF of freedom Torso. The first 3 DOF have been concluded from the analysis presented below in this chapter. A new adding DOF at the thoracic level of the human spine has been added to fulfill the advantages obtained in Chapter 2.

3.2.2 Parameter Description

The parameter description based on the Khalil et al. notation [74] of the new solution is given in Table 3.3, Where the main parameters are defined as follow: α_j is the angle between Z_{j-1} and Z_j with respect to the rotation around X_{j-1}, d_j is the distance between Z_{j-1} and Z_j along X_{j-1}, θ_j is the angle between X_{j-1} and X_j with respect to the rotation around Z_j, r_j is the distance between X_{j-1} and X_j along Z_j. All limbs and all joint axes of the fully-parallel chains are respectively noted ${}^{j}C_i$ and $\mathbf{Z_j^i}$ with $j = 1,2$ indicating

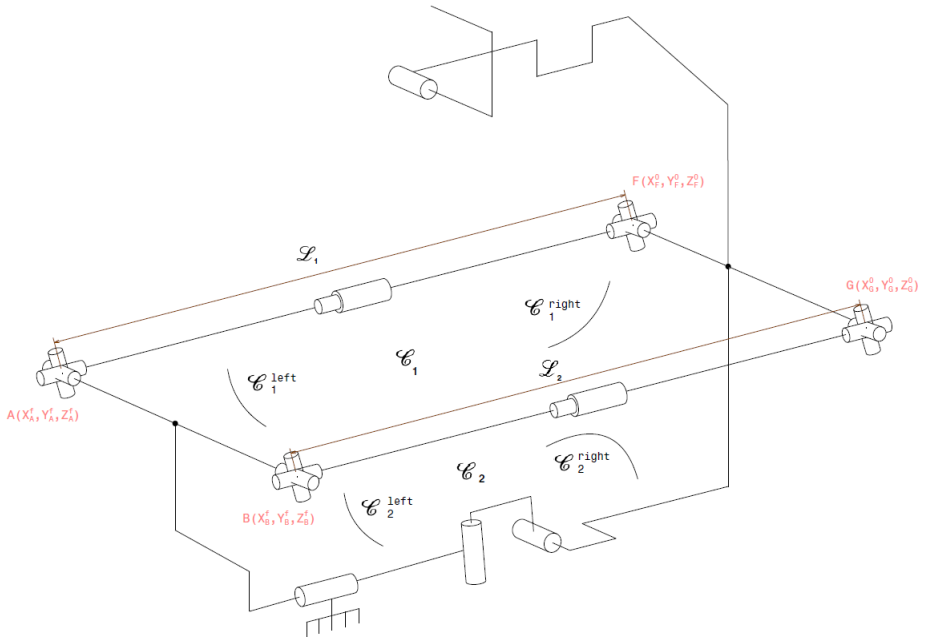

Figure 3.6: Torso hybrid mechanism

the kinematic chain index the frame belongs to and $1 \leq i \leq 9$ as given in Figure 3.7, where $(A,\ B,\ D,\ E,\ F\ \&\ G)$ are the centers of the links $(C_3^1,\ C_3^2,\ C_4^1,\ C_4^2,\ C_6^1\ \&\ C_6^2)$ respectively. The relative coordinates for these centers with respect to the previous link are defined as $A(X_A^f,\ Y_A^f,\ Z_A^f)$, $B(X_B^f,\ Y_B^f,\ Z_B^f)$, $D(X_D^{3,1},\ 0,\ Z_D^{3,1})$, $E(X_E^{3,2},\ 0,\ Z_E^{3,2})$, $F(X_F^0,\ Y_F^0,\ Z_F^0)$ and $G(X_G^0,\ Y_G^0,\ Z_G^0)$ respectively.

Since the new hybrid mechanism is generic, some parameters have to be set to particular values (see Figure 3.7 for the definition of these parameters),in order to get the complete description of the hybrid Torso and Hip solutions. These conditions can be summarized in the following set of equations:

$$X_A^f = X_B^f,\ Y_A^f = -Y_B^f,\ Z_A^f = Z_B^f$$

$$X_D^{3,1} = Z_D^{3,1} = X_E^{3,2} = Z_E^{3,2} = 0$$

$$X_F^0 = X_G^0,\ Y_F^0 = -Y_G^0,\ Z_F^0 = Z_G^0$$

Once the novel kinematic structure has been proposed, carrying out its performance analysis is required. This analysis will be based on geometrical models that are detailed

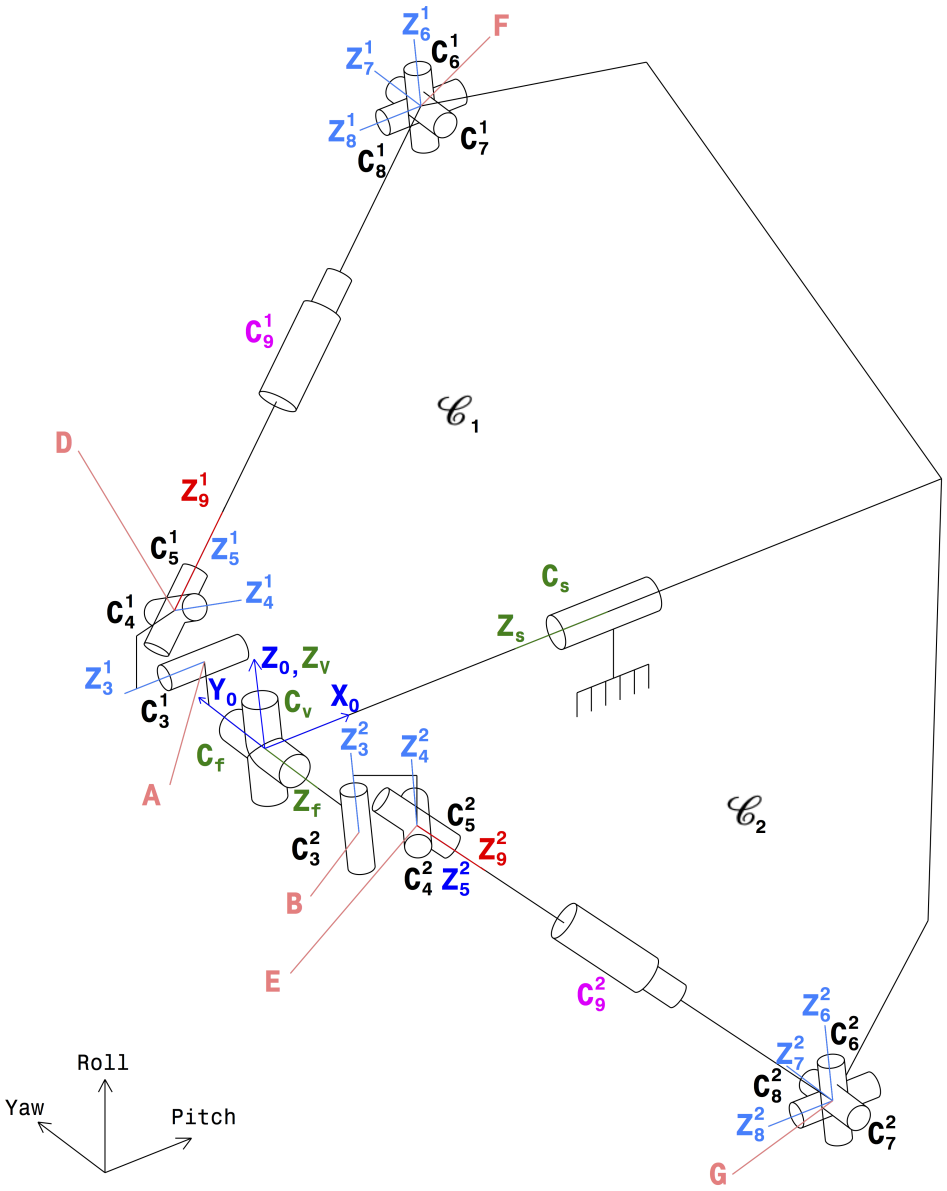

Figure 3.7: New generic hybrid mechanism with all joint axis and notations

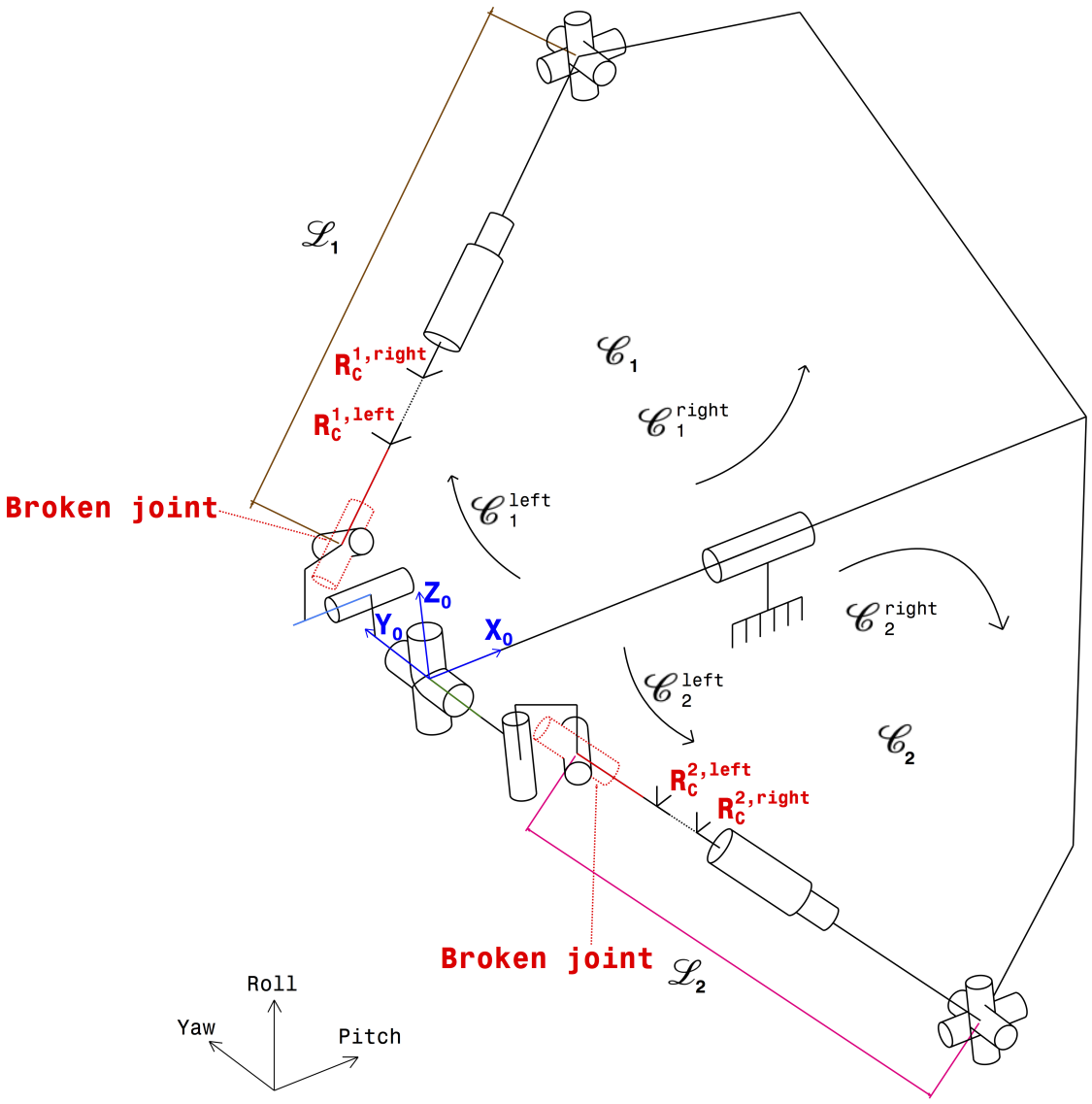

Figure 3.8: Closed loops and broken joints

Table 3.3: Khalil et al. parameters for the generic hybrid mechanism

j	i	σ_j	γ_j	b_j	α_j	d_j	θ_j	r_j
C_v	C_0	0	0	0	0	0	θ_v	0
C_f	C_v	0	0	0	$\frac{\pi}{2}$	0	$-\theta_f - \frac{\pi}{2}$	0
C_3^1	C_f	0	0	0	$\frac{\pi}{2}$	X_A^f	$\theta_3^1 - \theta_3^{1,0}$	$-Y_A^f$
C_4^1	C_3^1	0	0	0	$\frac{\pi}{2}$	$X_D^{3,1}$	$\theta_4^1 + \theta_4^{1,0}$	0
C_5^1	C_4^1	0	0	0	$\frac{\pi}{2}$	0	θ_5^1	0
$R_C^{1,left}$	C_5^1	0	0	0	0	0	0	0
C_6^1	C_0	0	0	0	0	X_F^0	$\theta_6^1 + \pi$	$-Y_F^0$
C_7^1	C_6^1	0	0	0	$\frac{\pi}{2}$	0	$\theta_7^1 + \frac{PI}{2}$	0
C_8^1	C_7^1	0	0	0	$\frac{\pi}{2}$	0	$\theta_8^1 - \theta_8^{1,0}$	0
C_9^1	C_8^1	1	0	0	α_9^1	0	0	$-R_1$
$R_C^{1,right}$	C_9^1	0	0	0	0	0	$-\frac{\pi}{2}$	0
C_3^2	C_f	0	$-\frac{\pi}{2}$	0	$\frac{\pi}{2}$	X_B^f	$\theta_3^2 - \theta_3^{2,0}$	$-Y_B^f$
C_4^2	C_3^2	0	0	0	$\frac{\pi}{2}$	$X_E^{3,2}$	$\theta_4^2 + \theta_4^{2,0}$	0
C_5^2	C_4^2	0	0	0	$\frac{\pi}{2}$	0	θ_5^2	0
$R_C^{2,left}$	C_5^2	0	0	0	0	0	0	0
C_6^2	C_0	0	0	0	0	X_G^0	$\theta_6^2 + \pi$	$-Y_G^0$
C_7^2	C_6^2	0	0	0	$\frac{\pi}{2}$	0	$\theta_7^2 + \frac{\pi}{2}$	0
C_8^2	C_7^2	0	0	0	$\frac{\pi}{2}$	0	$\theta_8^2 + \theta_8^{2,0}$	0
C_9^2	C_8^2	1	0	0	$-\alpha_9^2$	0	0	$-R_2$
$R_C^{2,right}$	C_9^2	0	0	0	0	0	$-\theta_C^2$	0

in the next section.

3.3 Modeling & Kinematic Analysis

In order to carry out the kinematic analysis with the help of a simulation tool, two models have to be established. These models concern, first, the Inverse Geometrical Model IGM used to calculate the linear actuator lengths ($\mathscr{L}_j, \quad j = 1,2$) for a given posture of the chest, arm or the leg whenever the torso, shoulder or the hip mechanism is considered. The other model concerns the kinematic performance will be presented in the second part of this work.

3.3.1 Inverse Geometrical Model - IGM

As mentioned above, there are two kinematic closed loops named $\mathscr{C}_j$, depicted in Fig. 3.7. Each of them is composed of the links ${}^jC_i$ as follows: (C_s, C_v, C_f, C_1^j, C_2^j, C_3^j, C_4^j, C_5^j, C_6^j, C_7^j, C_8^j, C_9^j) with $1 \leq j \leq 2$. The spherical joints that link the linear actuator to the base platform of the fully parallel subpart are split on three independent orthogonal axes (See Fig. 3.7). The connection of the linear actuator to the moving platform of the

fully parallel subpart consists of a universal joint and a rotational one; the former allows the rotational movement of the linear actuator around its own axis and is chosen to be the "broken" joint to establish the IGM of the fully parallel subpart as shown in Figure 3.8. The technique of breaking the kinematic closed loops to identify the equivalent kinematic open loop has been used to get the desired IGM. This choice was justified by the need to split the kinematic closed loops into two equivalent halves whenever the number of joints is considered. The upper script $Left$ and $Right$ are added to each closed $\mathscr{C}_j$ to identify the left and the right parts, respectively.

To generalize our model, we take into consideration the fact that the center of the links C_j^i (with $i \in \{1,2\}$ and $j \in \{3,4,6\}$) is variable.

The inputs parameters of the hybrid mechanism are the linear actuator lengths $\mathscr{L}_j$. The outputs are grouped in a three-dimension vector named $\mathbf{q_a} = (q_s, q_v, q_f)^t$ (sagittal, vertical and frontal angle respectively). All other i^{th} passive joints of the two closed loops are named θ_i^j where j is the closed loop index. Table 3.3 gives the required parameters for the description of the two branches of the two closed loop.

To establish the IGM model of the mechanism, the pitch rotation is straight forward since it belongs to the serial part. However, getting the roll and yaw rotations (parallel part) requires eliminating all passive joints angle θ_i^j in the geometrical constraints of closing the kinematic loops $\mathscr{C}_j$.

Hence, the base of the fully parallel mechanism can be considered, without any loss of generalization, to be fixed to link C_1. The target is to establish the relations giving the lengths of actuators function of the elements of vector $\mathbf{q_a}$. Since the closed loops $\mathscr{C}_j$ were broken at the joint $\mathbf{Z}_5^j$ of each, two sub-branches have to be considered. The first one, named left branch, connects links C_4^j to C_v, and the other, named right branch, links the limbs going from C_v^j to C_9^j. The homogenous transformation matrix between the two frames R_0 attached to link C_v and R_5 fixed on C_5^j can be expressed in the two circuits, using either the right or the left sub-branch. The closure loop relation yields the obvious equation between both homogenous matrices ${}^1\mathbf{T}_5^{Right,j}$ and ${}^1\mathbf{T}_5^{Left,j}$:

$$ {}^1\mathbf{T}_5^{Right,j} = {}^1\mathbf{T}_5^{Left,j} \quad 1 \leq j \leq 2 \tag{3.1}$$

The expressions of the elements of the above matrices are arrived at by multiplying

all successive homogenous transformation matrices and using the following notations: $S_k^j = \sin(\theta_k^j)$ and $C_k^j = \cos(\theta_k^j)$. The same notations are used for the sine and cosine functions of α_1, α_2, γ_2 (see table 5 for the definition) and for the vector $\mathbf{q_a}$ elements. To exemplify, the first loop $\mathscr{C}_1$ closing relation (Eq. 3.1) is detailed below. Using the equivalence between the third and fourth columns of each matrix, we obtain the following relations:

$$(C_3^i)^2 a_{1,k}^i + S_3^i C_3^i a_{2,k}^i + C_3^i a_{3,k}^i + S_3^i a_{4,k}^i + a_{5,k}^i = 0 \tag{3.2}$$

The way to obtain the above equations (3.2) and the expression of $a_{j,k}^i$ are detailed in the Appendix for $i \in \{1,2\}$, $j \in \{1,2,3,4,5\}$ and $k \in \{1,2,3\}$
The equation(3.2)for k=2 gives:

$$S_3^i = -\frac{(C_3^i)^2 b_1^i + C_3^i b_3^i + b_5^i}{C_3^i b_2^i + b_4^i} \tag{3.3}$$

by replacing equation (3.3) with equation (3.2) for k=1 and k=3, we obtain:

$$(C_3^i)^3 b_{1,n}^i + (C_3^i)^2 b_{2,n}^i + C_3^i b_{3,n}^i + b_{4,n}^i = 0 \tag{3.4}$$

with

$$b_{1,n}^i = a_{1,k}^i a_{2,2}^i - a_{2,k}^i a_{1,2}^i \tag{3.5}$$

$$b_{2,n}^i = a_{1,k}^i a_{4,2}^i - a_{2,k}^i a_{3,2}^i + a_{3,k}^i a_{2,2}^i - a_{4,k}^i a_{1,2}^i \tag{3.6}$$

$$b_{3,n}^i = -a_{2,k}^i a_{5,2}^i + a_{3,k}^i a_{4,2}^i - a_{4,k}^i a_{3,2}^i + a_{5,k}^i a_{2,2}^i \tag{3.7}$$

$$b_{4,n}^i = -a_{4,k}^i a_{5,2}^i + a_{5,k}^i a_{4,2}^i \tag{3.8}$$

with $n \in \{1,2\}$

Combining equation (3.4) for $n = 1$ and equation (3.4) for $n = 2$, we obtain a second order polynomial equation in C_3^i

$$L_1^i (C_3^i)^2 + L_2^i C_3^i + L_3^i = 0 \tag{3.9}$$

with

$$L_1^i = b_{1,1}^i b_{1,2}^i - b_{1,2}^i b_{2,1}^i \tag{3.10}$$

$$L_2^i = b_{1,1}^i b_{3,2}^i - b_{1,2}^i b_{3,1}^i \tag{3.11}$$

$$L_3^i = b_{1,1}^i b_{4,2}^i - b_{1,2}^i b_{4,1}^i \tag{3.12}$$

Solving equation (3.9) when even $\delta = (L_2^i)^2 - 4L_1^i L_3^i >= 0$, we obtain:

$$\theta_3^i = \pm \arccos\left(\frac{-L_2^i \pm \sqrt{\delta}}{2L_1^i}\right) \tag{3.13}$$

if $\delta < 0$ no solution for θ_3^i and the chains cannot be closed. Meanwhile, equation (3.13) shows 4 analytic solutions $\theta_{3,j}^i$ for θ_3^i with $i \in \{1,2\}$ and $j \in \{1,2,3,4\}$. To choose the right solution $\theta_{3,sol}^i$, we adopted the following design criteria. To prevent the overloading on the link and the interference between the parts, the link C_3^i's rotation should be limited. This yields the following rotation:

$$\theta_{3,min}^i < \theta_{3,sol}^i < \theta_{3,max}^i$$

On the other hand, as $\theta_{3,sol}^i$ is obtained numerically using the error criteria, it should satisfy equations (3.2). Hence, a numerical error $Err(\theta_{3,sol}^i)$ can be established as the sum of the errors induced by each equation: $Err(\theta_{3,i}^1) = \sum_{r=1}^{3} Err_{i,r}^2$.

$Err_{i,r} = (C_{3,i}^1)^2 a_{1,r}^i + S_{3,i}^1 C_{3,i}^1 a_{2,r}^i + C_{3,i}^1 a_{3,r}^i + S_{3,i}^1 a_{4,r}^i + a_{5,r}^i$
The used condition for the choice of the appropriate $\theta_{3,sol}^i$ solution can be stated as: $Err(\theta_{3,sol}^i) < \varepsilon, \quad i \in \{1,2\}$. From the forth column of the first member of the closure loop relation for chain 1, and using the value $\theta_{3,sol}^1$, the following can be established:

$$X_D^0 = (-C_v S_f C_{3,sol}^1 + S_v S_{3,sol}^1) X_D^{3,1} - C_v C_f Z_D^{3,1} - C_v S_f X_A^f + C_v C_f Y_A^f + S_v Z_A^f \tag{3.14}$$

$$Y_D^0 = (-S_v S_f C_{3,sol}^1 - C_v S_{3,sol}^1) X_D^{3,1} - S_v C_f Z_D^{3,1} - S_v S_f X_A^f + S_v C_f Y_A^f - C_v Z_A^f \tag{3.15}$$

$$Z_D^0 = -C_f C_{3,sol}^1 X_D^{3,1} + S_f Z_D^{3,1} - C_f X_A^f - S_f Y_A^f \tag{3.16}$$

Since the center F is fixed, we have the length of the piston of Chain 1:

$$\mathscr{L}_1 = \sqrt{(X_D^0 - X_F^0)^2 + (Y_D^0 - Y_F^0)^2 + (Z_D^0 - Z_F^0)^2} \tag{3.17}$$

The same calculation for chain 2 leads to the following conditions of point E coordinates:

$$X_E^0 = (-C_v C_f C_{3,sol}^2 + S_v S_{3,sol}^1) X_E^{3,2} + C_v S_f Z_E^{3,2} - C_v S_f X_B^f + C_v C_f Y_B^f + S_v Z_B^f \quad (3.18)$$

$$Y_E^0 = (-S_v C_f C_{3,sol}^2 - C_v S_{3,sol}^2) X_E^{3,2} + S_v S_f Z_E^{3,2} - S_v S_f X_B^f + S_v C_f Y_B^f - C_v Z_B^f \quad (3.19)$$

$$Z_E^0 = S_f C_{3,sol}^2 X_E^{3,2} + C_f Z_E^{3,2} - C_f X_B^f - S_f Y_B^f \quad (3.20)$$

Since the center G is fixed, we have the length of the piston of Chain 2:

$$\mathscr{L}_2 = \sqrt{(X_E^0 - X_G^0)^2 + (Y_E^0 - Y_G^0)^2 + (Z_E^0 - Z_G^0)^2} \quad (3.21)$$

In case of torso or hip mechanism, the center of the links C_4^i is coincident with the center of the links C_3^i. Therefore, the following relations can be written:

$$X_D^{3,1} = X_E^{3,1} = Z_D^{3,1} = Z_E^{3,1} = 0$$

Hence, the new expression of centers D and E coordinates is given in the following set of equations:

$$X_D^0 = X_A^0 = -C_v S_f X_A^f + C_v C_f Y_A^f + S_v Z_A^f \quad (3.22)$$

$$Y_D^0 = Y_A^0 = -S_v S_f X_A^f + S_v C_f Y_A^f - C_v Z_A^f \quad (3.23)$$

$$Z_D^0 = Z_A^0 = -C_f X_A^f - S_f Y_A^f \quad (3.24)$$

$$X_E^0 = X_B^0 = -C_v S_f X_B^f + C_v C_f Y_B^f + S_v Z_B^f \quad (3.25)$$

$$Y_E^0 = Y_B^0 = -S_v S_f X_B^f + S_v C_f Y_B^f - C_v Z_B^f \quad (3.26)$$

$$Z_E^0 = Z_B^0 = -C_f X_B^f - S_f Y_B^f \quad (3.27)$$

To get the IGM of the torso or the hip mechanism, the previous values of centers D and F coordinates have to be used in equations (3.17) and (3.21). Once the IGM model is established, we present in the next results section how it is used to optimize the proposed

solution for the torso, hip and shoulder mechanisms.

3.4 Torso, Hip and Shoulder Optimized Solutions

In the early stage of designing a robotic system, it is required to determine the appropriate parameters defining the relative arrangement of the joints. This step induces the whole dimensions of the limbs. Thanks to the established IGM, an optimization process was carried out to get the optimal positions of the attachment points of the two linear actuators of the fully-parallel subpart. The chosen criterion to be optimized is the torques on yaw and roll axes produced by the mechanisms for given linear actuators forces. Each torque is called a quasi-static torque since it is based on the geometrical effects of the lever arm between each linear actuator and the axis of rotation. This is the first step in pre-dimensioning the proposed mechanism that has to be extended to kinetostatic and dynamic analysis in order to manage an external effort applied on the arm or on the thigh. As shown on figure 3.9, the torque to be optimized varied non-linearly with the vertical and frontal angles due to the non-linearity evolution of the abovementioned lever arm. Moreover, this torque depends on other parameters such as the linear force of the linear actuator and the initial position of the attachment points of the linear actuator, namely points A, B, G and F (see figure 3.7). Therefore, this torque can be written as the following function:

$$\tau_{axis} = f(F_1, F_2, \psi_1, \psi_2, \psi_3, \psi_4)$$

where: F_1 and F_2 are the forces exerted by the linear actuators. $\psi_1 = (X_A, Y_A, Z_A)$ and $\psi_2 = (X_B, Y_B, Z_B)$ are vectors grouping respectively the centers A and B coordinates while $\psi_3 = (X_G, Y_G, Z_G)$ and $\psi_4 = (X_F, Y_F, Z_F)$ are those, respectively, of the centers G and F. As we consider the yaw and roll axes, two quasi-static torques namely τ_y and τ_z are defined. For each of them, two values denoted positive $(+)$ and negative $(-)$ quasi-static torque are introduced. The positive or negative definition is related the direction of the torque around the considered axis. Hence, four discrete torques τ_y^+, τ_y^-, τ_z^+ and τ_z^- are defined.

On the other hand, for the same angular displacement, the retracting (l_1^j) and extend-

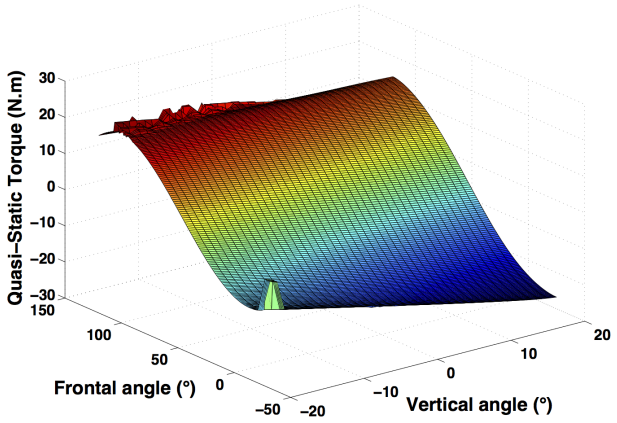

Figure 3.9: Quasi-static torque τ_y^+ function of the end-effector yaw and roll angles

ing (l_2^j) lengths of the j^{th} ($j = 1,2$) linear actuators (see figure 3.10) depend directly on the position of the attachment of the linear actuators $(\psi_1, \psi_2, \psi_3, \psi_4)$. Producing an angular displacement of the end effector for its total range with minimizing l_1^j and l_2^j will reduce the whole size of the mechanism. This aspect is treated as a penalty constraint in the optimization process.

Therefore, the optimization process is carried out to find the optimal positions for the centers A, B, G and F such that the output torque to geometrical dimensions ratio is optimal in the obtained kinematic structure.
To carry out the optimization process, we considered that these centers are varying into a sphere of radius r. The radius of these spheres is chosen with respect to the global available space of the concerned mechanism. Figure 3.11 shows the variation sphere of the corresponding four centers; consequently, two different configurations are depicted.

The optimization process will take in consideration the following aims:

- Maximize τ_y^+, $|\tau_y^-|$, τ_z^+, and $|\tau_z^-|$
- Minimize l_1 and l_2 with considering that $l_1 > L_c$ and $l_2 < l_c + l_p$ (see figure 3.10 for the definition of l_p and l_c)

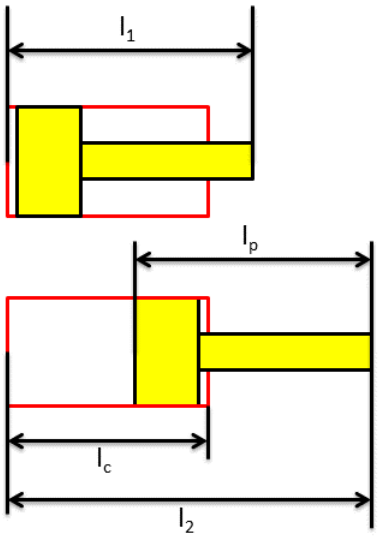

Figure 3.10: Retracting and Extending linear actuator configurations

Hence, the established IGM model can be used in the optimization tool to determine, at each iteration, the lengths $\mathscr{L}_1$ and $\mathscr{L}_2$ of the linear actuator. of the linear actuator. The adopted optimization procedure is described as follows. For each combination, we calculated the variation of the maximum positive and negative quasi-static torques around the Y-axis and Z-axis. Also the variation of the retracting and extending lengths of the actuators was developed. The calculation was done for a constant linear actuators force equivalent to 1900 N which corresponds to pressure of 50 bar.

The obtained results are given in the following figures. As seen in figure 3.12a, the variation of the initial position of the centers has a significant impact on the maximum positive torque around Z-axis τ_z^+. The rate of variation in this case is almost 66%. In contrast, there is significant effect on the maximum positive torque around Y-axis τ_y^+. On the other hand, the extending lengths of linear actuator 1 and 2 shown in figure 3.12c and figure 3.12d are clearly affected by the centers position variation. These lengths take their low values for almost the same zone of the centers where we have the high maximum torques τ_y^+ and τ_z^+. The rate of variation of the extending lengths is up to 42% and 36% respectively. Moreover, the rate of variation of the retracting lengths of

linear actuator 1 and 2 given in figure 3.12e and figure 3.12f takes high values, going up to 50% and 62.5% respectively.

From this study, we primarily improve the selection of positions for the centers A, B, F and G in order get the largest amount of quasi-static torque for the smallest extending and retracting linear actuators values. Therefore, we can state that these results lead to an optimal solution: the quasi-static torques are maximized with lesser energy expense since minimizing the piston stroke will result in a minimum flow. For the final results, the following table presents the selected positions for Torso, hip and shoulder mechanisms. The coordinates are given in *mm* with respect to the center of the reference frame shown in Figure 3.11.

Table 3.4: The selected positions for the attachment linear actuators centers

Center	Torso	Shoulder	Hip
A	$(-64, 38, -86)$	$(-11, 0, -24)$	$(-64, 38, -86)$
D	$(-64, -38, -86)$	$(14, 9, 22)$	$(-64, -38, -86)$
F	$(61, 36, -60)$	$(95, 70, 95)$	$(61, 36, -60)$
G	$(61, -36, -60)$	$(95, -70, -95)$	$(61, -36, -60)$

3.5 Conclusion

In this chapter, a new generic hybrid mechanism based on serial and fully parallel subparts was proposed. We show that by positioning the two tips of the linear actuators of the fully parallel subpart, a Torso, shoulder and hip mechanism for humanoid robots can be designed. The proposed solution, which is a generalization of the previous hybrid solution introduced by the authors, consequently improves the angular range of motion of the output, making its application for a all the three mechanism possible. The IGM model for the generic solution was established and its adaptation to the particular case of the torso and hip was identified. An optimized solution for the mechanisms was given. The optimization process was based on two criteria: maximum output quasi-static torque for yaw and roll axes and minimum stroke for the linear actuators for a maximum range of angular motion.

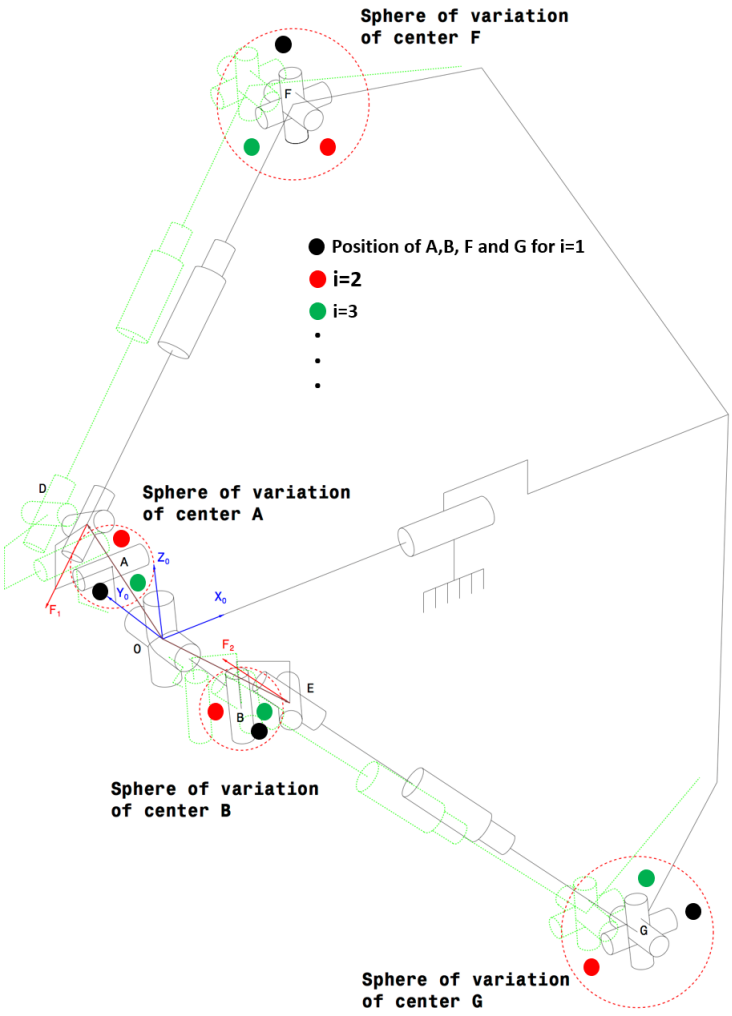

Figure 3.11: Variation spheres for the linear actuators attachement centers and two different configurations

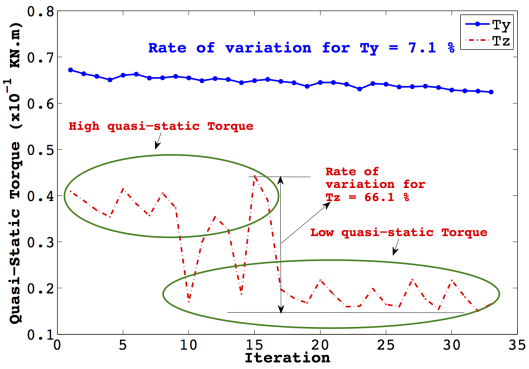

(a) Variation of the maximum positive Torque around Y-axis and Z-axis

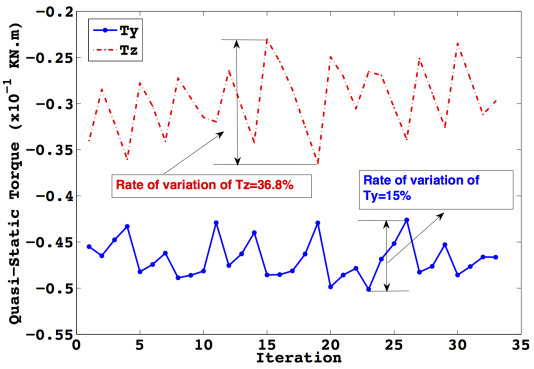

(b) Variation of the maximum negative Torque around Y-axis and Z-axis

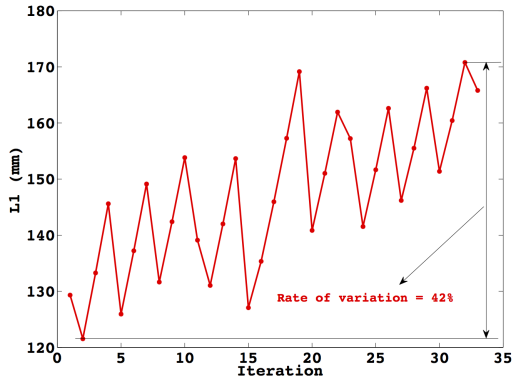

(c) Variation of the extending length for linear actuator 1 with different initial centers position

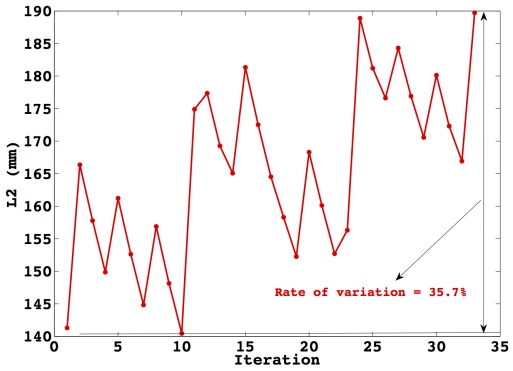

(d) Variation of the extending length for linear actuator 2 with different initial centers position

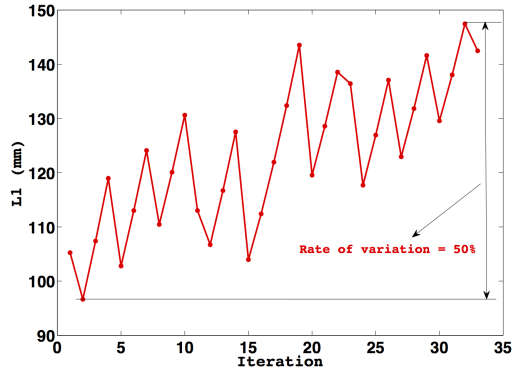

(e) Variation of the retracting length for linear actuator 1 with different initial centers position

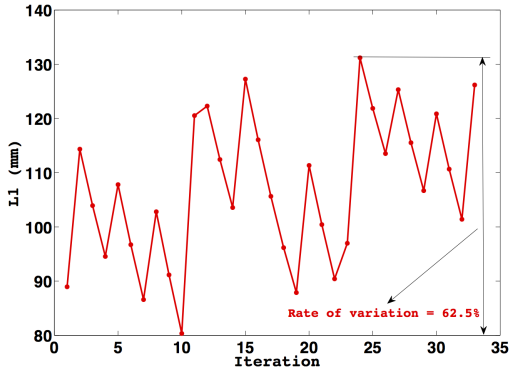

(f) Variation of the retracting length for linear actuator 2 with different initial centers position

Figure 3.12: Optimization result

Chapter 4

HYDROïD arm improvement

Contents

As mentioned previously in the introduction, the kinematic movement of the end effector of the robot is also affected by the configuration of the joints and the kinematics of the robot arm. Therefore, this topic has gained considerable attention from roboticists because of its great importance. A good configuration allows the robot arm to be able to perform dexterity tasks with a wide range of movements and obviously promise safer, more efficient work environments for people. In addition, this will contribute to stability during robot locomotion [75] as well as to the dynamic behavior of the whole robot.

Many humanoid robot arms have been developed till now, but as far as we know, no existing arm relies entirely on the human arm structure. They ignored some joints that have an effective and significant role on the whole robot performance. One of this joint is the shoulder girdle which is the inner part of the shoulder complex. In the following, we will present a macroscopic anatomy for the human arm with more concentration on the part of the shoulder complex. Then, we present some existing model for the shoulder girdle which it lead us to derive the optimized model for arm of our HYDROïD robot.

4.1 Range of Motion of Human Arm

Human arm acquired a considerable attention from the roboticists due to its important role. It assist to the stability during walking through whole body dynamics [76], [77], and obviously, it will carry and move more or less heavy objects with the accuracy required by the targeted applications. Therefore, the design of humanoid robot arm able to perform dexterity tasks with wide range of motion is still an open challenge.

The human arm is constituted by a series of joints forming a system characterized by a high level of complexity and dexterity. Hence, and to obtain a structure close to that of the human arm, it will need to return first of all to the anatomical studies to know the number and the geometrical position of that joints as well as its angular displacement. According to these anatomies, the human arm is consists from Wrist, Elbow, Radioulna and Shoulder Complex : glenohumeral joint, and shoulder girdle. Except the latter (Shoulder Complex), the corresponding joints are represented in the following figures (4.1, 4.2, 4.3, 4.4).

All these joints can be represented as a revolute joint having an angular limitation as shown in the figures.

As we will be interested in the contribution of the shoulder complex especially the shoulder girdle, a more detailed study on this part is presented below.
Shoulder complex is one of the complex mechanism in human body. Therefore, an exact kinematic model that describes this mechanism is difficulty obtained. In general, it

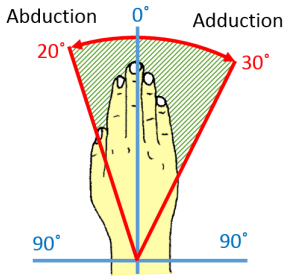

(a) Wrist abduction and adduction

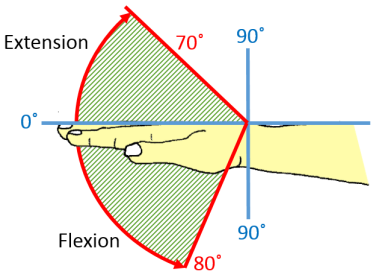

(b) Wrist flexion and extension

Figure 4.1: Wrist motion

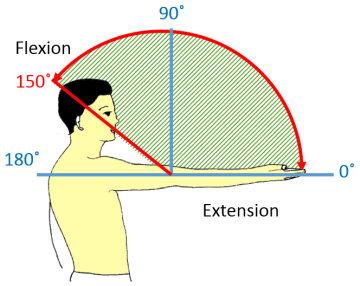

Figure 4.2: Elbow flexion and extension

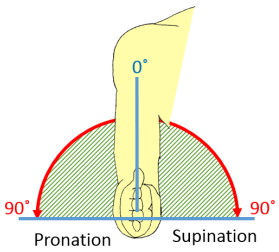

Figure 4.3: Radioulna pronation and supination

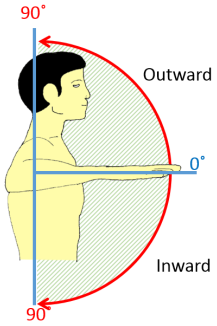

Figure 4.4: Inward and outward rotation

is composed of Inner and Outer joint. The Sterno-Clavicular (SC) joint occurs between the proximal end of the clavicle and the sternum. It allows a 3 DOF, Elevation and Depression, Protraction and Retraction, and axial rotation.

The Acromio-Clavicular (AC) joint exist between the acromion of the scapula and the distal end of the clavicle. All movements at this joint are passive; there is no muscle present which produce an active movement between the bones[5]. The Scapulo-Thoracic (ST) joint is a gliding joint which allows the scapula to glide over the thoracic[78][79]. Different model assumed that the ST joint can be modeled as 4 or 5 DOF [80][81]. All the presented joints are including in the inner joint of the shoulder complex and its called the Shoulder Girdle. The outer joint of the shoulder complex is called the Glenohumeral joint which occurs as a ball and socket joint between the humerus and glenoid fossa of the Scapula[5]. This large number of degree of freedom are associated with each other to offer the most mobile kinematic system in human body. The figures 4.5 and 4.6 present the different bones and joints for the shoulder complex.

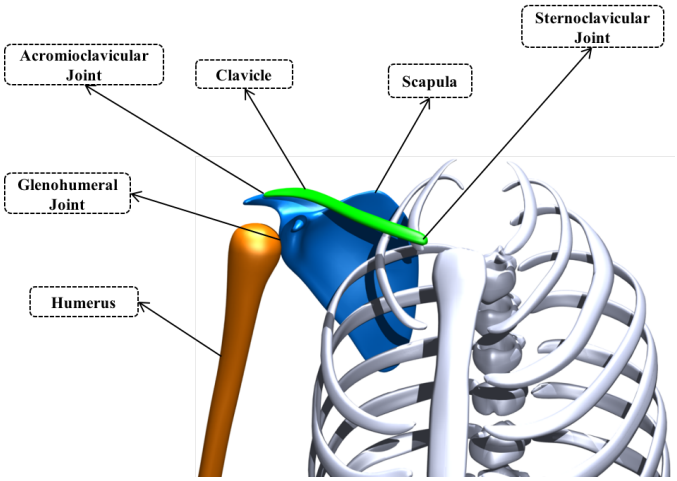

Figure 4.5: Bones of the Shoulder Complex[5]

As the glenohumeral joint is obviously could be modeled as ball and socket joint, the range of motion for its 3 DOF is presented in the figure 4.7.

In the other hand, an equivalent kinematic model for the shoulder girdle is still not determined due to the complex three-dimensional movements of such system. Nevertheless, it was illogical to ignore its contribution in increasing humerus mobility, therefore, some researchers have try to estimate this structure by different biologically-inspired engineering design, which is not purely mimicking biological systems, but focuses on engineering systems to have the same function as the system by taking inspiration from

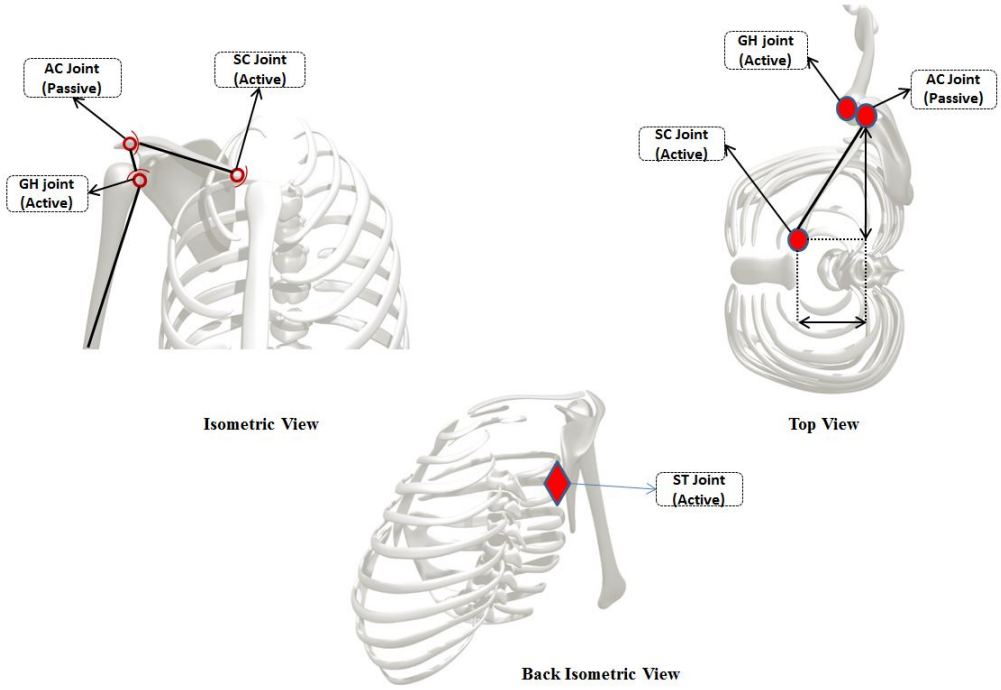

Figure 4.6: Joints of the Shoulder Complex[5]

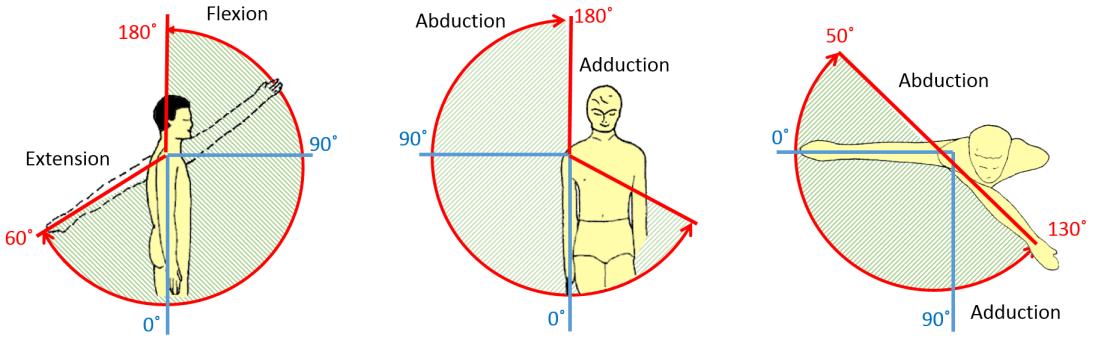

Figure 4.7: Glenohumeral flexion/extension, abduction/adduction and rotation

the biological knowledge [82]. However, other try to create a biomimetic design by reproducing the same musculoskeletal structure for the shoulder complex [83][84].

Engin and Tümer represents the shoulder complex by an open chain with a ball and socket joint for each SC, AC, and GH joints [85][86](Figure 4.8). In this model, they considered that the position of the GH joint is fixed relative to the thorax, which is an

wrong assumption, due to its variation during the movement of Scapula. In addition, this model present nine DOF for the shoulder complex.

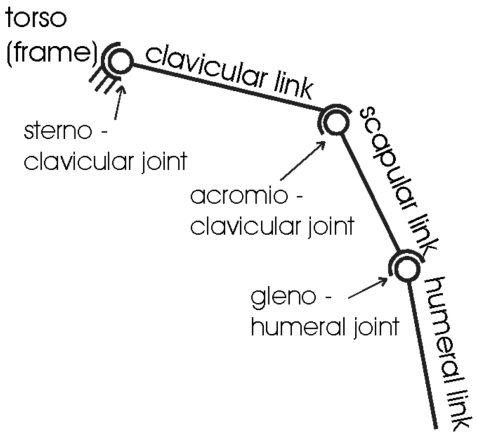

Figure 4.8: Engin and Tümer model for the shoulder complex

Klopcar et al. propose a shoulder complex with six degrees of freedom for both inner and outer joints (Figure 4.9). The shoulder girdle joint has two rotations, depression/elevation and retraction/protraction, and one translation, which are all dependent on the elevation angle of the humerus [80].

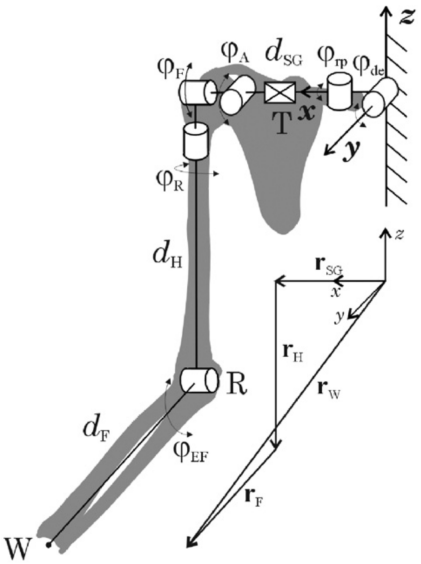

Figure 4.9: Klopcar et al. model for the shoulder complex

In the other hand, a closed kinematic chain for the shoulder girdle has been presented by Dvir and Berne[6]. This representation imposes too many constraints that complicate its mathematical modeling as well as its mechanical design (Figure 4.10).

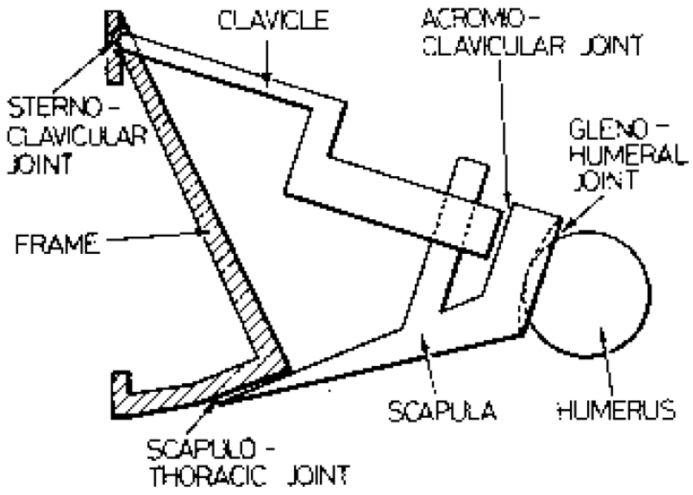

Figure 4.10: Dvir and Berne representation [6]

Starting from the complexity of the shoulder complex, the objective in the next sections is to carry out a kinematic synthesis based on several criteria in order to create a biomimetic robotic arm able to exhibit the same performances than the human arm ones. Obviously, the number of DOF as well as the relative position of their corresponding axes play an important role in the achievement of natural motion. Hence, still open questions have to be addressed: i) What is the suitable number of degrees of freedom that can reach the human arm dexterity? ii) What are the criteria that should evaluated upon? iii) How to deal with contradictory criteria?

4.2 Robotic Arm Kinematic Synthesis

The performance taken into account to carry out the kinematic synthesis process are based on the workspace of the robotic arm. Firstly, main properties of the workspace considered as a solid are taken into account. This concern the size, the shape and the

volume of the workspace. We will study all these criteria for 8, 9, 10, and 11 degrees of freedom for left robot arm. All of them have same links lengths. Looking to them as different robots will help us to propose which one is more suitable. In the following section the reference point (0, 0, 0) is always the center of shoulder girdle.

4.2.1 Forward geometrical model FGM

The Forward geometrical model FGM is used to determine position of the end-effector according to the joint's angles. In the following, we will develop the FGM for 11 DOF kinematic structure arm (3 in the shoulder girdle, 3 in the glenohumeral shoulder, 2 in the elbow complex and 3 in the wrist) . The FGM for any kinematic structure less than 11 DOF will be obtained from the same model by replacing the joint angles by 0. The figure 4.11 shows the kinematic structure for 11 DOF.
As we are interesting in the position X, Y and Z of the end effector, the 3 DOF of the wrist doesn't computed in the FGM because it hasn't any effect on these positions.
The parameter description based on the Khalil et al. notation is given on Table 4.1.

j	α_j	d_j	θ_j	r_j
1	0	0	θ_{s1}	0
2	$\frac{\pi}{2}$	0	$\theta_{s2}+\frac{\pi}{2}$	0
3	$-\frac{\pi}{2}$	0	$\theta_{s3}+\pi$	0
4	0	L_1	θ_1	0
5	$\frac{\pi}{2}$	0	$\theta_2-\frac{\pi}{2}$	0
6	$\frac{\pi}{2}$	0	$\theta_3+\pi$	0
7	$\frac{\pi}{2}$	0	$\theta_4+\frac{\pi}{2}$	0
8	$\frac{\pi}{2}$	0	$\theta_5+\pi$	0

Table 4.1: DH parameters for the 11 DOF arm structure

$$T_{r,s1}T_{s1,s2}T_{s2,s3}T_{s3,1}T_{1,2}T_{2,3}T_{3,4}T_{4,5}T_{5,e}=U_0$$

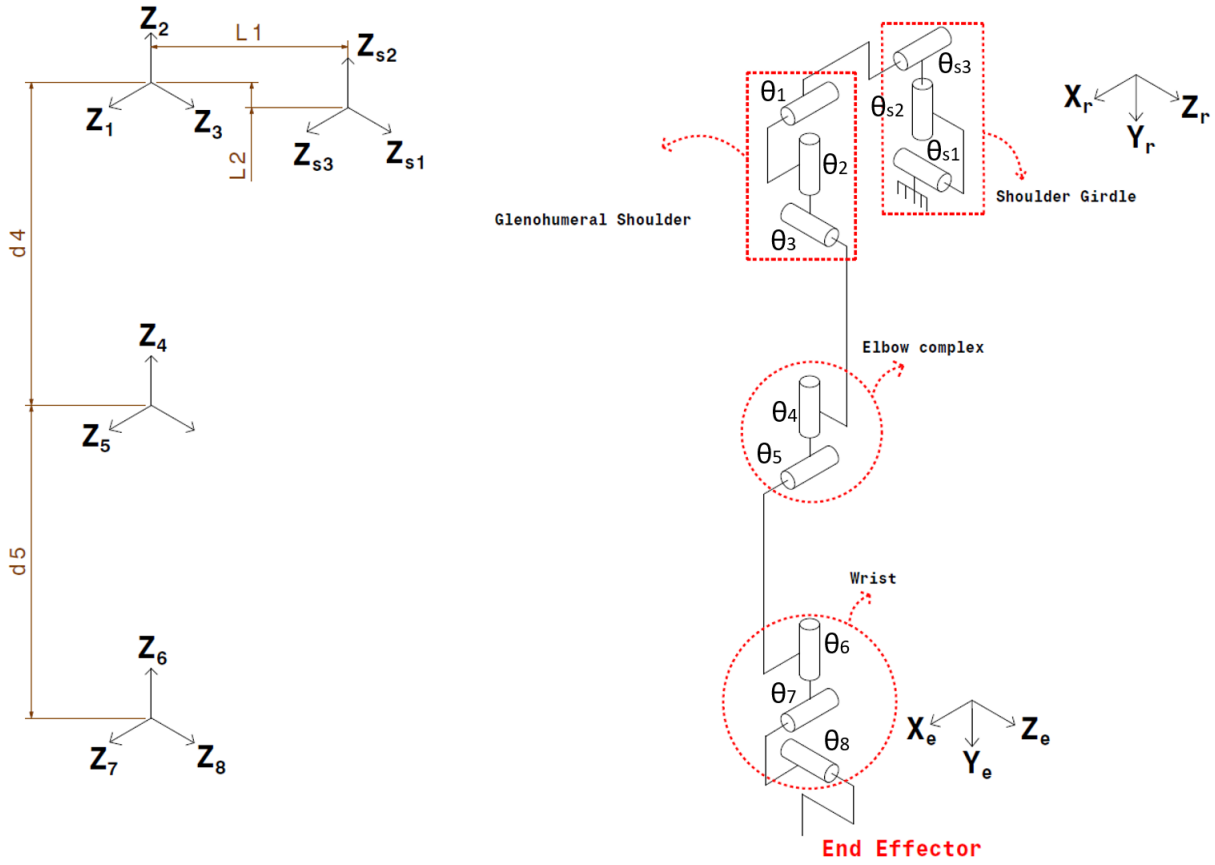

Figure 4.11: Kinematic model for 11 DOF arm structure

U_0=

$$\begin{pmatrix} s_x & n_x & a_x & X_e \\ s_y & n_y & a_y & Y_e \\ s_z & n_z & a_z & Z_e \\ 0 & 0 & 0 & 1 \end{pmatrix}$$

(X_e, Y_e, Z_e) is the coordinate vector of the end effector relative to the reference $(X_r Y_r Z_e)$. The DGM for this structure is written in the following equations:

$$X_e = f_1(\Theta_{s1}, \Theta_{s2}, \Theta_{s3}, \Theta_1, \Theta_2, \Theta_3, \Theta_4, \Theta_5, d_4, d_5, L_1, L_2) \tag{4.1}$$

$$Y_e = f_2(\Theta_{s1}, \Theta_{s2}, \Theta_{s3}, \Theta_1, \Theta_2, \Theta_3, \Theta_4, \Theta_5, d_4, d_5, L_1, L_2) \tag{4.2}$$

$$Z_e = f_3(\Theta_{s1}, \Theta_{s2}, \Theta_{s3}, \Theta_1, \Theta_2, \Theta_3, \Theta_4, \Theta_5, d_4, d_5, L_1, L_2) \tag{4.3}$$

with d_4, d_5, L_1, L_2 are a constants.

4.3 Structure Optimization

To have an optimal structure of the arm of a humanoid, it will be necessary to make a comparison with the proposed structure of the arm of a human being. This comparison is based first of all on the volume of the workspace of each of the proposed structures. We consider that the kinematics of the arm remains similar from the glenohumeral shoulder to the wrist and that our optimization will be achieved on the girdle shoulder part. The distance between the joints is equal to the average height of a man who has the same dimensions as HYDROïD robot.

In this study, we assess the anthropomorphism of 3 different structures of the robot arm 4.12. These structures are extracted from the 11 DOF model presented in the figure 4.11. The first structure is considered without the axial rotation joint $\theta_2 s$, the second structure is modeled without Elevation and Depression joint $\theta_3 s$, and the last structure is modeled like the almost humanoid robot arm which presented without the shoulder girdle. All these structures were compared with the 11 DOF in order to obtain an optimized structure without loosing capabilities. As the protraction and retraction joint $\theta_1 s$ is almost neglected, it will take a zero value during the calculation.

4.4 Comparison approach

4.4.1 Convex hull

The convex hull of a set point S is described as the smallest convex envelop which surround S. It is the intersection of all convex portions containing S.

$$Conv(S) = \cap\, C_i$$

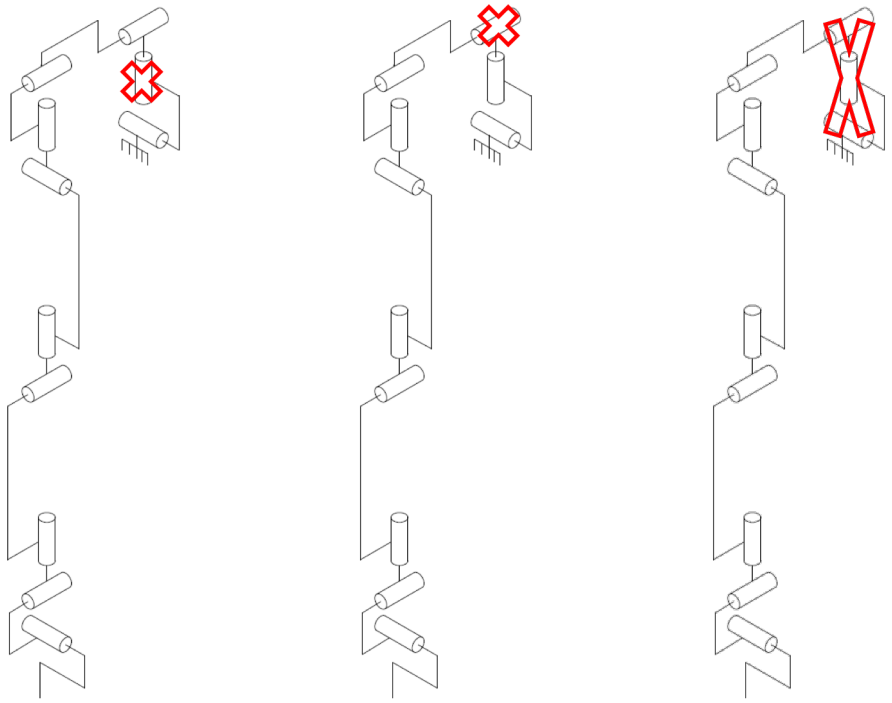

(a) Structure 1 (b) Structure 2 (c) Structure 3

Figure 4.12: Proposed structures for optimization

(C is a convex that contains S)

If S is a finite set of points, EC (S) is a convex polygon of which the vertices are inside S. There are different algorithms to compute the convex hull of a set S of points like algorithm of Jarvis, algorithms of Graham, or algorithm of Monotone chain.... In our approach we will use the quickhull algorithm presented in [87].

Before calculating the convex hull for each structure, the specific direct geometric model, presented before, was used to derive the corresponding working space W_i. Afterwards, the convex hull could be calculated and its volume and surface will be used to determine the anthropomorphic rate of the proposed structure with that of the human arm.

The Convex hull of the 11 DOF model is represented by CH_0 and the convex hull of the 3 other structures are represented by CH_i with $i \in \{1,2,3\}$. The figure 4.13 presents the convex hull for the workspace of the 11 DOF.

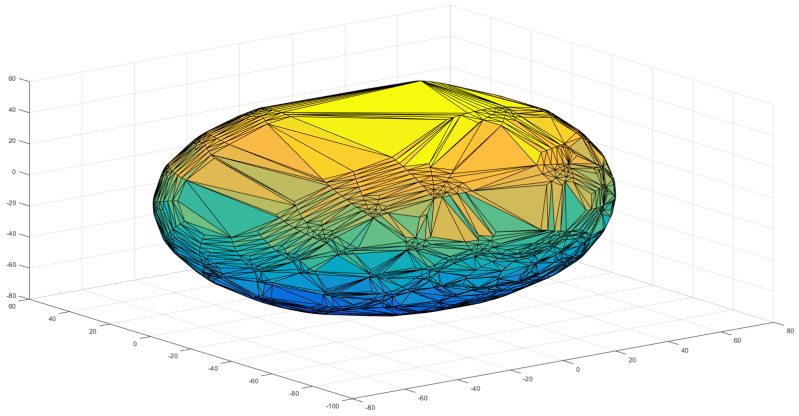

Figure 4.13: Convex hull for 11 DOF kinematic model

The volume and the area of this convex hull will be equivalent to those of the real workspace. Therefore, our approach consist in comparing the volume of each structure to that of the human arm by using the following equations:

$$V_i = \frac{Vol(CH_i)}{Vol(CH_0)} x100$$

$$A_i = \frac{A(CH_i)}{A(CH_0)} x100$$

with V_i represents the rate of volume of the i structure relative to that of human arm, $Vol(CH_i)$ is the volume of the convex hull for the i structure, A_i is the rate of area of the i structure relative to that of human arm and finally $A(CH_i)$ is the area of the convex hull for the i structure.

4.5 Result and analysis

In this section we will present the anthropomorphism rate for each structure by computing the corresponding volume and area rates. The results are derived and presented in the table 4.2.

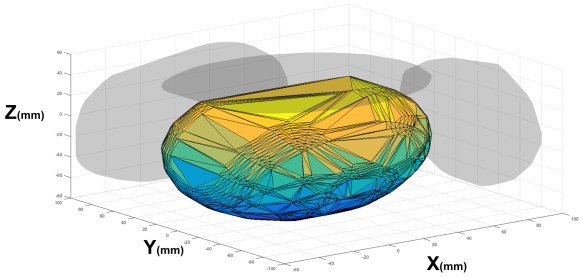

(a) Convex hull for structure 1

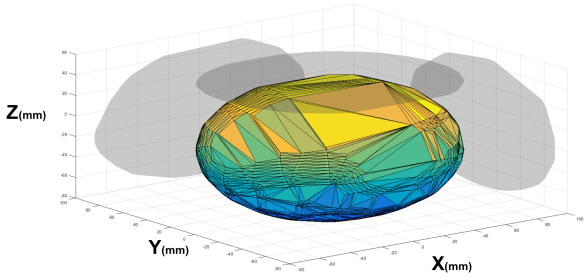

(b) Convex hull for structure 2

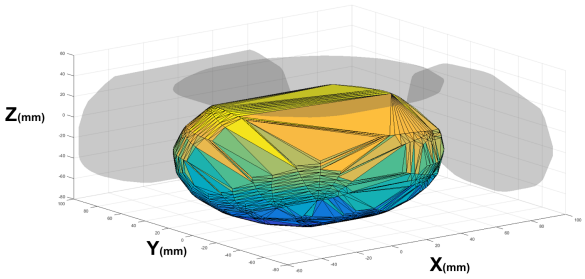

(c) Convex hull for structure 3

Figure 4.14: Convex hull and shadow projections for each structure

Structure	**Volume rate** V_i	**Area rate** A_i
1	86,92 %	91,63 %
2	88,76 %	92,76 %
3	73,94 %	82,55 %

Table 4.2: Anthropomorphism rate for the 3 proposed structures

From table 4.2, we can conclude that the volume and the area of the workspace for the structure 2 are closest to those of the human arm.

4.6 Centroid

The centroïd of the workspace for each structure has been calculated in order to get an idea about the orientation of each workspace. For this, we consider that each accessible point in the 3D space having the weight of a unit, Therefore, the calculation of the

centroïd is derived from the following equation :

$$C_{ix} = \frac{\sum_{n=1}^{n} m_i X_i}{\sum_{n=1}^{n} m_i}$$

$$C_{iy} = \frac{\sum_{n=1}^{n} m_i Y_i}{\sum_{n=1}^{n} m_i}$$

$$C_{iz} = \frac{\sum_{n=1}^{n} m_i Z_i}{\sum_{n=1}^{n} m_i}$$

with C_i represents the centroïd coordinates relative the frame reference, m_i is the weight of the accessible point which is considered equal to 1, X_i, Y_i, ,Z_i are the coordinates of the accessible point.

The results are presenting in the table 4.3.

Structure	X_c (mm)	Y_c	Z_c
human arm	3,77	-13,02	-34,83
1	1,96	-6,51	-18,14
2	1,26	-0,52	-12,72
3	0,98	-0,38	-9,94

Table 4.3: Centroïd coordinates for each structure

4.7 Conclusion

In this chapter, we proposed kinematic structure for the robot arm based on a systematic approach to quantify the anthropomorphism of robot arms. A comparison was performed for three kinematically different robot arm models. The proposed methodology provide specifications for the design of the next version of HYDROïD robot arm. Finally, the proposed configuration will help to attain an enhancement for the robot dual-arm by improving its working accessibility.

Chapter 5

HYDROïD trunk design and Experimental validation

Contents

In this chapter, we will present the mechanical design of the torso and the 8th degree of freedom of the arm . The aim of these mechanisms is to support the needed load and to reach the principal motions in order to furnish the desired mobility. We always should remember that our important constraint is to obtain an anthropomorphic design by respecting all the geometrical and kinematic constraints. In addition, this design should also fulfill a very important conditions: light weight, high stiffness and low cost.

5.1 Design Specifications

Before initiating the design of a prototype, a specification booklet containing the constraints and requirements must be provided to the designer. For our application, the first constraints consist in respecting the kinematics of the model as well as the geometric and inertial properties. The constraints on the supplied power as well as on the maximum speeds of the moving bodies must be respected also when choosing the driving system. The tables 5.1 and 5.1 represents the required specifications

Torso			
Joint	**Range of motion (°)**	**Maximum speed (°/s)**	**Maximum Torque @ 120 bars (N/m)**
Flexion / Extension (TFE)	-25/+50	230	350
Lateral Flexion (TLF)	±40	245	450
Vertical Rotation (TVR)	±25	200	350
Lumbar Flexion / Extension (LFE)	±40	275	350

Table 5.1: Specification for the Torso

5.2 Virtual model

A virtual model for HYDROïD torso was built using Adams. This model allows us to obtain a full study (modeling, simulating, optimizing, refining...) for our mechanism by giving us the capability to change all the parameters and study the effects of this changing on the mechanism. All the parts were imported as step files from Catia to Adams and conserving all its parameters such as mass, inertia and geometrical dimensions. Firstly this model is used to verify the inverse Geometrical model calculated in the modeling section. The analytic model was programmed in C++ and linked to Adams virtual model. Figure 5.2 presents a video snapshots for the simulation of the mechanism.

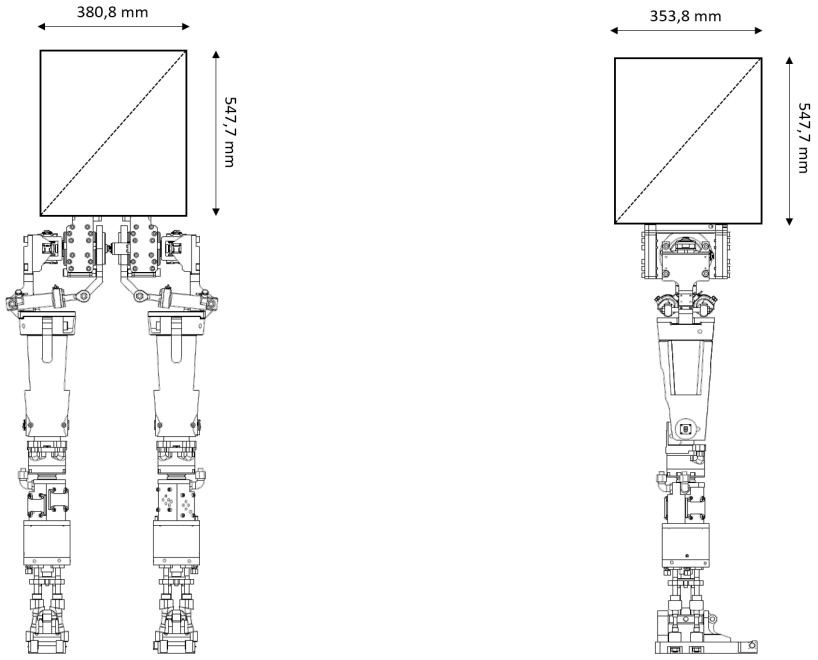

(a) Front View (b) Side View

Figure 5.1: Geometrical Constraints for the Torso

5.3 Prototype of Torso

Figure 5.3 represents the characteristic of the proposed hybrid mechanism. The sagittal and the transversal (vertical) motion are obtained using a parallel mechanism serially connected with the other joint (Frontal and the 4th DOF).

Once all the kinematic structure has been validated and based on the previous analyzes, the torso mechanism for HYDROïD was designed. Figure 5.3 gives the design structure of the hybrid mechanism of the torso. Figure 5.4 present the CAD and torso real prototype for the torso.

An important step in designing a system is the choice of materials. Since these systems are dedicated to humanoid robotic applications, it is very important to reduce the total weight and to have the lightest possible system. In addition, since hydraulics have been used as an actuating source, it is therefore necessary to make a judicious choice of the materials of the moving parts in order to guarantee appropriate contact surfaces. Finally, it is important that all of the parts support the static and dynamic efforts during

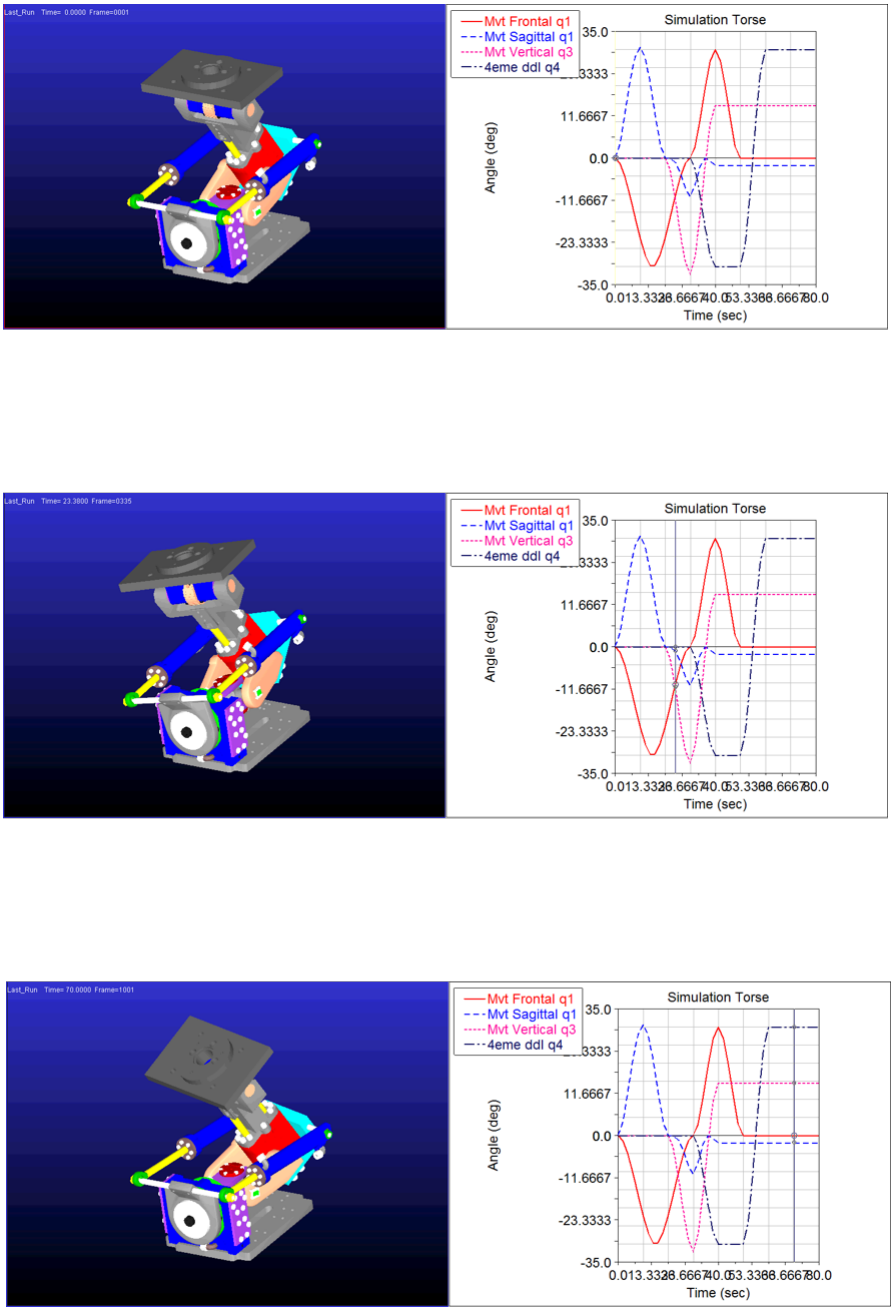

Figure 5.2: Virtual model of the Torso

the required charge.

For the torso, the total weight of the system is approximately 20 Kg also respecting the constraint on the total weight of the prototype imposed by the specifications.

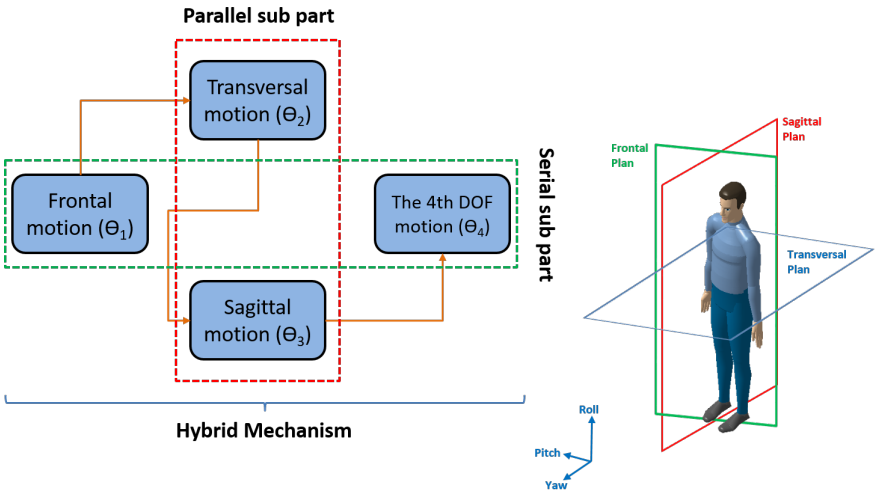

Figure 5.3: Hybrid Mechanism of the Torso

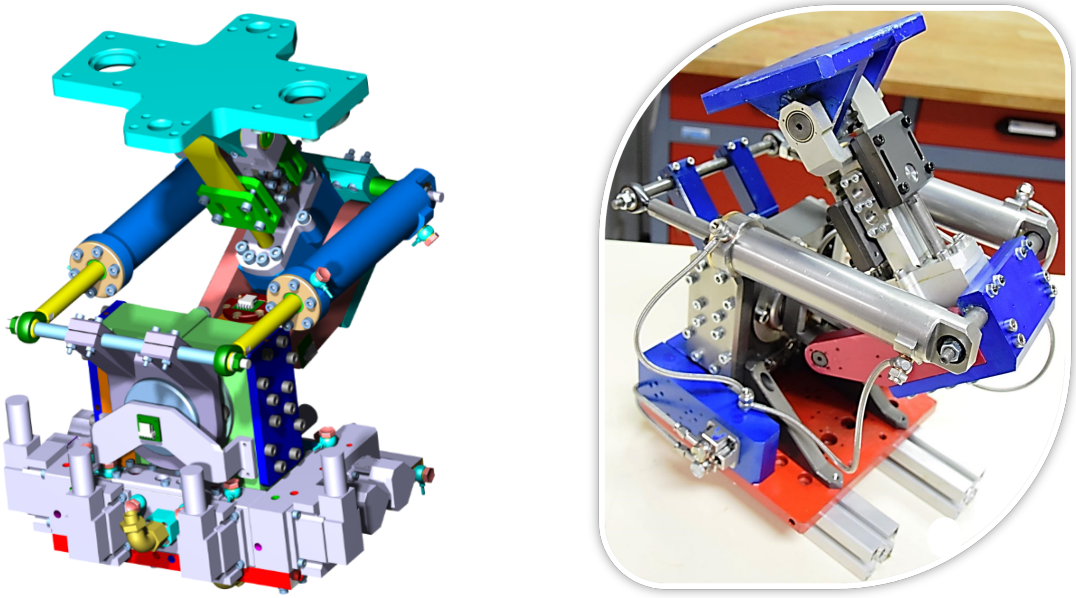

(a) CAD design

(b) Real design

Figure 5.4: Prototype of the Torso

The figures 5.5, 5.6, 5.7 and 5.8 shows the proposed mechanism used for each joint of the torso.

This first prototype was cleaned and tested joint by joint to check the operation of each mechanism as well as the tightness of our hydraulic integrated system.

The joints are controlled by a hydraulic servo valves which subsequently control the flow of oil sent to the pistons, and thus directly affects its own speeds. Two pressure sensors and a position sensor have been integrated for each link to allow the development of a strategy of compliant commands based on both force and position control.

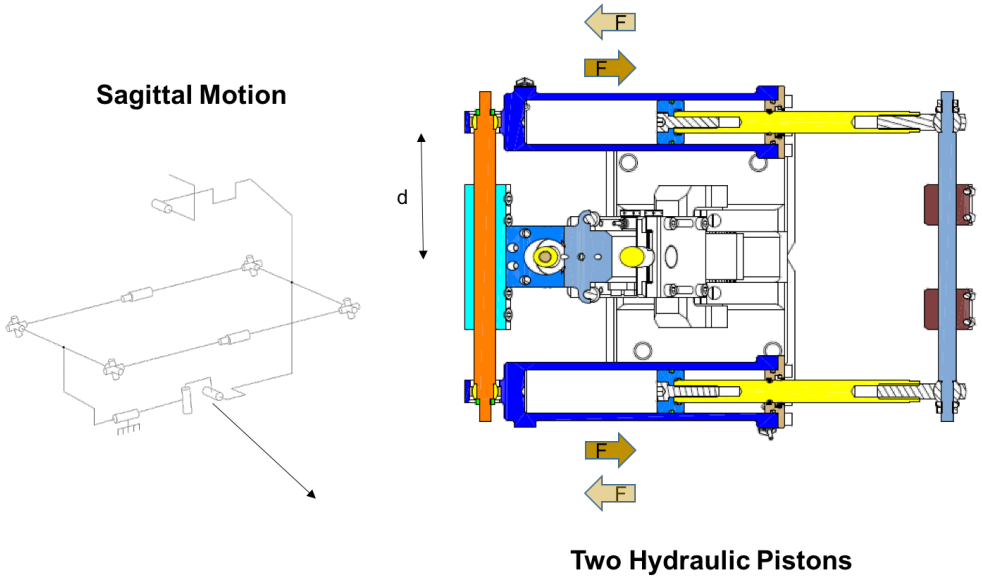

Figure 5.5: Sagittal motion mechanism

5.4 Experiments

The torso system was tested by an external hydraulic unit. Using this central hydraulic group, preliminary results have shown the performance of the various designed and realized mechanisms . Figures 5.9, 5.10 and 5.11 present the preliminary results of torso provided from a video snapshots. The mechanism is designed to withstand a maximum pressure of 120 bar.

5.5 The 8th DOf of the arm

The shoulder girdle of the arm contains one degree of freedom actuated by hydraulic pistons. The range of motion of this DOF is -30deg to $+30$ *deg*. This DOF allows

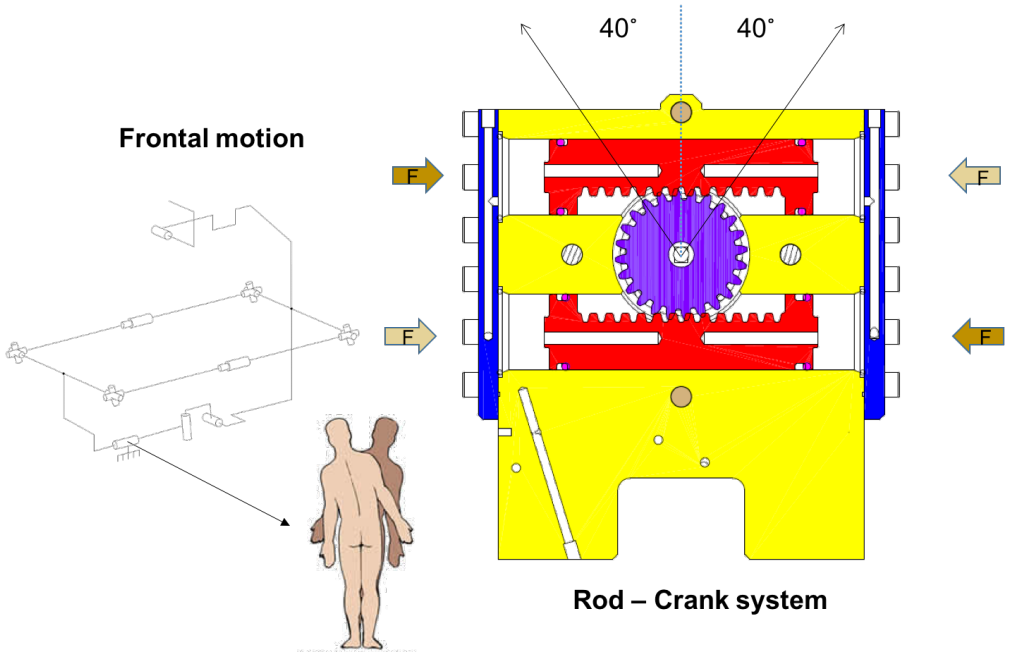

Figure 5.6: Frontal motion mechanism

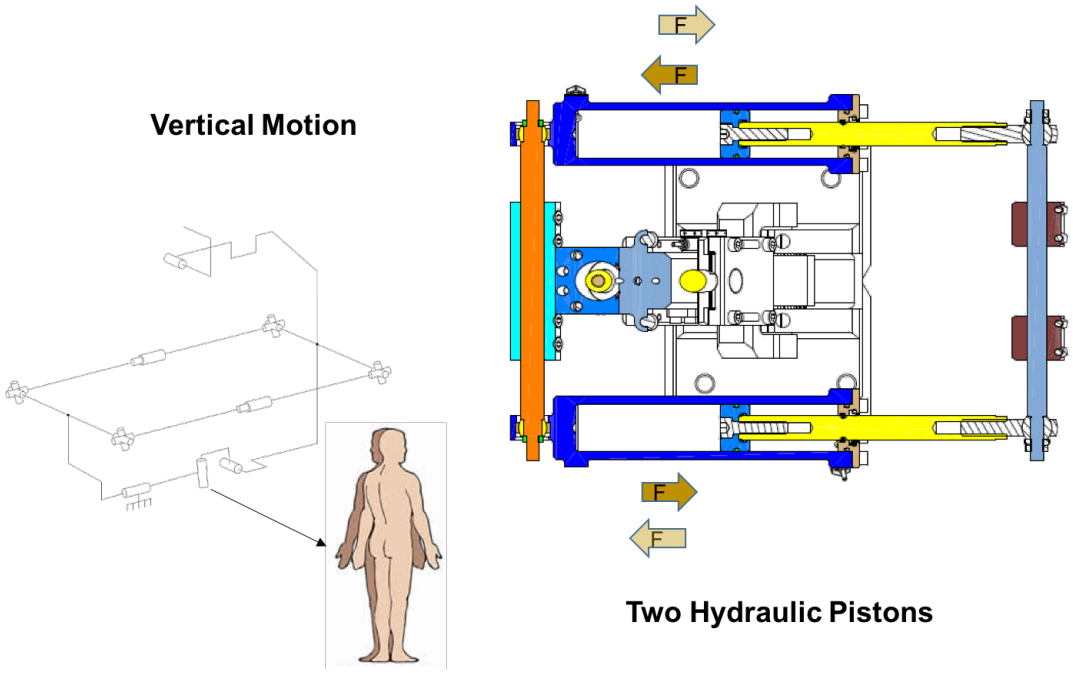

Figure 5.7: Vertical motion mechanism

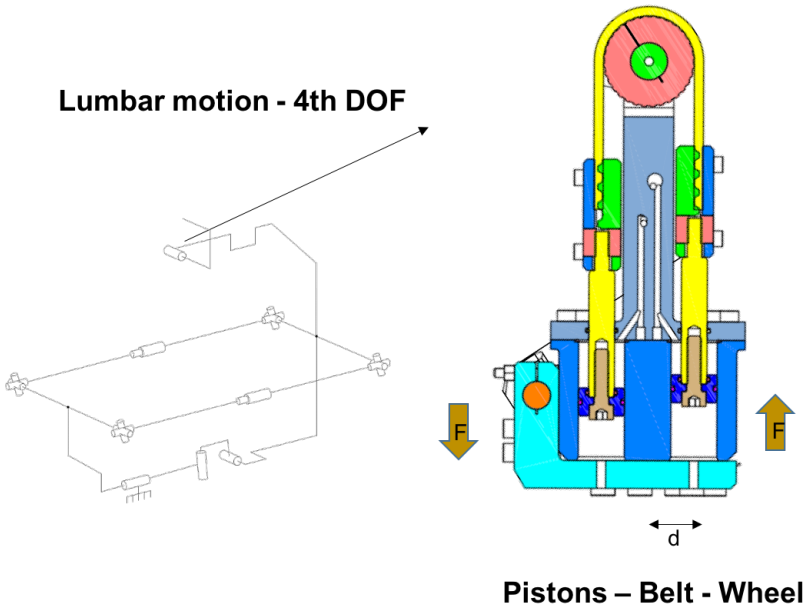

Figure 5.8: Lumbar motion mechanism

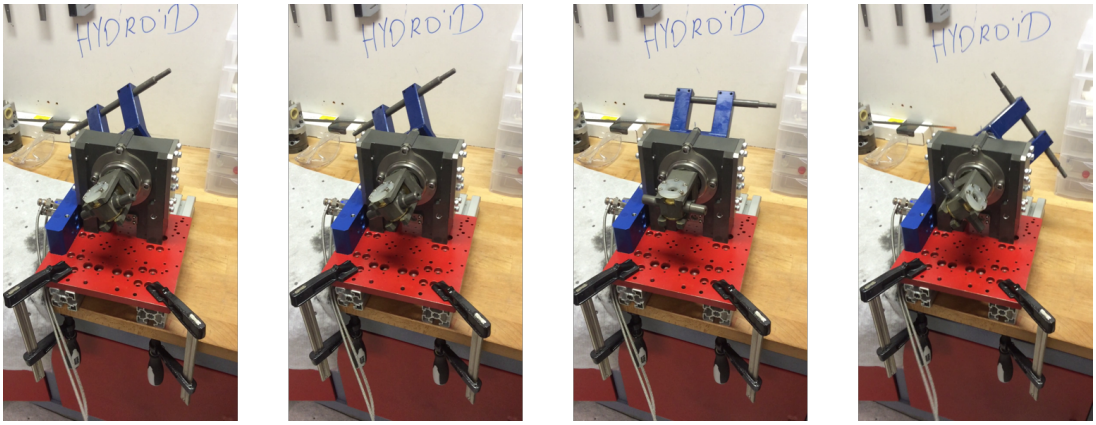

Figure 5.9: Frontal mechanism testing

the arm to rotate in the transversal plan in order to increase the workspace of the whole structure. The hydraulic pistons exerts force on the axis A1 and A2 while B1 and B2 are always fixed (Figure 5.12) . These forces allow the base of the shoulder girdle, which are linked with the gear via grooved toothing connection, to rotates around the vertical axis; Thanks to the thrust bearing for supporting the axial load and for the conical bearing

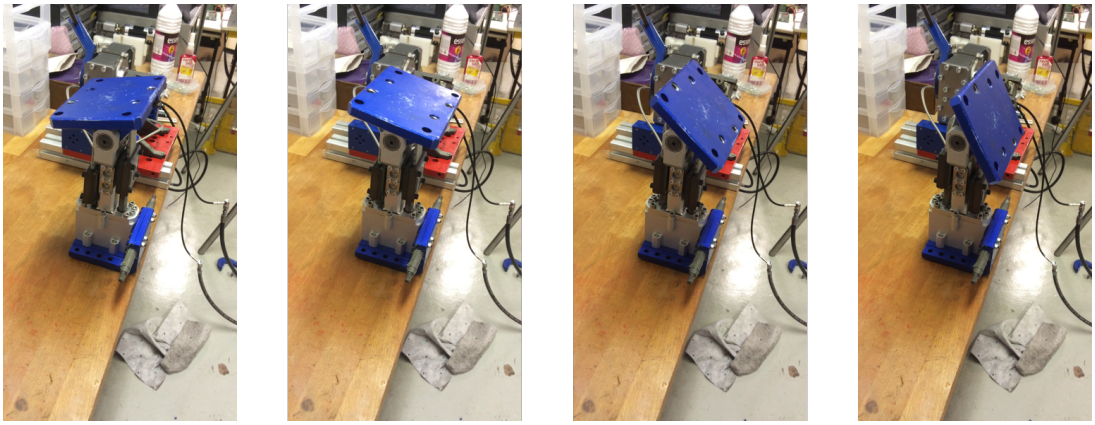

Figure 5.10: Lumbar mechanism testing

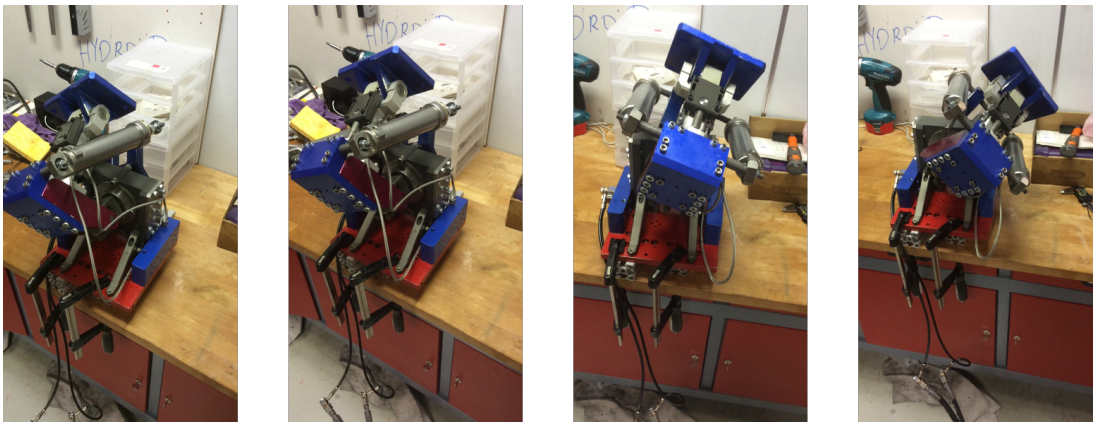

Figure 5.11: Torso mechanism testing

which support the axial and radial force. The shoulder girdle design is characterized by its compactness; All hydraulic circuit are integrated into the shoulder base; the other hydraulic component such as the proportional sevo-valve and hydraulic connectors are implemented in a small workspace.

The same technique as that used previously, in the torso also equips this mechanism. The figure 5.12 shows two sections for the girdle system.

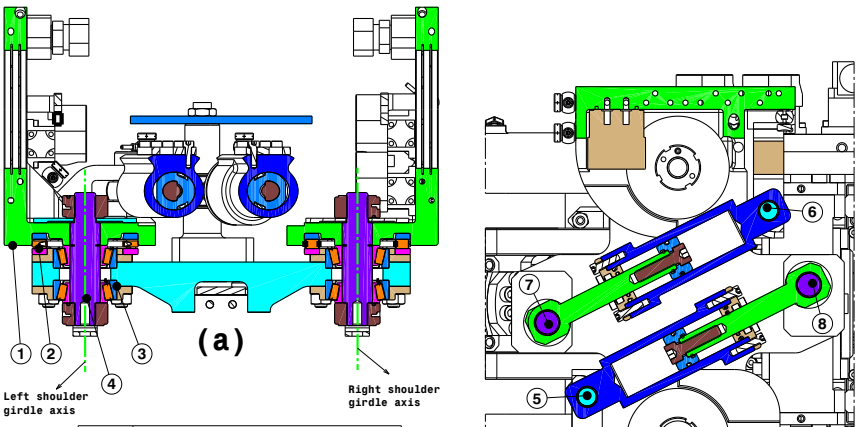

1	Base of the shoulder girdle
2	Thrust bearing
3	Conical bearing
4	Gear
5	Axis A1
6	Axis A2
7	Axis B1
8	Axis B2

Figure 5.12: (a): Cross section for the shoulder girdle axis, (b) Cross section for the hydraulic pistons

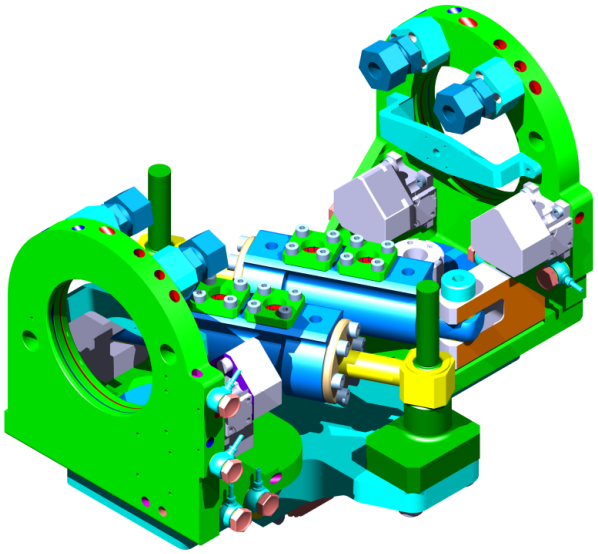

Figure 5.13: CAD for the 2 shoulder girdle joints

5.6 HYDROïD upper part

After the end of the design stage, an assembly of the whole upper part must be put in place. Figure 5.14 presents the upper part of HYDROïD containing the torso with the four degree of freedom and the joint of the shoulder girdle. This part has been developed with a minimum of use of hydraulic hoses which have the effect of increasing the resistance applied on the joints as well as increasing the human aspect necessary for the lasting and secure interaction. All the servo valves have been positioned in such a way as to have a very compact system to respect the geometric constraints presented in the specifications.

Figure 5.15 represents the kinematic structure of the upper part of HYDROïD robot, without its head, which contains 20 revolute joints (8 DOF per arm and 4 DOF for the Torso).

Figure 5.16 shows the main angular displacement of the joints in both side and upper view.

Figure 5.2 gives the main specifications of the upper part of the HYDROïD. We can see that the maximum reach length per arm increase by more than 40% when we use our four DOF Torso.

HYDROïD Upper part	
Structure	Articulated
Payload	up to 10 Kg/arm (re-configurable with requirement)
Horizontal Reach per arm without Torso	648,5
Vertical Reach per arm without Torso	648,5
Maximum length Reach per arm with Torso	920 mm

Table 5.2: Upper part specification

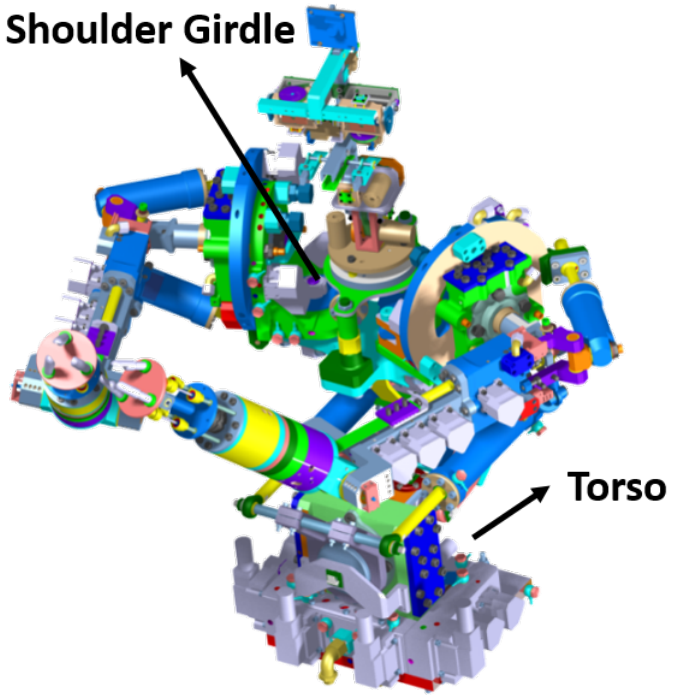

Figure 5.14: Upper part of HYDROïD

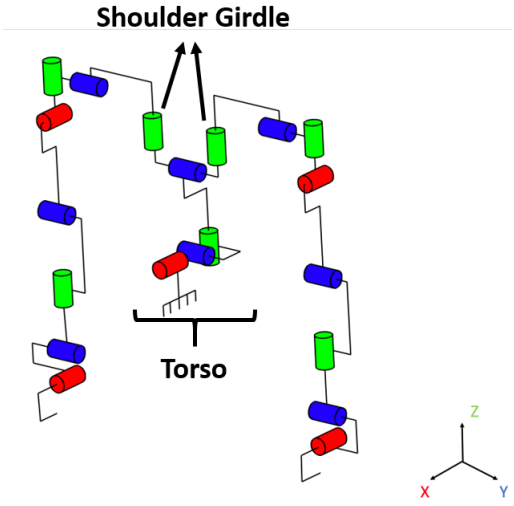

Figure 5.15: Kinematic structure of the upper part of HYDROïD

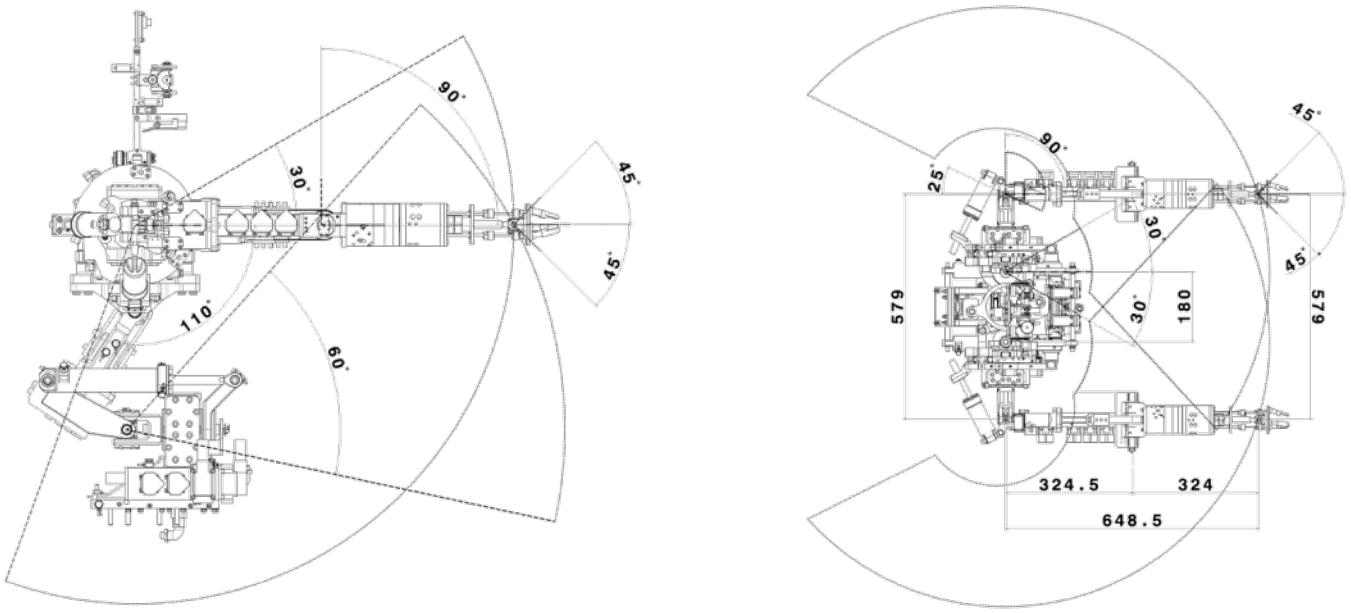

Figure 5.16: Side and upper view for HYDROïD's upper part

5.7 conclusion

In this chapter, the details of the design of the torso and shoulder of the HYDROïD robot were presented. The design work went through several challenges, from the 3D design phase, through the determination of the necessary components, the realization of the manufacturing plans, the reception and the assembly of the parts until the first tests. All these phases have been carefully accomplished while benefiting from the experience of the directors as well as the contact with the necessary industries.

Chapter 6

Conclusion and Perspectives

6.1 Conclusion

The work carried out in this thesis has two essential axes whose aim is to improve the kinematics of the upper part of the HYDROïD robot. From a biomechanical study, a multi-body model simulating the spine of a human being was presented to identify its effect on the work space of the robot. this identification first served us the importance of developing a torso with more complex kinematics than existing systems of two or three degrees of freedom and more functional than systems with tens of degrees of freedom in the torso. The dynamic study that followed showed that the addition of a degree of freedom in the sagittal plane has a positive effect on the energy consumed during a bipedal walk. For this reason, we adopted a hybrid kinematics of 4 degrees of freedom (DOF) for the torso of the robot distributed in 3 DOF at the lumbar(RPY) level and one pitch DOF at the thoracic level.

The second part was to carry out a kinematic synthesis based on several criteria in order to create a biomimetic robotic arm able to exhibit the same performances than the human arm ones. This new proposed structure for the shoulder improves the kinematic of the arms by increasing the volume and the weight of its workspace. Hence, it can attain a remarkable enhancement for the robot dual-arm by improving its working accessibility.

Later, an analysis of the connections made it possible to identify the mechanism of the torso while respecting all the necessary constraints. A generic hybrid mechanism, dedicated to the realization of the torso, consisting of the linear and rotary actuators has been developed to accomplish all the movements envisaged. The IGM model for the generic solution was established and its adaptation to the particular case of the torso was identified. An optimized solution for the mechanisms was given. The optimization process was based on two criteria: maximum output quasi-static torque for yaw and roll axes and minimum stroke for the linear actuators for a maximum range of angular motion.

Finally, the design of the mechanisms has been carried out, the actuation has been selected with a focus on hydraulic joints design.

The work in this thesis opens important perspectives in different terms to answer the problems already mentioned in the general introduction such as designed a fully anthropomorphic and friendly character for a humanoid robot.

In short term, the robot must be completely assembled and tested to check the sequence of all joints as well as the internal hydraulic circuits. then, a thesis work will continue on the control of the torso. The objective is to maintain the balance of the robot by controlling the articular motion of the torso without knowing the trajectories of the locomotion apparatus. In the long term, it will be necessary to control all the joints of the robot in order to ensure its balance during a walking speed.

Once the prototype is ready, we envisage to establish a procedure for estimating the consumed power with and without the contribution of the torso structure. This will help us to have a complete and detailed vision on the importance of a flexible structure on the consumed energy during walking.

In addition, the new structure of the arm must be set up to study its dynamic effect necessary to balance during robot operation. This structure must be mounted with another arm to study the effect of dual arms on the manipulability of the HYDROïD.

In the medium term, the work done on the development of a low mass linear hydraulic actuator must be integrated directly into HYDROïD robot in order to minimize its total mass. The effect of vibration and the ground reaction force reaction must be

studied to improve the design of the actuator especially at its attachment points.

Finally, The kinematic structure developed for the parts of the robot is an asset to simulate the movement of human joints as well as its center of gravity. This, in the long term, should allow this robot to be used as an experimental platform for medical devices such as prostheses and orthoses.

Bibliography

[1] R. S. Snell, *Clinical Anatomy by Regions*. Lippincott Williams and Wilkins., 2008.

[2] D. I. Miller and W. E. Morrison, "Prediction of segmental parameters using the Hanavan human body model.," 1975.

[3] M. M. PANJABI, K. TAKATA, V. GOEL, D. FEDERICO, T. OXLAND, J. DURANCEAU, and M. KRAG, "Thoracic Human Vertebrae Quantitative Three-Dimensional Anatomy," *SPINE*, vol. 16, no. 8, pp. 888–901, 1991.

[4] R. Konz, S. Fatone, and S. Gard, "Effect of restricted spinal motion on gait," *The Journal of Rehabilitation Research and Development*, vol. 43, no. 2, p. 161, 2006.

[5] I. a. Murray, "Determining upper limb kinematics and dynamics during everyday tasks," *Ph.D Thesis, Centre for Rehabilitation and Engineering Studies, University of Newcastle upon Tyne*, no. November, pp. 1–470, 1999.

[6] Z. Dvir and N. Berme, "The shoulder complex in elevation of the arm: A mechanism approach," *Journal of Biomechanics*, vol. 11, no. 5, pp. 219–225, 1978.

[7] P. M. Cholewicki J, Crisco JJ 3rd, Oxland TR, Yamamoto I, "Effects of posture and structure on three-dimensional coupled rotations in the lumbar spine. A biomechanical analysis.," *SPINE*, vol. 21, 1996.

[8] S. P. Moroney, A. B. Schultz, J. A. A. Miller, and G. B. J. Andersson, "Load-displacement properties of lower cervical spine motion segments," *Journal of Biomechanics*, vol. 21, no. 9, pp. 769–779, 1988.

[9] F. A. Pintar, N. Yoganandan, T. Myers, A. Elhagediab, and A. Sances, "Biomechanical properties of human lumbar spine ligaments," *Journal of Biomechanics*, vol. 25, no. 11, pp. 1351–1356, 1992.

[10] J. Goetz, S. Kiesler, and A. Powers, "Matching robot appearance and behavior to tasks to improve human-robot cooperation," in *The 12th IEEE International*

Workshop on Robot and Human Interactive Communication, 2003. Proceedings. ROMAN 2003., pp. 55–60, Oct 2003.

[11] D. Li, P. L. P. Rau, and Y. Li, "A cross-cultural study: Effect of robot appearance and task," *International Journal of Social Robotics*, vol. 2, no. 2, pp. 175–186, 2010.

[12] S. Alfayad, *Robot Humanoide HYDROïD : Actionnement, Structure cinématique, et Stratégie de Contrôle*. PhD thesis, Université de Versailles, Versailles, France, 2009.

[13] S. Alfayad, F. B. Ouezdou, and F. Namoun, "New three DOF ankle mechanism for humanoid robotic application: Modeling, design and realization," in *2009 IEEE/RSJ International Conference on Intelligent Robots and Systems, IROS 2009*, pp. 4969–4976, 2009.

[14] S. Alfayad, F. B. Ouezdou, and F. Namoun, "New 3-DOFs Hybrid Mechanism for Ankle and Wrist of Humanoid Robot: Modeling, Simulation, and Experiments," *Journal of Mechanical Design*, vol. 133, no. February 2011, p. 021005, 2011.

[15] S. Alfayad, A. M. Tayba, F. B. Ouezdou, and F. Namoun, "Kinematic Synthesis and Modeling of a Three Degrees-of-Freedom Hybrid Mechanism for Shoulder and Hip Modules of Humanoid Robots," *Journal of Mechanisms and Robotics*, vol. 8, no. 4, p. 41017, 2016.

[16] S. Alfayad, M. El Asswad, A. Abdellatif, F. B. Ouezdou, A. Blanchard, N. BeaussÃl', and P. Gaussier, "HydroÃŕd humanoid robot head with perception and emotion capabilities: Modeling, design, and experimental results," *Frontiers in Robotics and AI*, vol. 3, p. 15, 2016.

[17] J.-C. Ceccato, *Le tronc de la locomotion à la commande*. PhD thesis, Université Montpellier2, Montpellier, France, 2009.

[18] K. H. Eliane N. Marieb, *Human Anatomy and Phisiology*. Pearson education, Inc, 2010.

[19] J. Wicke, G. A. Dumas, and P. A. Costigan, "A comparison between a new model and current models for estimating trunk segment inertial parameters," *Journal of Biomechanics*, vol. 42, no. 1, pp. 55–60, 2009.

[20] E. Hanavan, "A mathematical model of the human body. AMRL-TR-64-102," *Aerospace*, pp. 1–149, 1964.

[21] C. E. Clauser, J. T. McConville, and J. W. Young, "Weight, Volume, and Center of Mass of Segments of the Human Body," *National Technical Information Service*, pp. 1–112, 1969.

[22] Y. Sakagami, R. Watanabe, C. Aoyama, S. Matsunaga, N. Higaki, and K. Fujimura, "The intelligent ASIMO: system overview and integration," *IEEE/RSJ International Conference on Intelligent Robots and System*, vol. 3, no. October, pp. 2478–2483, 2002.

[23] "Current and future perspective of Honda humamoid robot," *Proceedings of the 1997 IEEE/RSJ International Conference on Intelligent Robot and Systems*, pp. 500–508.

[24] "History of honda's robot development." http://world.honda.com/ASIMO/history/p1_p2_p3/index.html.

[25] J. Y. Kim, I. W. Park, and J. H. Oh, "Design and Walking Control of the Humanoid Robot, KHR-2 (KAIST Humanoid Robot-2)," *Proceedings of International Conference on Control, Automation and Systems*, vol. 2, pp. 1540–1543, 2004.

[26] I. W. Park, J. Y. Kim, J. Lee, and J. H. Oh, "Mechanical design of humanoid robot platform KHR-3 (KAIST humanoid robot - 3: HUBO)," in *Proceedings of 2005 5th IEEE-RAS International Conference on Humanoid Robots*, vol. 2005, pp. 321–326, 2005.

[27] H. Ulbrich, T. Buschmann, and S. Lohmeier, "Design and Realization of Humanoid Robots at AM-TUM," no. Diname, 2007.

[28] J. Englsberger, A. Werner, C. Ott, B. Henze, M. A. Roa, G. Garofalo, R. Burger, A. Beyer, O. Eiberger, K. Schmid, and A. Albu-Schäffer, "Overview of the torque-controlled humanoid robot TORO," *IEEE-RAS International Conference on Humanoid Robots*, vol. 2015-February, pp. 916–923, 2015.

[29] K. Kaneko, F. Kanehiro, M. Morisawa, K. Akachi, G. Miyamori, A. Hayashi, and N. Kanehira, "Humanoid robot HRP-4 - Humanoid robotics platform with lightweight and slim body," in *IEEE International Conference on Intelligent Robots and Systems*, pp. 4400–4407, 2011.

[30] S. Lohmeier, T. Buschmann, H. Ulbrich, and F. Pfeiffer, "Modular joint design for performance enhanced humanoid robot lola," in *Proceedings 2006 IEEE International Conference on Robotics and Automation, 2006. ICRA 2006.*, pp. 88–93, May 2006.

[31] "Reem-c robot." http://pal-robotics.com/en/products/reem-c/.

[32] B. J. Stephens, "State estimation for force-controlled humanoid balance using simple models in the presence of modeling error," *Proceedings - IEEE International Conference on Robotics and Automation*, no. May, pp. 3994–3999, 2011.

[33] "Boston dynamics robots." http://www.bostondynamics.com.

[34] "Optimization-based locomotion planning, estimation, and control design for the atlas humanoid robot," *Autonomous Robots*, vol. 40, no. 3, pp. 429–455, 2016.

[35] "Romeo project." http://projetromeo.com.

[36] N. Pateromichelakis, A. Mazel, M. A. Hache, T. Koumpogiannis, R. Gelin, B. Maisonnier, and A. Berthoz, "Head-eyes system and gaze analysis of the humanoid robot Romeo," in *IEEE International Conference on Intelligent Robots and Systems*, pp. 1374–1379, 2014.

[37] A. Dietrich, M. Kimmel, T. Wimböck, S. Hirche, and A. Albu-Schäffer, "Workspace analysis for a kinematically coupled torso of a torque controlled humanoid robot," *Proceedings - IEEE International Conference on Robotics and Automation*, pp. 3439–3445, 2014.

[38] "Twendyone concept." http://www.twendyone.com/concept_e.html.

[39] H. Iwata and S. Sugano, "Design of human symbiotic robot TWENDY-ONE," in *Proceedings - IEEE International Conference on Robotics and Automation*, pp. 580–586, 2009.

[40] T. Asfour, K. Berns, and R. Dillmann, "The Humanoid Robot ARMAR : Design and Control," *The Second International Symposium in HUmanoid RObots (HURO'99)*, pp. 174–180, 1999.

[41] T. Asfour, K. Regenstein, P. Azad, J. Schröder, A. Bierbaum, N. Vahrenkamp, and R. Dillmann, "ARMAR-III: An integrated humanoid platform for sensory-motor control," in *Proceedings of the 2006 6th IEEE-RAS International Conference on Humanoid Robots, HUMANOIDS*, pp. 169–175, 2006.

[42] "ARMAR-4: A 63 DOF torque controlled humanoid robot," *2013 13th IEEE-RAS International Conference on Humanoid Robots (Humanoids)*, pp. 390–396.

[43] F. Gravez, B. Mohamed, and F. Ouezdou, "Dynamic simulation of a humanoid robot with four DOFs torso," *Proceedings 2002 IEEE International Conference on Robotics and Automation (Cat. No.02CH37292)*, vol. 1, no. May, pp. 1–6, 2002.

[44] B. MOHAMED, *Torse biofidéle pour le robot ROBIAN: Analyse et conception basées sur l'équivalence dynamique des systémes*. PhD thesis, Université de Versailles Saint Quentin en Yvenlines, Versailles, France, 2004.

[45] Y. Ogura, H. Aikawa, K. Shimomura, H. Kondo, A. Morishima, H. Lim, and A. Takanishi, "Development of a humanoid robot WABIAN-2," in *Proceedings of the IEEE International Conference on Robotics and Automation*, pp. 76 –81, 2006.

[46] Y. Nakanishi, S. Ohta, T. Shirai, Y. Asano, T. Kozuki, Y. Kakehashi, H. Mizoguchi, T. Kurotobi, Y. Motegi, K. Sasabuchi, J. Urata, K. Okada, I. Mizuuchi, and M. Inaba, "Design approach of biologically-inspired musculoskeletal humanoids: Invited paper," *International Journal of Advanced Robotic Systems*, vol. 10, 2013.

[47] I. Mizuuchi, T. Yoshikai, Y. Sodeyama, Y. Nakanishi, A. Miyadera, T. Yamamoto, T. Niemelä, M. Hayashi, J. Urata, Y. Namiki, T. Nishino, and M. Inaba, "Development of musculoskeletal humanoid Kotaro," in *Proceedings - IEEE International Conference on Robotics and Automation*, vol. 2006, pp. 82–87, 2006.

[48] I. Mizuuchi, Y. Nakanishi, Y. Sodeyama, Y. Namiki, T. Nishino, N. Muramatsu, J. Urata, K. Hongo, T. Yoshikai, and M. Inaba, "An advanced musculoskeletal humanoid kojiro," in *Proceedings of the 2007 7th IEEE-RAS International Conference on Humanoid Robots, HUMANOIDS 2007*, pp. 294–299, 2008.

[49] Y. Nakanishi, Y. Asano, T. Kozuki, H. Mizoguchi, Y. Motegi, M. Osada, T. Shirai, J. Urata, K. Okada, and M. Inaba, "Design concept of detail musculoskeletal humanoid 'Kenshiro' - Toward a real human body musculoskeletal simulator," in *IEEE-RAS International Conference on Humanoid Robots*, pp. 1–6, 2012.

[50] M. Lapeyre, P. Rouanet, and P. Oudeyer, "Poppy Humanoid Platform: Experimental Evaluation of the Role of a Bio-inspired Thigh Shape," *Humanoids 2013*, vol. 2013, 2013.

[51] O. Ly and P. Y. Oudeyer, "Acroban the humanoid: Compliance for stabilization and human interaction," in *IEEE/RSJ 2010 International Conference on Intelligent Robots and Systems, IROS 2010 - Conference Proceedings*, pp. 2525–2526, 2010.

[52] Y. Cao, K. Lu, X. Li, and Y. Zang, "Accurate Numerical Methods for Computing 2D and 3D Robot Workspace," *International Journal of Advanced Robotic Systems*, vol. 8, no. 6, pp. 1–13, 2011.

[53] D. Kohli and J. Spanos, "Workspace analysis of mechanical manipulators using polynomial discriminants," *Journal of Mechanisms, Transmissions, and Automation in Design*, vol. 107, pp. 209–215, 06 1985.

[54] A. Kumar and K. J. Waldron, "The workspaces of a mechanical manipulator," *Journal of Mechanical Design*, vol. 103, pp. 665–672, 07 1981.

[55] N. P. Reeves and J. Cholewicki, "Modeling the human lumbar spine for assessing spinal loads, stability, and risk of injury.," *Critical reviews in biomedical engineering*, vol. 31, no. 1-2, pp. 73–139, 2003.

[56] A. B. Schultz and J. O. Galante, "A mathematical model for the study of the mechanics of the human vertebral column," *Journal of Biomechanics*, vol. 3, no. 4, pp. 405–416, 1970.

[57] L. Lindbeck, "Analysis of the asymmetrically loaded spine by means of a continuum beam model," *Journal of Biomechanics*, vol. 20, no. 8, pp. 753–765, 1987.

[58] K. P. Granata and S. E. Wilson, "Trunk posture and spinal stability," *Clinical Biomechanics*, vol. 16, no. 8, pp. 650–659, 2001.

[59] R. L. Adler, J.-P. Dedieu, J. Y. Margulies, M. Martens, and M. Shub, "Newton's method on Riemannian manifolds and a geometric model for the human spine," *IMA Journal of Numerical Analysis*, vol. 22, pp. 359–390, 2002.

[60] T. Merrill, W. Goldsmith, and Y. C. Deng, "Three-dimensional response of a lumped parameter head-neck model due to impact and impulsive loading," *Journal of Biomechanics*, vol. 17, no. 2, pp. 81–95, 1984.

[61] J. L. Williams and T. B. Belytschko, "A three-dimensional model of the human cervical spine for impact simulation.," 1983.

[62] S. Y. Ishikawa Y., " Model Simulation for Restoration of Trunk in Complete Paraplegiaby Functional Electrical Simulation," *Proceedings IFESS05 Conference Montreal, Canada.*, 2005.

[63] T. Zander, A. Rohlmann, C. Klöckner, and G. Bergmann, "Comparison of the mechanical behavior of the lumbar spine following mono- and bisegmental stabilization," *Clinical Biomechanics*, vol. 17, no. 6, pp. 439–445, 2002.

[64] R. Cooper, C. Cardan, and R. Allen, "Computer visualisation of the moving human lumbar spine," *Computers in Biology and Medicine*, vol. 31, no. 6, pp. 451–469, 2001.

[65] D. Ma and H. M. Lankarani, "A multibody/finite element analysis approach for modeling of crash dynamic responses," *Journal of Mechanical Design*, vol. 119, pp. 382–387, 09 1997.

[66] M. M. Panjabi, N. Chen, E. Shin, and J. Wang, "The cortical shell architecture of human cervical vertebral bodies.," *Spine*, vol. 26, no. 22, pp. 2478–2484, 2001.

[67] S. Del Din, E. Carraro, Z. Sawacha, A. Guiotto, L. Bonaldo, S. Masiero, and C. Cobelli, "Impaired gait in ankylosing spondylitis," *Medical and Biological Engineering and Computing*, vol. 49, no. 7, pp. 801–809, 2011.

[68] "Ankylosing spondylitis." https://www.niams.nih.gov.

[69] J. Or, "Humanoids grow a spine: The effect of lateral spinal motion on the mechanical energy efficiency," *IEEE Robotics Automation Magazine*, vol. 20, pp. 71–81, June 2013.

[70] J. Crosbie, R. Vachalathiti, and R. Smith, "Patterns of spinal motion during walking," *Gait and Posture*, vol. 5, no. 1, pp. 6–12, 1997.

[71] A. Konno, R. Sellaouti, F. Amar, and F. Ouezdou, "Design and development of the biped prototype ROBIAN," *Proceedings 2002 IEEE International Conference on Robotics and Automation (Cat. No.02CH37292)*, vol. 2, 2002.

[72] S. B. Rok, Y. Byung-Ju, K. Wheekuk, O. Sang-Rok, P. Jongil, and K. Y. Soo, "Design of a redundantly actuated leg mechanism," *2003 IEEE International Conference on Robotics and Automation (Cat. No.03CH37422)*, vol. 3, 2003.

[73] S. Alfayad, F. B. Ouezdou, F. Namoun, O. Bruneau, and P. Hénaff, "Three DOF hybrid mechanism for humanoid robotic application: Modeling, design and realization," *2009 IEEE/RSJ International Conference on Intelligent Robots and Systems, IROS 2009*, pp. 4955–4961, 2009.

[74] W. Khalil and E. Dombre, *Modeling, Identification and Control of Robots*. 2002.

[75] J. Park, "Synthesis of natural arm swing motion in human bipedal walking," *Journal of Biomechanics*, vol. 41, no. 7, pp. 1417–1426, 2008.

[76] H. O. Elftman, *The Function of the Arms in Walking*. Johns Hopkins Press, 1939.

[77] S. M. Bruijn, O. G. Meijer, P. J. Beek, and J. H. van Dieën, "The effects of arm swing on human gait stability," *Journal of Experimental Biology*, vol. 213, no. 23, pp. 3945–3952, 2010.

[78] W. Maurel and D. Thalmann, "Human shoulder modeling including scapulothoracic constraint and joint sinus cones," *Computers and Graphics (Pergamon)*, vol. 24, no. 2, pp. 203–218, 2000.

[79] S. Dayanidhi, M. Orlin, S. Kozin, S. Duff, and A. Karduna, "Scapular kinematics during humeral elevation in adults and children," *Clinical Biomechanics*, vol. 20, no. 6, pp. 600–606, 2005.

[80] N. Klopčar, M. Tomšič, and J. Lenarčič, "A kinematic model of the shoulder complex to evaluate the arm-reachable workspace," *Journal of Biomechanics*, vol. 40, no. 1, pp. 86–91, 2007.

[81] B. Tondu, "A kinematic Model of the Upper Limb with a Clavicle-like Link for Humanoid Robots," *International Journal of Humanoid Robotics*, vol. 5, no. 1, pp. 87–118, 2008.

[82] S. Ikemoto, Y. Kimoto, and K. Hosoda, "Shoulder complex linkage mechanism for humanlike musculoskeletal robot arms," *Bioinspiration & Biomimetics*, vol. 10, no. 6, p. 066009, 2015.

[83] Y. Sodeyama, T. Nishino, Y. Namiki, Y. Nakanishi, I. Mizuuchi, and M. Inaba, "The designs and motions of a shoulder structure with a spherical thorax, scapulas and collarbones for humanoid," in *2008 IEEE/RSJ International Conference on Intelligent Robots and Systems*, pp. 1465–1470, Sept 2008.

[84] H. G. Marques, M. JÃd'ntsch, S. Wittmeier, O. Holland, C. Alessandro, A. Diamond, M. Lungarella, and R. Knight, "Ecce1: The first of a series of anthropomimetic musculoskeletal upper torsos," in *2010 10th IEEE-RAS International Conference on Humanoid Robots*, pp. 391–396, Dec 2010.

[85] A. E. Engin and S. T. Tüumer, "Three-Dimensional Kinematic Modelling of the Human Shoulder Complex,Part I: Physical Model and Determination of Joint Sinus Cones," *Journal of Biomechanical Engineering*, vol. 111, pp. 107–112, may 1989.

[86] S. T. Tümer and A. E. Engin, "Three-Dimensional Kinematic Modelling of the Human Shoulder Complex,Part II: Mathematical Modelling and Solution Via Optimization," *Journal of Biomechanical Engineering*, vol. 111, pp. 113–121, may 1989.

[87] C. B. Barber and D. P. Dobkin, "The Quickhull Algorithm for Convex Hulls," vol. 22, no. 4, pp. 469–483, 1996.

Appendix A

Chapter 2

A.1 Coordinates of center of mass

The center of mass of each link is calculated as follow:

$$x_{1c} = -l_{1c}.cos(\theta_1(t)) \tag{A-1}$$

$$y_{1c} = l_{1c}.sin(\theta_1(t)) \tag{A-2}$$

$$x_{2c} = -l_1.cos(\theta_1(t)) + h.sin(\theta_1(t)) + l_{2c}.cos(\theta_2(t)) \tag{A-3}$$

$$y_{2c} = l_1.sin(\theta_1(t)) + h.cos(\theta_1(t)) + l_{2c}.sin(\theta_2(t)) \tag{A-4}$$

$$x_{3c} = -l_1.cos(\theta_1(t)) + h.sin(\theta_1(t)) + l_2.cos(\theta_2(t)) + l_{3c}.cos(\theta_3(t)) \tag{A-5}$$

$$y_{3c} = l_1.sin(\theta_1(t)) + h.cos(\theta_1(t)) + l_2.sin(\theta_2(t)) + l_{3c}.sin(\theta_3(t)) \tag{A-6}$$

$$x_{4c} = -l_1.cos(\theta_1(t)) + h.sin(\theta_1(t)) + l_2.cos(\theta_2(t)) + l_3.cos(\theta_3(t)) + l_{4c}.cos(\theta_4(t)) \tag{A-7}$$

$$y_{4c} = l_1.sin(\theta_1(t)) + h.cos(\theta_1(t)) + l_2.sin(\theta_2(t)) + l_3.sin(\theta_3(t)) + l_{4c}.sin(\theta_4(t)) \tag{A-8}$$

$$x_{5c} = -l_1.cos(\theta_1(t)) + h.sin(\theta_1(t)) + l_2.cos(\theta_2(t)) + l_3.cos(\theta_3(t)) + (l_5 - l_{5c}).cos(\theta_5(t)) \tag{A-9}$$

$$y_{5c} = l_1.sin(\theta_1(t)) + h.cos(\theta_1(t)) + l_2.sin(\theta_2(t)) + l_3.sin(\theta_3(t)) - (l_5 - l_{5c}).sin(\theta_5(t)) \tag{A-10}$$

$$x_{6c} = -l_1.cos(\theta_1(t)) + h.sin(\theta_1(t)) + l_2.cos(\theta_2(t)) + l_3.cos(\theta_3(t)) + l_5.cos(\theta_5(t)) + (l_6 - l_{6c}).cos(\theta_6(t)) \tag{A-11}$$

$$y_{6c} = l_1.sin(\theta_1(t)) + h.cos(\theta_1(t)) + l_2.sin(\theta_2(t)) + l_3.sin(\theta_3(t)) - l_5.sin(\theta_5(t)) - (l_6 - l_{6c}).sin(\theta_6(t)) \tag{A-12}$$

$$\begin{aligned} x_{7c} = & -l_1.cos(\theta_1(t)) + h.sin(\theta_1(t)) + l_2.cos(\theta_2(t)) + l_3.cos(\theta_3(t)) \\ & + l_5.cos(\theta_5(t)) + l_6.cos(\theta_6(t)) + k.sin(\theta_7(t)) + l_{7c}.cos(\theta_7(t)) \end{aligned} \tag{A-13}$$

$$\begin{aligned} y_{7c} = & l_1.sin(\theta_1(t)) + h.cos(\theta_1(t)) + l_2.sin(\theta_2(t)) + l_3.sin(\theta_3(t)) \\ & - l_5.sin(\theta_5(t)) - l_6.sin(\theta_6(t)) - k.cos(\theta_7(t)) + l_{7c}.sin(\theta_7(t)) \end{aligned} \tag{A-14}$$

A.2 Relative angle equations

$$\theta_1 = q_0 \tag{A-15}$$

$$\theta_2 = \frac{Pi}{2} - q_0 - q_1 \tag{A-16}$$

$$\theta_3 = \frac{Pi}{2} - q_0 - q_1 + q_2 \tag{A-17}$$

$$\theta_4 = \frac{Pi}{2} - q_0 - q_1 + q_2 + q_3 \tag{A-18}$$

$$\theta_5 = \frac{Pi}{2} + q_0 + q_1 - q_2 - q_3 - q_4 \tag{A-19}$$

$$\theta_6 = \frac{Pi}{2} + q_0 + q_1 - q_2 - q_3 - q_4 + q_5 \tag{A-20}$$

$$\theta_7 = -q_0 - q_1 + q_2 + q_3 + q_4 - q_5 + q_6 \tag{A-21}$$

A.3 Torques Equations

A.3.1 Seven-link model

$$\tau_{q0} = \tau_{\theta1} - \tau_{\theta2} - \tau_{\theta3} - \tau_{\theta4} + \tau_{\theta5} + \tau_{\theta6} - \tau_{\theta7} \tag{A-22}$$

$$\tau_{q1} = -\tau_{\theta2} - \tau_{\theta3} - \tau_{\theta4} + \tau_{\theta5} + \tau_{\theta6} - \tau_{\theta7} \tag{A-23}$$

$$\tau_{q2} = \tau_{\theta3} + \tau_{\theta4} - \tau_{\theta5} - \tau_{\theta6} + \tau_{\theta7} \tag{A-24}$$

$$\tau_{q3} = \tau_{\theta4} - \tau_{\theta5} - \tau_{\theta6} + \tau_{\theta7} \tag{A-25}$$

$$\tau_{q4} = -\tau_{\theta 5} - \tau_{\theta 6} + \tau_{\theta 7} \tag{A-26}$$

$$\tau_{q5} = \tau_{\theta 6} - \tau_{\theta 7} \tag{A-27}$$

$$\tau_{q6} = \tau_{\theta 7} \tag{A-28}$$

A.3.2 Eight-link model

$$\tau_{q0} = \tau_{\theta 1} - \tau_{\theta 2} - \tau_{\theta 3} - \tau_{\theta 4} + \tau_{\theta 5} + \tau_{\theta 6} - \tau_{\theta 7} - \tau_{\theta 8} \tag{A-29}$$

$$\tau_{q1} = -\tau_{\theta 2} - \tau_{\theta 3} - \tau_{\theta 4} + \tau_{\theta 5} + \tau_{\theta 6} - \tau_{\theta 7} - \tau_{\theta 8} \tag{A-30}$$

$$\tau_{q2} = \tau_{\theta 3} + \tau_{\theta 4} - \tau_{\theta 5} - \tau_{\theta 6} + \tau_{\theta 7} + \tau_{\theta 8} \tag{A-31}$$

$$\tau_{q3} = \tau_{\theta 4} - \tau_{\theta 5} - \tau_{\theta 6} + \tau_{\theta 7} + \tau_{\theta 8} \tag{A-32}$$

$$\tau_{q4} = -\tau_{\theta 5} - \tau_{\theta 6} + \tau_{\theta 7} \tag{A-33}$$

$$\tau_{q5} = \tau_{\theta 6} - \tau_{\theta 7} \tag{A-34}$$

$$\tau_{q6} = \tau_{\theta 7} \tag{A-35}$$

$$\tau_{q7} = \tau_{\theta 8} \tag{A-36}$$